UNIVERSITY OF LATVIA

FACULTY OF PHYSICS AND MATHEMATICS

LATVIJAS UNIVERSITĀTE

FIZIKAS UN MATEMĀTIKAS FAKULTĀTE

Edgars Nitišs

INVESTIGATIONS OF NONLINEAR OPTICAL ORGANIC GLASS WAVEGUIDES AND THEIR APPLICATIONS

DOCTORAL THESIS

Submitted for the Degree of Doctor of Physics

Subfield of Solid State Physics

Scientific Advisor: Dr. Phys. Martins Rutkis

NELINĀRI OPTISKU ORGANISKU STIKLU VIĻŅVADU UN TO PIELIETOJUMU PĒTĪJUMI

PROMOCIJAS DARBS

Doktora zinātniskā grāda iegūšanai fizikas nozarē

Apakšnozare: cietvielu fizika

Zinātniskais vadītājs: Dr. Phys. Mārtiņš Rutkis

Riga, 2015

This work was conducted at the Institute of Solid State Physics, University of Latvia, from October 2011 until March 2015.

Type of thesis: scientific papers

This work has been supported by the European Social Fund within the project «Support for Doctoral Studies at University of Latvia».

Promocijas darbs izstrādāts Latvijas Universitātes Cietvielu Fizikas institūtā laika posmā no 2011. gada oktobra līdz 2015. gada martam.

Darba forma: publikāciju kopa

Šis darbs izstrādāts ar Eiropas Sociālā fonda atbalstu projektā «Atbalsts doktora studijām Latvijas Universitātē».

Abstract

The development of information and telecommunication technology rests upon an ever-increasing speed of information processing and transfer. Nonlinear organic materials have been shown to be appealing candidates for the mentioned technologies for the development of optoelectronic and photonic devices. Currently a considerable effort is devoted towards research and characterization of new organic materials for electro-optical applications as well as to develop new types of active waveguide device designs.

In this contribution the author of this thesis presents the results obtained during the implementation of methods for characterization of linear and non-linear optical properties of waveguides, the waveguide poling investigations and the development of a waveguide modulator design.

Keywords: nonlinear optics, organic materials, material characterization, waveguides

Anotācija

Informācijas un telekomunikāciju tehnoloģijas nozaru turpmākajai attīstībai nepieciešamas jaunas ierīces ātrākai informācijas apstrādāšanai un pārnešanai. Nozares izaugsmi būtiski veicinātu datu pārraidē izmantoto elektrooptisko modulatoru darbības ātruma palielināšana. To paredzēts sasniegt izmantojot integrētas viļņvadu ierīces, kurās par elektrooptisko aktīvo vidi izmantos nelineāri optiski (NLO) aktīvus organiskus materiālus. Organiskiem NLO materiāliem piemīt vairākas būtiskas īpašības, kuru dēļ tie varētu tikt plaši izmantoti dažādās viļņvadu ierīces.

Šajā promocijas darbā autors apkopo iegūtos rezultātus, kas iegūti veicot elektrooptisko organisku stiklu viļņvadu lineāri un nelineāri optisko īpašību pētījumus, elektrooptisko viļņvadu materiālu orientēšanas pētījumus, kā arī izstrādājot jauna tipa elektrooptisko viļņvada modulatora izgatavošanas koncepciju. Autors pirmo reizi demonstrē, ka Abelsa matricu formālismu var izmantot, lai aprakstītu eksperimentālos rezultātus, kas iegūti ar Tenga-Mana metodi un Maha-Zendera interferometrisko metodi, un noteikt plānu kārtiņu elektrooptiskos koeficientus.

Atslēgvārdi: nelineārā optika, organiskie materiāli, materiālu īpašību pētījumi, viļņvadi.

List of the scientific papers included in the Thesis

Promocijas darbā iekļauto publikāciju saraksts

1. **E. Nitiss**, M.Rutkis, O.Vilitis, Determination of electro-optic coefficient of thin organic films by Mach-Zehnder interferometric method, Latvian Journal of Physics and Technical Sciences 3 (46), 5-14 (2009)
2. **E. Nitiss**, M. Rutkis, M. Svilans, Effects of the multiple internal reflection and sample thickness changes on determination if electro-optica coefficient values of a polymer film, *Lithuanian Journal of Physics* 52 (1), 30-38 (2012)
3. **E. Nitiss**, R. Usans, M. Rutkis, Simple method for measuring bilayer system optical parameters, SPIE Proceedings, 8430, 84301C, (2012)
4. **E. Nitiss**, M. Rutkis, M. Svilans, Electrooptic coefficient measurements by Mach Zender interferometric method: application of Abeles matrix formalism for thin film polymeric sample description, Optics Communications 286, 357-362, (2013)
5. **E. Nitiss**, E. Titavs, K. Kundzins, A. Dementjev, V. Gulbinas, M. Rutkis, Poling Induced Mass Transport in Thin Polymer Films, J. Phys. Chem. B 117, 2812−2819 (2013)
6. **E. Nitiss**, J. Busenbergs, M. Rutkis, Optical propagation loss measurements in electro optical host - guest waveguides, SPIE Proceedings, 8772, 87721L (2013)
7. **E. Nitiss**, J. Busenbergs, M. Rutkis, Hybrid silicon on insulator/polymer electro-optical intensity modulator operating at 780 nm, J. Opt. Soc. Am. B 31 (10), 2446-2454, (2014)
8. **E. Nitiss**, A. Bundulis, A. Tokmakov, J. Busenbergs, E. Linina, M. Rutkis, Review and comparison of experimental techniques used for determination of thin film electro-optic coefficients, Phys. Status Solidi A, 1–13 (2015) / DOI 10.1002/pssa.201532054

DETERMINATION OF ELECTRO-OPTIC COEFFICIENT OF THIN ORGANIC FILMS BY MACH-ZEHNDER'S INTERFEROMETRIC METHOD

E. Nitišs*, M. Rutkis, O. Vilītis

Institute of Solid State Physics of University of Latvia
8 Kengaraga Str., Riga-1063, LATVIA
*email: edgars.nitiss@cfi.lu.lv

The authors analyze the use of Mach-Zehnder's interferometric (MZI) method for determining the electro-optic coefficient of thin organic films. The theoretical analysis of numerous methods existing for this purpose is shortly reported, and reasoned argumentation in favor of the MZI method is given. For successful implementation of this method the effects caused by its drawbacks – such as sensitivity to vibrations, instability of the measurement point (interferometer phase), electro-magnetically induced false signal in the lock-in amplifier – should be minimized. The experience gained during implementation of the method is described, and the results of measuring the r_{13} values for host-guest PMMA films containing tBu-DMABI as chromophore are provided.

1. INTRODUCTION

Due to the rapid growth of defense, computing and telecommunications industries a significant need for faster electro-optical (EO) modulators has thrived [1]. Increase in the operational speed of EO modulators could be achieved by substitution of electrical-field poled NLO active polymers for widely used inorganic NLO active crystals (such as $LiNbO_3$). The EO coefficients of a thin film are usually the most important criteria for the evaluation and further optimization of new EO polymer materials. Due to the symmetry reasons, in poled polymer films only two EO coefficients – r_{13} and r_{33} – should be determined. A wide range of methods for determination of EO coefficients are described in the literature.

In terms of the optical setup, the one-beam, two-beam and multi-beam interferometric techniques have been used for this purpose.

One-beam ellipsometric methods are based on determination of the phase shift of *s*- and *p*-polarized light caused by EO effect. The reflection or Teng – Mann's technique [2] is more often used in comparison with the transmission technique [3], because only one of the electrodes should be light-semitransparent. However, both techniques allow determining only the effective EO coefficient, which is a combination of r_{13} and r_{33}. As a rule, assumption $r_{33} = 3r_{13}$ is used – an applicable approximation in the case of weak poling fields where $\mu E < kT$ [4]. Nonetheless, recent investigations point out that the optical wave-guiding technique described in [5] shows more reliable results than ones mentioned before (see [6]).

Two-beam interferometric setups are based on the traditional Mach-Zehnder interferometer (MZI) or Michelson interferometer, where light wave phase shift in a sample arm due to EO effect is measured. The MZI technique [7] is more often used because of simpler adjustment of the interference pattern. The resulting phase difference can easily be changed via changing the optical path length in the reference arm. Both techniques are very sensitive to mechanical and acoustical vibrations, which results in the instability of measurement point.

In multiple beam methods, the sample serves as a Fabri – Perot etalon filled with the EO material under investigation. Change of the material refractive index due to EO effect causes alternation of light transmission through the interferometer (more detailed description of this technique can be found in [8, 9]).

The electrical scheme of the setup depends on the type of electrical field applied to the sample. For optically stable setups (usually in one-beam methods) the static field (DC) method is commonly used. The dynamic field (AC) method in combination with lock-in amplifier detection allows the determination of very low light modulation amplitudes, and therefore is used when the expected EO modulated signal is small [10].

Before initiating the creation of an appropriate device one has to think about both optical and electrical schemes, and to estimate advantages and disadvantages of their experimental performance [11].

The advantage of MZI method is the possibility to obtain a dependence of the effective EO coefficient on the probing light polarization and incidence angle; therefore, the main reasons for selecting MZI method were the following: determination of both r_{13} and r_{33} should be possible; the resulting phase difference and thus the location of measurement point should be changeable; simplicity of the optical setup. The dynamic field (AC) method was chosen because it is the most sensitive available method for detection of small signals, and would be very useful in our case, when the signal-to-noise ratio is expected to be low.

However, the mentioned method also possesses several drawbacks – high sensitivity to vibrations, instability of measurement point (phase difference), electro-induced false signal in the lock-in amplifier, etc. For successful implementation of Mach-Zehnder's inteferometric method the effect of these drawbacks should be reduced. We will report our experience gained at implementation of the method and provide measurement results of r_{13} for host-guest films containing DMABI derivatives as chromophores.

2. EXPERIMENTAL

The assembled experimental setup is presented on Fig. 1. The CW He-Ne laser beam (λ=633 nm) is split into sample and reference arms and then again recombined creating a two-beam interference, which can be described by the following relation:

$$I = \frac{1}{2}\left(I_1 + I_2 + 2\sqrt{I_1 I_2}\cos(\varphi_0 + \varphi(V))\right), \quad (1)$$

where I is the resulting light intensity, I_1 and I_2 are the interfering beam intensities, and φ_0 is the phase difference of interfering beams which defines the measurement point. Last term $\varphi(V)$ is the phase difference originated by the change of refractive index of EO material caused by applied AC modulation voltage. The resulting output intensity of MZI is dependent on both φ_0 and $\varphi(V)$. Small light intensity AC modulations are detected by a lock-in amplifier and registered by computer. The reference beam travels through the phase compensator – in our case a small-angle glass wedge, whose position and, therefore, the interferometer's phase difference (measurement point) is controlled by the computer. The resulting light intensity is registered by computer with a photodiode. We used a lens and a slit for magnification of the interference pattern and the selection of a spatial interference region where the modulation detection takes place. The incident light polarization can be changed by rotation of a half-wave plate.

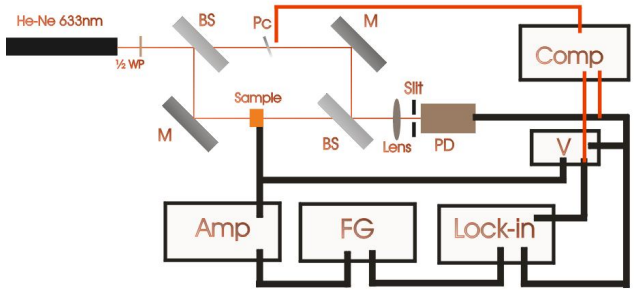

Fig.1. Schematic of experiment: He-Ne, helium-neon laser λ=633 nm; ½ WP, half-wave plate; BS: 50/50 beam splitter; Pc: phase compensator (wedge); M: mirror; Sample; Lens; PD: photodiode; Slit; V: voltmeter; Comp: computer; FG: function generator; Amp: signal amplifier; Lock-in: lock-in amplifier.

It is very important to select an appropriate measurement point, i.e. the phase difference of MZ interferometer at which the light modulation by EO effect will occur. In Fig.2*a* the resulting intensity curve is shown as a function of phase difference.

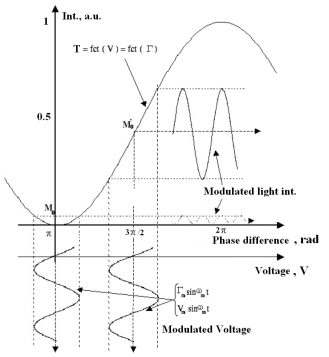

a.

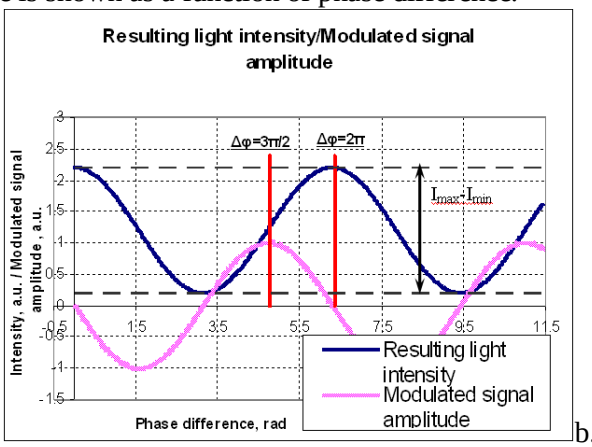

b.

Fig. 2. a) Resulting light intensity as a function of phase difference in MZI arms; *I=f(φ)*; maximum linearity point M_0' and minimum transmission point M_0.

b) Resulting light intensity and modulation signal amplitude as a function of phase difference of interfering waves.

Usually, the modulation is carried out at the phase difference of $\pi/2$, or the maximum linearity point M_0', because the amplitude of the EO modulated signal is maximal. This point can be used if the modulated signal amplitude is small. Another option is to carry out the measurements at the minimum transmission point M_0. However, at M_0 the lock-in amplifier should be set up to recover the second harmonic signal of modulation voltage frequency; besides, the signal amplitude is very sensitive to phase changes [2].
The effective EO coefficients at the maximum linearity point M_0' can be calculated by the relation:

$$r_{eff}^{s,p} = \frac{2\lambda}{\pi U n^3} \cdot \frac{I_{\mathrm{mod}}}{[I_{\max} - I_{\min}]} \cdot \cos\alpha \,, \tag{2}$$

where λ is the optical wavelength, I_{mod} is the modulated signal (amplitude), $I_{\max}$ is the light intensity in the case of constructive interference, $I_{\min}$ is the light intensity in the case of destructive interference, U is the AC modulation voltage (amplitude), α is the light propagation angle in EO material, r_{eff}^{s} r_{eff}^{p} is the effective EO coefficient for *s*- and *p*-polarized incident light, respectively. These effective values are related to r_{13} and r_{33} according to the following equations:

$$r_{eff}^{s} = r_{13} \tag{3}$$

$$r_{eff}^{p} = r_{13}\cos^2\alpha + r_{33}\sin^2\alpha \tag{4}$$

An important aspect of successful determination of r_{eff} is the preparation of samples. In our setup tests we have used organic host-guest films containing NLO active tret-butil 2-(4'-N,N-dimethylaminobenzylidene)indan 1,3-dione (tBu-DMABI) as chromophores and PMMA (poly methyl methacrylate (T_g=120^{o}C)) as polymer matrix. This host-guest system was chosen because it possesses nonlinear optical coefficients [12]. Thin PMMA films containing 5 wt% tBu –DMABI were deposited on conventional glass slides with ITO coating – either by spin-coating or blade casting technique.

A serious disadvantage of MZI method is the necessity to put a film between two light transparent and, at same time, conducting electrodes. In our case, a semitransparent ITO layer could serve as a bottom electrode. One of the possibilities to create the top electrode is to sputter a transparent gold layer directly onto the host-guest film. Unfortunately, because of high temperature during the sputtering, we did not succeed in producing a good conducting electrode without "destroying" the sample. Finally, it was decided to make samples with the structure as shown in Fig. 3.

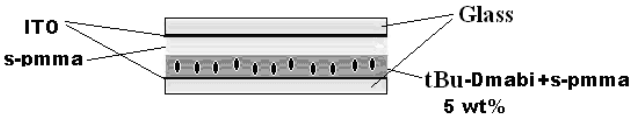

Fig. 3. The "sandwich type" sample for measuring r_{eff} of tBu-DMABI/PMMA host -guest system.

The essential in our concept was to prepare independently "top" and "bottom" parts of the sample and afterwards "bake" them together in the structure shown in Fig.3. As can be seen in this figure, one of the PMMA films in our "sandwich" contains no chromophore. This layer serves as an additional insulator preventing electrical brake-down of the sample during the poling. The chromophores in the matrix tend to make small crystals [13], which act as conducting channels; therefore, an insulating layer of pure PMMA is very useful.

The thickness and surface profile of the films are different for samples prepared by spin-coating or by blade-casting methods. A sample surface scan made by a "Dektak" profilometer can be seen in Fig. 4. The average thickness of the films produced by the spin-coating method was approximately 1-1.2 μm, whereas for the blade-casting method it was up to 5 μm. The surface of spin-coated films is quite smooth and thicker at the slide sides. In contrast, the blade-cast films are much rougher and thicker at the middle of slide. These properties of the films, as we will see further, are very important for preparation of good samples.

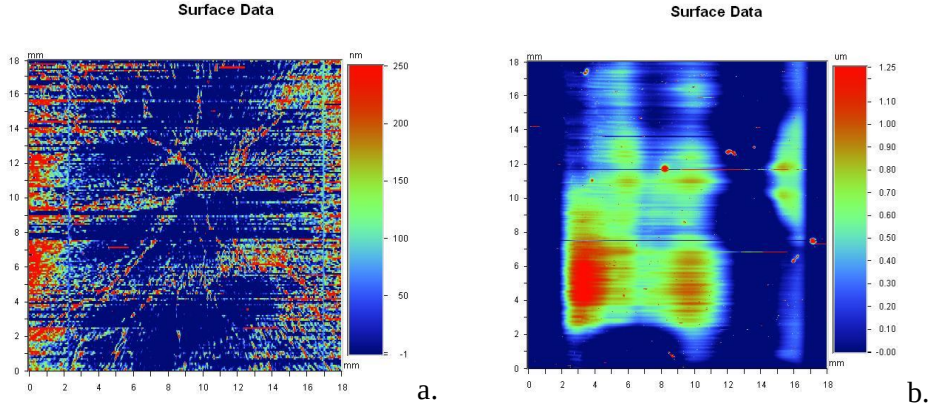

Fig. 4. Sample surface scan made by "Dektak" profilometer: a) spin-coated sample; b) blade-cast sample

.

Finally, separately made "parts" are pressed together and held under a pressure of 8 kPa at 170°C for 2 h. The electrode contact wires are attached to the ITO surfaces with silver paste. Afterwards, the sample is placed into a sample holder where the heating and chromophore orientation process (poling) takes place.

The EO modulation frequency was selected to be ω = 3 kHz. Our choice is based on the observation that at this frequency for all available built-in filter combinations of our lock-in amplifier the recovered signal has the highest signal-to-noise ratio.

The calculation of r_{ef} is based on the determination of EO modulation amplitude at the maximum linearity region on the $I = f(\varphi)$ curve of MZ interferometer. Unfortunately, accurate adjustment of MZI phase difference to π/2 is quite complicated. Therefore, more convenient is to scan the interferometer's phase difference by moving the glass wedge. The simultaneously acquired EO signal amplitude should have the extremes at maximum linearity points or at MZ interferometer phase differences of π(2n+1)/2. In fact, the EO signal should be in the counter-phase for odd and even ***n*** cases (see Fig. 2*a*), so the lock-in amplifier should detect positive (at n = 1, 3, …) or negative (at n = 2, 4, …) EO amplitudes. In other words, during that kind of scan we could recover two sine waves with the same frequency but shifted in phase by π/2 (see Fig 2*b*): one being the resulting light intensity at MZI output (DC photocurrent), while the other – the EO modulated signal amplitude (3kHz AC component). The necessary components of Eq.(2) are determined after the approximation: I_{mod} is the sine amplitude of modulated signal, $I_{\max} - I_{\min}$ is the double sine amplitude of the resulting intensity signal.

3. RESULTS AND DISCUSSION

Once we had set up a Mach-Zehnder interferometer for the first time we recognized that the MZI method is an amazingly sensitive tool to acoustical and mechanical vibrations. To establish MZI for reliable EO coefficient measurements, one has to handle mechanical stability problems – oscillations and drift of the phase point. We would like to pinpoint the following actions that allowed us to achieve a sufficient stability. First of all, the interferometer should be well insulated from mechanical vibrations of surrounding. A wall-mounted stand for the interferometer with appropriate shock absorbing material under its base was our solution. Reducing the MZI arm length allowed us to lower the amplitude of phase oscillations caused by vibrations of the base. Further significant improvement was achieved by replacement of ordinary mirror holders with special ultra-light and stable mirror holders - KS1 Ultra-Stable Kinematic Ø1" Mirror Mount from Thor Labs**.** At last, our MZI seems to be well damped to mechanical vibrations and stable to the resulting phase difference. By hard taping on the MZI base one could deliberately initiate mechanical vibrations. In our case, they have the characteristic relaxation time less than one second, and after damping the vibrations the initial phase difference is always recovered.

One more problem was the radio frequency (rf) signal pickup by the detection system. This effect is caused by the "transmission" of electromagnetic waves by the amplifier to the sample cable and "receiving" by the photodiode – lock-in amplifier assembly. Attenuation of this signal could be achieved by blocking the laser light at MZI input. Appropriate grounding of the electronic parts and double shielded cables make it possible to reduce the amplitude of rf-induced signal to an acceptably low level.

At first glance, the task of obtaining a sample where the EO polymer under investigation is sandwiched between semitransparent electrodes looks quite simple. In

a real situation, our thin films have thickness variations (see above). To "bake" them together with no air-gap is rather tricky [14]. **Spin-coated** samples unfortunately have the property to be thicker at the sides of a slide. As a result, a wide air-gap (usually ~ 10 μm thick) is formed at the centre of sample. A typical case could be seen in Fig. 5. This gap causes two undesirable effects: first is reduction in the poling (DC) and modulation (AC) electrical field intensities, while another is the possibility of glass slides to contract and repulse under the applied AC field due to the lack of rigid material in-between them. At the same time, glass slides are forming a sort of Fabri-Perot's (FP) etalon for which the optical path length is manipulated by mechanical vibrations, and therefore the modulated signal should correlate with the light intensity at MZI output. This modulation effect can be recognized by huge amplitudes of signal (up to 25 mV) and the lacking of phase difference between the signals.

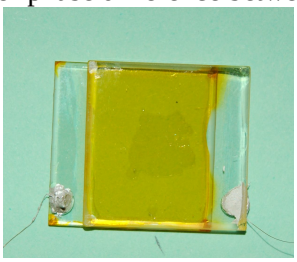

Fig. 5. Air gap of "sandwich type" sample prepared with the spin-coating method.

In the case of "baking" together **Blade-cast** samples, the air-gap formation is less probable due to the fact that these films are thicker in the middle of slides. The central area of these samples is usually filled by polymers, and the vibrations caused by electrostatic forces are less evident. The distance between ITO electrodes could be determined by spectral reflectoscopy. Typical values for our samples were within a 9 - 12 μm range. Based on these inter-electrode distances we could estimate the poling and EO modulation electric field intensity. These samples show better performance, and, in our opinion, good experimental data are demonstrated in Fig. 6. One can see the quality of interference fringe amplitude and the stability of phase difference.

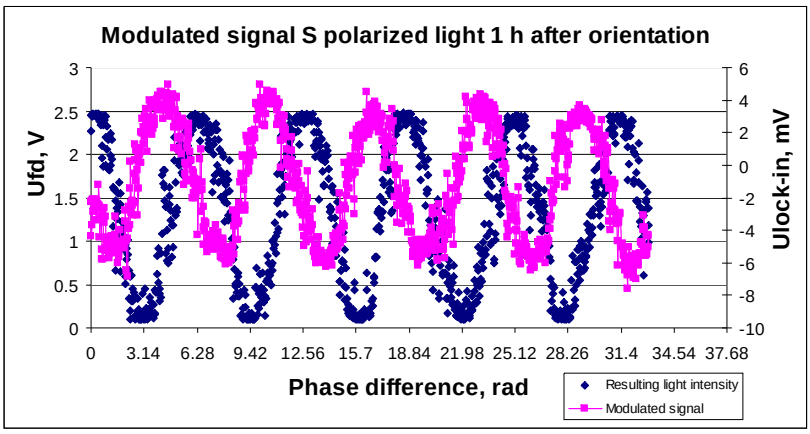

Fig. 6. EO modulated signal in the MZI; incidence angle: 0^o; 1 h after poling; modulation voltage: 49.22 V rms.

The EO modulated signal and MZI output intensity had the phase difference as expected. Both signals were afterwards approximated with sine functions. The modulated signal approximation function contains a sine part, and the DC offset attributed to small rf pickup signal is still present in the system. The amplitude of sine part in this approximation is the maximum value of EO modulated signal, or, in other words, the signal I_{mod} modulated at the maximum linearity point. The MZI characteristic value $I_{max} - I_{min}$ is the double amplitude of sine part in the approximation of the resulting light intensity. Based on these values, applying Eqs. (2) and (3), r_{13} was calculated. A typical signal-to-noise ratio is approximately 7. In Fig.7, one can see the decay of experimentally determined r_{13} values for 5 wt% tBu-DMABI in PMMA poled at T= 100C° with E_p=50V/μm.

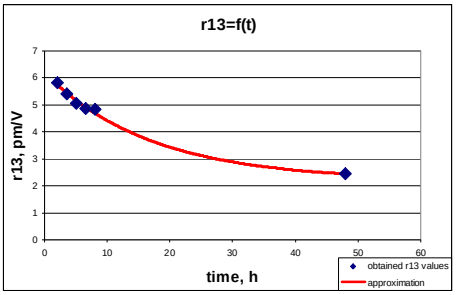

Fig. 7. Exponential r_{13} decrease with time (time constant $\tau \approx 17$ h).

The characteristic time constant ($\tau \approx 17$ h) of EO coefficient decay is in agreement with our previous observations related to the NLO coefficient decays in this system determined by the second harmonic generation (SHG).

4. CONCLUSIONS

The Mach-Zehnder interferometric method has successfully been implemented after we had found solutions to the key setup problems (to reduce extremely high sensitivity to acoustical and mechanical vibrations, attenuate rf and mechano-optical signals, etc.). Further increase in the reliability of effective determination of EO coefficients was achieved by setting-up measurements in the MZI phase scanning mode. First investigations of the test organic NLO active host-guest polymers have shown that the necessary conditions for good sandwich sample preparation by "baking" two slides are the high surface quality and compatibility of films. Finally, we can report the value r_{13} = 6.4 pm/V immediately after poling of 5 wt% tBu-DMABI in PMMA. This value decays with characteristic time $\tau \approx 17$ h to a constant value r_{13} = 2.4 pm/V after 48 h.

REFERENCES

1. Dalton L. R. (2003). Rational design of organic electro-optic materials. *J. Phys.: Condens. Matter, 15*, 897–934.
2. Teng C.C., Man H.T. (1990). Simple reflection technique for measuring the electro-optic coefficient of poled polymer films. *Appl. Phys. Lett., 56* (18).
3. Horsthuis W.H.G., Krijnen G.J.M. (1989). Simple measuring method for electro-optical coefficients in poled polymer waveguides. *Appl. Phys. Lett., 55* (7).
4. Maertens C., Detrembleur C. (1998). Synthesis and electrooptic properties of a new chromophore dispersed or grafted in a carbazolyl methacrylate matrix. *Chem. Mater., 10*, 1010-1016.
5. Burland D.M., Miller R.D., Walsh C.A. (1994). Second-order nonlinearity in poled-polymer systems. *Chem. Rev., 94*, 31 – 75.
6. Dalton L.R. *et al*. (2009). *Opt. Mater*., doi:10.1016/j.optmat.2009.02.002
7. Sigelle M., Hierle R. (1981). Determination of electrooptic coefficients for 3-methyl 4-nitropyridine 1-oxide by an interferometric phase-modulation technique. *J. Appl. Phys., 52* (6), 4199-4204.
8. Nils Benter, Ralph Peter Bertram. (2005). Large-area Fabry–Perot modulator based on electro-optic polymers. *Appl. Optics, 44* (29).
9. Patrice Nagtegaele, Etienne Brasselet, & Joseph Zyss. (2003), Anisotropy and dispersion of a Pockels tensor: a benchmark for electro-optic organic thin-film assessment. *J. Opt. Soc. Am., B, 20* (9).
10. Aillerie M., Theofanous N. (2000). Measurement of the electro-optic coefficients: description and comparison of the experimental techniques, *Appl. Phys. B, 70*, 317–334.
11. Shin, M. J., & Cho, H. R. (1997). Optical interferometric measurement of the electro-optic coefficient in nonlinear optical polymer films. *Journal of the Korean Physical Society, 31* (1), July, 99-103.
12. Rutkis M., Vembris A., Zauls V., Tokmakovs A., Fonavs E., Jurgis A., Kampars V. (2006). Novel second-order nonlinear optical polymer materials containing indandione derivatives as cromophores. *SPIE Proceedings, Organic optoelectronics and photonics.* (Eds. P.L.Heremans, M.Muccini, A.Meulenkamp)
13. Vembris A., Rutkis M., Laizane E. (2008). Effect of corona poling and thermo-cycling sequence on NLO properties of the guest-host system, *Molecular Crystals and Liquid Crystals, 485*, 873–880.
14. Brian Keith Canfield (2002). *Ph.D. Thesis*, Washington State University.

MAHA-ZENDERA INTERFEROMETRISKĀS TEHNIKAS IEVIEŠANA PLĀNU ORGANISKO KĀRTIŅU ELEKTRO-OPTISKAJIEM MĒRĪJUMIEM.

E. Nitišs, M. Rutkis, O. Vilītis

Šajā darbā tiek apskatīta Maha-Zendera interferometriskās (MZI) metodes ieviešana plānu organisku kārtiņu elektro-optisko (EO) koeficientu noteikšanai. Lai veiksmīgi ieviestu šo metodi, īpaša uzmanība jāpievērš interferometra jutības samazināšanai pret ārējām mehāniskajām un akustiskajām vibrācijām, kā arī jānovērš elektromagnētiski inducētā un mehano-optiskā viltus signālu rašanās mērījumu sistēmā. Mērījuma ticamību var palielināt detektējot EO modulētā signāla amplitūdu atkarībā no MZI fāzu starpības jeb veicot „skenējoša" tipa mērījumu. Pārbaudot eksperimentālo iekārtu un izvēlēto mērījuma metodiku, konstatējām, ka nozīmīgs faktors kvalitatīvu paraugu pagatavošanā ir atsevišķi sagatavoto NLO aktīvo organisko kārtiņu virsmas reljefs un to savietojamība „sakausēšanas" procesā. Veiksmīgi pagatavotam 5 wt% tBu-DMABI+PMMA paraugam uzreiz pēc tā orientēšanas tika noteikta EO koeficienta vērtība 6.4 pm/V. Šis lielums samazinājās ar laika konstanti $\tau \approx 17$ stundas līdz sasniedza kvazistacionāru vērtību 2.4 pm/V pēc 48 stundām.

Lithuanian Journal of Physics, Vol. **52,** No. 1, pp. 30–38 (2012)

EFFECTS OF THE MULTIPLE INTERNAL REFLECTION AND SAMPLE THICKNESS CHANGES ON DETERMINATION OF ELECTRO-OPTIC COEFFICIENT VALUES OF A POLYMER FILM

E. Nitiss [a], M. Rutkis [a], and M. Svilans [b]

[a] *Institute of Solid State Physics, University of Latvia, Kengaraga 8, LV-1063 Riga, Latvia*

[b] *Faculty of Material Science and Applied Chemistry, Riga Technical University, Āzenes 14/24, LV-1048 Riga, Latvia*

E-mail: edgars.nitiss@cfi.lu.lv

Received 8 September 2011; revised 18 January 2012; accepted 1 March 2012

New nonlinear optical (NLO) active organic materials are appealing candidates for optoelectronic and photonic technologies. For the evaluation of new NLO polymer materials for applicability in the mentioned technologies, the most important criteria are their electro-optic (EO) coefficients. We have implemented the Mach–Zehnder interferometric (MZI) method for the determination of EO coefficients of thin organic films. Despite the fact that other multiple optical methods for the determination of thin film EO coefficients are known, the MZI method has been chosen because this particular technique has high sensitivity to phase and intensity modulations in the sample arm of an interferometer and allows one to determine independently both thin film EO coefficients, r_{13} and r_{33}. In addition to the drawbacks described earlier we demonstrate that some other effects like electrostriction and multiple internal reflections in the sample have a considerable influence on light intensity at the MZI output. Taking into account these effects we have performed numerical simulations of the EO effect caused MZI output changes or modulation depth at different incidence angles using the Abeles matrix formalism. We can show that the modulated signal at the MZI output is highly dependent on the sample structure and is mainly governed by the effects mentioned above. For analysis of modulated signal components and determination of EO coefficients of a thin polymer film, a series of experiments was carried out on PMMA + DMABI 10 wt% samples.

Keywords: electro-optic coefficient, Mach–Zehnder interferometric method, nonlinear optical polymer, multiple internal reflections in polymer films

PACS codes: 81.70.Fy, 82.35.Ej

1. Introduction

Increasing interest has been devoted to new nonlinear optical (NLO) active organic materials due to their low cost, easy processability and potential applications as organic optical components in electro-optic (EO) devices.

Such organic EO materials are possible substitutes for traditional inorganic materials [1]. A high NLO activity is the most important material prerequisite for further successful application in EO devices making the evaluation of this property an important task for new material development.

Typically an organic EO material sample under investigation is a spin-coated thin film on an indium tin oxide (ITO) glass substrate and poled by an external electrical field. The EO performance of oriented film can be described by only two EO coefficients, r_{13} and r_{33} [2]. Several optical methods have been applied to characterise the EO performance of such organic materials [3–5]; however, some of the techniques are limited when it comes to determining r_{13} and r_{33} independently. In such cases, as r_{ef} is a function of r_{13} and r_{33}, the r_{33}/r_{13} ratio also needs to be known. Usually, if the film is poled at low poling fields ($\mu E < kT$), this ratio is assumed to be constant and equal to 3 [6]. In

spite of high sensitivity to acoustic and mechanical vibrations, the Mach–Zehnder interferometric (MZI) techniques in the transmission or in the reflection mode are being applied more and more often [7, 8]. Researchers using the MZI technique in the transmission mode have mostly excluded multiple internal reflections and thickness change of the sample by electrostriction and piezoelectric effects from their considerations. To our knowledge, a limited number of investigators pay attention to these effects [9–11]; however, according to our observations, the effects can contribute greatly to the measured modulated signal amplitude and phase and therefore must be taken into account. For correct determination of both EO coefficients the light intensity and phase transmitted by the multilayer EO sample must be known. It can be described by the Abelès matrix formalism [12, 13]. In this contribution we would like to present the influence of the multiple internal reflection and sample thickness change effects on the determination of polymer film EO coefficients using the MZI technique.

2. Experimental set-up

The MZI set-up for EO measurements can be seen in Fig. 1. The sample was usually examined in the transmission configuration. In contrast to the reflection configuration, where the sample is used as a mirror in the sample arm, here we can obtain modulation amplitude values as a function of the light incidence angle.

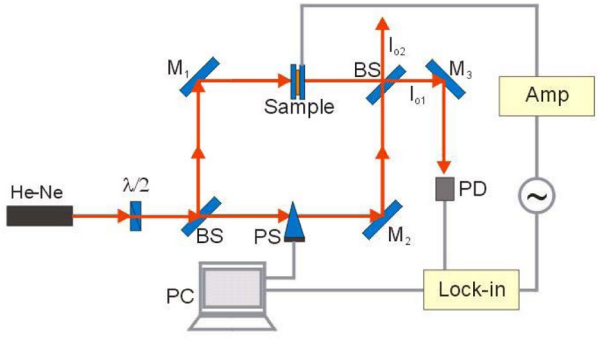

Fig.1. Experimental set-up of MZI for determination of EO coefficients of a thin organic film: helium-neon laser 632.8 nm *He–Ne*, half wave plate *λ/2*, beam splitter *BS*, mirrors M_1, M_2 and M_3, phase shifter *PS*, sample, photodiode *PD*, lock-in amplifier *Lock-in*, amplifier *Amp*, computer *PC*.

In our optical scheme we used a Helium-Neon laser (632.8 nm) as a light source. Polarisation of incident light can be controlled by a half wave plate *λ*/2. Afterwards, light is split into sample I_s and reference I_r arms of a MZI by a 50/50 beam splitter. By means of a small angle glass wedge and a computer controllable translation stage in the reference arm the interference phase of I_r and I_s and thus the AC signal measurement point can be shifted. To obtain an interference pattern the light of the reference and sample arms is combined by a second 50/50 beam splitter. The acquired interference pattern is detected by a large area Si photodiode. It is important to note that full overlapping of both light beams is necessary to achieve the maximum modulated signal. As the MZI is highly sensitive to any vibrations the elements of the optical set-up must be fixed firmly. An ultra stable beam splitter and mirror holders are suggested. A modulation voltage at 4 kHz was provided by a computer controlled lock-in detector (*Stanford Research Systems* SR830) and an amplifier (*Trek* PZD350). The light intensity modulation (AC signal) as well as the average MZI output light intensity (DC signal) was measured with the SR830 and recorded by the PC. It is important to note that the AC signal recovered by the Lock-in amplifier contains a notable fraction of crosstalk. This effect is caused by electromagnetic induction and can be recognised by its presence in the detection system with the laser light turned off. The crosstalk signal has the same frequency as the modulation caused by EO effect and creates an additional offset value in the signal detected by lock-in which is not dependent on MZI phase.

Typically, the polymer sample PMMA + DMABI 10 wt% (for a detailed molecular structure see Ref. [14]) used in this investigation was made by spin-coating (900 rpm speed, 300 rpm/s acceleration) it onto an ITO covered glass slide (*SPI Supplies* ITO 70–100 Ω) from a chloroform solution (concentration of 100 mg/ml) of appropriate amounts of components. The glass transition temperature of the polymer is approximately 110 °C.

There are two main possibilities how to obtain the sandwich sample structure. For sample 1, an ITO glass slide carrying the polymer is covered with another bare ITO glass slide as shown in Fig. 2,

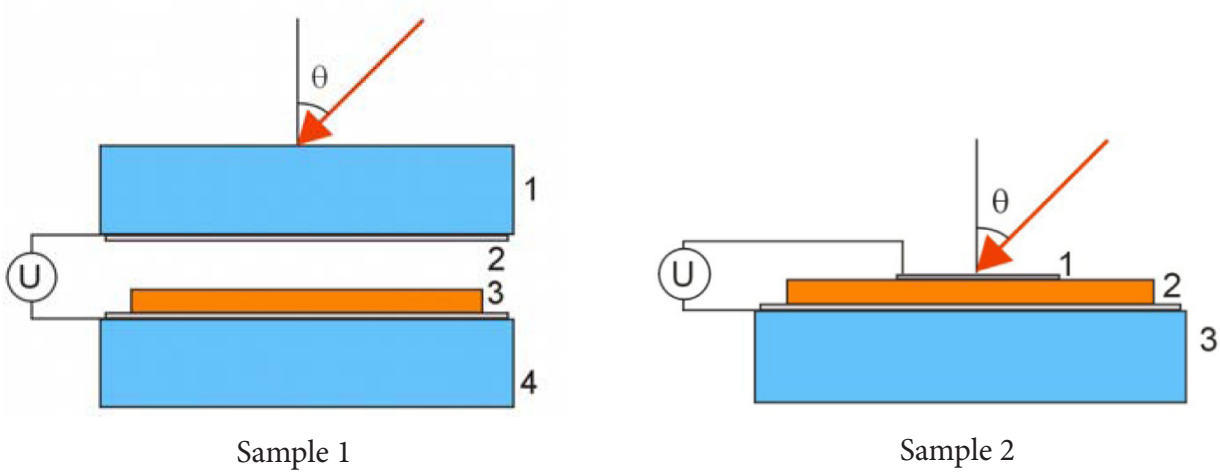

Fig. 2. Sample 1 geometry: *1*, *4* ITO coated glass, *2* air gap, *3* PMMA + DMABI 10 wt%, θ light incidence angle. Sample 2 geometry: *1* sputtered Al layer, *2* polymer (PMMA + DMABI 10 wt%), *3* ITO coated glass, θ light incidence angle.

after which both slides are squeezed together in the sample holder. On a micron scale the surface of the sample, especially at slide edges, is rather rough. Due to this an air gap forms between the surface of polymer and second ITO electrode. Alternatively, for sample 2 an Al layer with the thickness of ~25 nm can be sputtered directly onto the polymer as shown in Fig. 2. In this case the overall optical transmission coefficient of the sample is reduced; however, lower voltages on electrodes are necessary for material poling and observation of EO modulations.

The electrical connections to ITO electrodes were made using a silver paste. The *in situ* poling was performed at 100 °C and 80 V on the electrodes for 30 minutes for sample 1 and at 100 °C and 40 V on the electrodes for 30 minutes for sample 2. The EO measurements were performed after at least 24 hours during which the charge relaxation had taken place. The parameters of the sandwich type samples are as shown in Table 1.

The thickness and refractive index of the polymer thin film was determined by a prism coupler (Metricon 2010), the extinction coefficient by measuring the absorption coefficient (*Ocean Optics* HR4000CG-UV-NIR). The air gap thickness was evaluated by interference fringe separation in the low absorbance part of the sample transmittance spectrum.

Table 1. Parameters of sandwich type samples.

Sample 1			
Layer	**Thickness**	**Refractive index *n* (at 632.8 nm)**	**Extinction coefficient *k* (at 632.8 nm)**
Glass	1 ± 0.02 mm	1.50	0
ITO	15–30 nm	1.76	0
Air Gap	5.95 ± 2.38 μm	1.00	0
Polymer	0.90 ± 0.09 μm	1.54	$(10.4 \pm 0.01)\times10^{-3}$
ITO	15–30 nm	1.76	0
Glass	1±0.02 mm	1.50	0
Sample 2			
Layer	**Thickness**	**Refractive index *n* (at 632.8 nm)**	**Extinction coefficient *k* (at 632.8 nm)**
Al layer	25 ± 1 nm	1.45	7.54
Polymer	1.21 ± 0.09 μm	1.54	$(10.4 \pm 0.01)\times10^{-3}$
ITO	15–30 nm	1.76	0
Glass	1 ± 0.02 mm	1.50	0

The EO experiment was performed as follows. Modulation voltage (typically 50 V rms for sample 1 and 15 V rms for sample 2) was applied to the electrodes, the output light intensity of MZI (DC signal) and the light modulation amplitude (AC signal) was detected with the Si photodiode and measured by the lock-in detector. Data was collected for 20 s at several MZI interference phase points and then averaged. The measurement series was done with *s* and *p* polarised light at several incident angles. Figure 3 shows typical measurement results where the interference phase is scanned with the motor-controlled glass wedge.

From Fig. 3 the maximal modulation depth $m_{\max}$ is calculated by

$$m_{\max} = \frac{I_{\text{ac}\max} - I_{\text{ac min}}}{\left(I_{\max} - I_{\min}\right)}, \tag{1}$$

where $I_{\text{ac max}}$ and $I_{\text{ac min}}$ are the AC maximal and minimal modulated signal amplitudes, $I_{\max}$ and $I_{\min}$ are the maximal and minimal values of DC signal obtained from the MZI phase scan. The maximal modulation depth is a dimensionless number used to describe the relative AC modulation intensity.

2.1. Description of the MZI output

The EO coefficient tensor r_{ijk} characterises the ability of a material to change its refractive index n when low frequency electric field E is applied:

$$\left(\frac{1}{\Delta n^2}\right) = \sum_k r_{ijk} E_k . \tag{2}$$

Due to Kleinman symmetry, r_{ijk} can be rewritten as r_{il} which is a 6 × 3 tensor. In a poled polymer with point group symmetry of $C_{\infty V}$ the effective EO coefficient can be rewritten for *s* polarised light as [15]

$$r_{\text{ef}} = r_{13} \tag{3a}$$

and for *p* polarised light as

$$r_{\text{ef}} = r_{13} \cos^2 \alpha + r_{33} \sin^2 \alpha, \tag{3b}$$

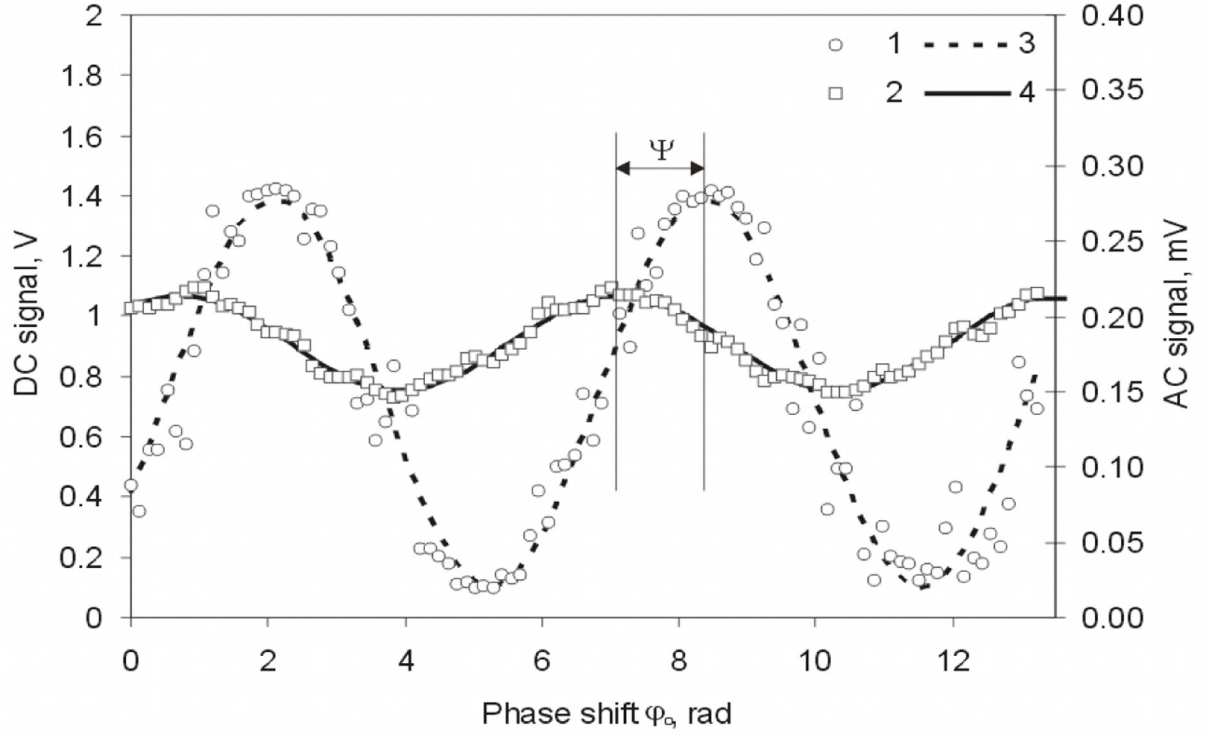

Fig. 3. Typical EO measurement performed at 8° incidence angle and *s* polarised light: *1* I_{DC} signal experimental data, *2* I_{AC} signal experimental data, *3* I_{DC} signal sin approximation, *4* I_{AC} signal sin approximation; Ψ is AC and DC signal maxima phase difference.

where r_{13} and r_{33} are the EO coefficients, and α is the angle between the sample normal and light propagation direction.

The light intensity at the MZI output can be described by the two beam interference equation:

$$I_{01} = \frac{1}{2}\left[I_r + TI_s + 2\sqrt{I_r TI_s}\cos(\varphi_0 + \varphi)\right], \quad (4)$$

where I_r is light intensity in the reference arm, I_s is light intensity in the sample arm without the sample, φ_0 is interference phase difference (adjustable by phase shifter), T is transmission coefficient of the sample, φ is additional phase difference caused by the sample.

If an AC electrical field is applied to the sample the transmission T and phase φ are also modulated as affected by several parameters, e. g. the refractive index, light polarisation, sample thickness etc., with corresponding changes in the detected output light intensity and therefore the AC signal amplitude. Some parameters, e. g. thicknesses and complex refraction indices for each layer could be obtained from independent experiments. The unknown is the effective coefficient r_{ef} of EO active layer that we would like to determine from our MZI experiment. To describe the intensity and phase of light transmitted through the sample at a certain applied voltage one can use the Abelès matrix formalism [16].

3. Results and discussion

According to our observations, for sample 1 the maximal modulation depth m_{max} decreases as the incidence angle is increased. This dependence could not be explained just by multiple internal reflection effects. To describe experimental data adequately, sample thickness modulations needed to be included in our model. Thickness change can be caused by electrostriction or piezoelectric effects. To prove the existence of these effects and evaluate the magnitude of sample thickness modulation we used the MZI method in the reflection configuration [10]. In this case the ITO glass slide covered by a spin coated polymer thin film (~1 μm) was not enclosed by another slide, but a reflective 100 nm thick Al layer was deposited on the polymer. Then one of the mirrors (M_2, see Fig. 1) in our MZI set-up was replaced

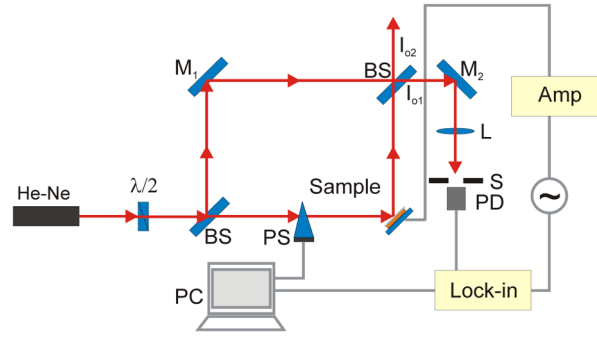

Fig. 4. Experimental set-up of MZI in reflection configuration for determination of a thin organic film thickness changes: helium-neon laser 632.8 nm *He–Ne*, half wave plate $\lambda/2$, beam splitter *BS*, minors M_1 and M_2, phase shifter *PS*, sample, photodiode *PD*, lock-in amplifier *Lock-in*, amplifier *Amp*, computer *PC*.

by the sample with the Al layer facing the incident beam (see Fig. 4). The Al layer was thicker than for sample 2 so that light would not penetrate into the sample. In this configuration, when voltage is applied to electrodes, electric field can cause sample thickness changes, thereby changing the position of Al mirror surface and thus mechanically altering the optical path length in the sample arm of the MZI. To evaluate the actual thickness change of the sample the modulation depth equation is modelled for phase modulation only due to changes in the sample arm path length. In this case the average light intensity at the MZI output, or DC signal, has a phase difference of π/2 with respect to the 4 kHz AC modulated signal amplitude since the beam intensities in both arms, I_r and I_s, remain constant.

For a modulation depth (Eq. (1)) of 7×10^{-5}, which is the maximal measured modulation depth of an unpoled sample, the sample thickness alteration of approximately 14 pm was estimated. In Fig. 5 we present the modulation depth determined according to Eq. (1) as a function of applied modulation voltage. The maximal modulation depth dependence on modulation voltage exhibits a quadratic and a linear component caused by electrostriction and piezoelectric effects, respectively. Moreover, both of these effects are more pronounced for the poled polymer films.

In Fig. 6 the maximal modulation depth of sample 1 (see Table 1) at different light incidence

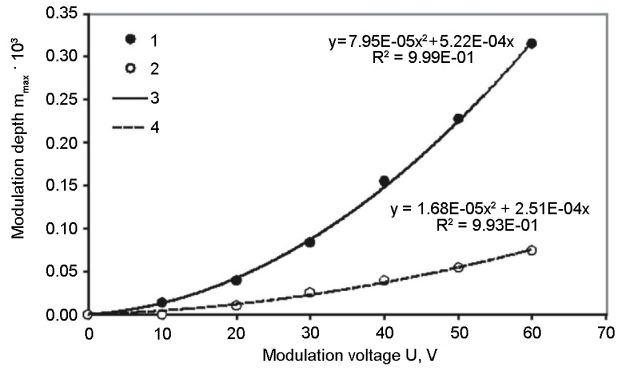

Fig. 5. Modulation depth m_{max} as a function of modulation voltage U for a MZI in the reflection configuration. Quadratic function regression is applied: *1* modulation depth m_{max} of poled film, *2* modulation depth m_{max} of unpoled film, *3* quadratic approximation of modulation depth m_{max} of poled film, *4* quadratic approximation of modulation depth mmax of unpoled film.

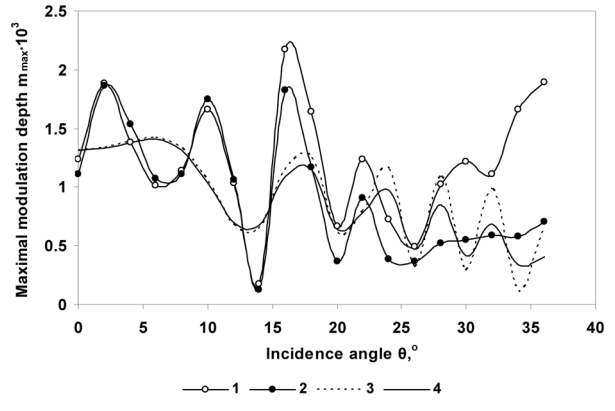

Fig. 6. Modulation depth dependence on the incidence angle in MZI in the transmission configuration for sample 1: *1*, *2* experimental data for *s* and *p* polarised light, respectively; *3*, *4* numerical approximation with MatLab performed using functions based on Abeles matrix formalism.

angles is shown. The measurement is performed by MZI in the transmission configuration by applying 50 V rms on the sample. The most important thing to notice in Fig. 6 is that the maximal modulation depth of *s* polarised light is higher than of *p* polarised light. From Eqs. (3a) and (3b) we would expect the refractive index change and therefore the maximal modulation depth for *p* polarised light to be higher as the effective EO coefficient is a combination of both r_{13} and r_{33}. In case of *s* polarised light the modulation depth should be dependent only on r_{13}. However, due to electrostriction and piezoelectric effect the sample thickness changes take place in addition to refractive index changes so that both the light phase and the amplitude are modulated causing the modulation depth decrease for greater incidence angles. The modelling is performed by refining the preliminary experimental results of a thin film and air gap thicknesses and varying the EO coefficients r_{13} and r_{33} and sample thickness alteration Δl due to electrostriction and piezoelectric effects.

For approximation of sample 1 experimental data we used a simple ITO-polymer-air gap-ITO layer system (Fig. 2 and Table 1) and glass as input and output media. This approach neglects interference effects caused by multiple light reflections within the glass slides and therefore theoretical lines are much smoother than experimental. Of course we could take into account glass slides as additional layers in our approximation. In that case noise-like interference fringes are superposed on the curves. The angular spacing of these fringes is well below the experimental incidence angle resolution. After performing the first numerical approximations for sample 1 we found that the modulation depth is a linear combination of NLO active layer thickness and EO modulations. When the EO coefficients were calculated taking into account a thickness modulation amplitude in the range of several tens of pm, the obtained r_{33} to r_{13} ratio ~10 and r_{33} value close to 100 pm/V were obviously too high. The ratio of r_{33} to r_{13} can be estimated by measuring the ratio of NLO coefficients d_{33} and d_{13}. Both EO and NLO coefficients characterise the material nonlinearity and are proportional to the second order polarisability $\chi^{(2)}$, but are used to describe the nonlinearity at different interactions and conditions. The NLO coefficient ratio d_{33}/d_{13} (nominally the same as r_{33}/r_{13} [17]) measurements performed by the second harmonic generation Maker fringe technique on the same sample yielded a value of 1.86. This suggests that the modulation is mainly caused by some effect other than EO variations. As described above the modulations could be caused by thickness changes in the polymer layer. The air gap (Fig. 2) thickness modulations can also take place as shown previously [18]. Therefore, the final modelling was performed allowing only air gap and NLO active layer thickness modulations Δl_{air} and

Δl, respectively. As it turned out in such case the calculated modulation depth was in good agreement with experimental data. The experimental data and best fit are shown in Fig. 6. The approximation values are shown in Table 2.

Table 2. Sample 1 parameters calculated from numerical approximation results.

Parameter	Value
Thickness l	0.85 ± 0.05 μm
Air gap	5.85 ± 0.10 μm
Δl_{air}	170 ± 5 pm
Δl	76.5 ± 1.0 pm

From comparison of data in Tables 1 and 2 one can see that the sample (polymer film) and air gap thicknesses are in good agreement with the preliminary experimental results. As expected, with thickness changes of air gap and NLO active layer, one can have a good approximation of modulation depth values.

The dependence of modulation depth on the incidence angle for sample 2 can be seen in Fig. 7. After measuring the dependence of modulation depth on the applied voltage we found that the dependence was linear. As thickness changes in the sample were expected to be quadratic, we consider that the effect of thickness change in this case has a small influence on the total modulation depth. Therefore, we excluded the sample thickness change effect in approximation by leaving only EO modulations. The approximation can be seen in Fig. 7. The numerical fit values can be seen in Table 3.

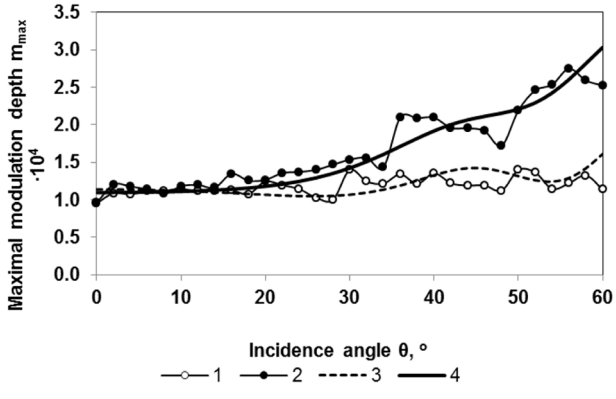

Fig. 7. Modulation depth dependence on the incidence angle in MZI in the transmission configuration for sample 2: *1*, *2* experimental data for *s* and *p* polarised light, respectively; *3*, *4* numerical approximation with MatLab performed using functions based on the Abeles matrix formalism.

Table 3. Sample 2 parameters calculated from numerical approximation results.

Parameter	Value
Thickness l	1.34 ± 0.05 μm
r_{13}	0.19 ± 0.02 pm/V
r_{33}	0.55 ± 0.06 pm/V

4. Conclusions

Both EO coefficients (r_{13} and r_{33}) of poled polymer films can be determined by applying the Abelès matrix formalism for numerical approximation of experimental MZI data at different incidence angles. However, one has to consider the sample structure. If an air gap is formed in the sample, the modulated signal in the MZI is usually generated by the air gap thickness modulations. The thickness modulations in the NLO active layer are also to be taken into account. An experimental procedure and data modelling are demonstrated for determining the EO coefficients of a poled PMMA + DMABI 10 wt% thin film. The obtained values are $r_{13} = 0.19 \pm 0.02$ pm/V and $r_{33} = 0.55 \pm 0.06$ pm/V.

Acknowledgements

This research was granted by ERDF 2.1.1.1 activity project No. 2010/0308/2DP/2.1.1.1.0/10/APIA/VIAA/051 "Development of Polymer EO Modulator Prototype Device" and Latvian National Research Program "Development of Innovative Multifunctional Materials, Signal Processing and Information Technologies for Competitive Science Intensive Products".

References

[1] L.R. Dalton, Rational design of organic electro-optic materials, J. Phys. Condens. Matter **15**, 897–934 (2003).

[2] A. Knoesen, M.E. Molau, D.R. Yankelevich, M.A. Mortazavi, and A. Dienes, Corona-poled

nonlinear polymeric films: in situ electric field measurement, charectarization and ultrashort-puls applications, Int. J. Nonlinear Opt. Phys. **1**(1), 73–102 (1992).

[3] M. Aillerie and N. Theofanous, Measurement of the electro-optic coefficients: description and comparison of the experimental techniques, Appl. Phys. B **70**, 317–334 (2000).

[4] C.C. Teng and H.T. Man, Simple reflection technique for measuring the electro-optic coefficient of poled polymer films, Appl. Phys. Lett. **56**(18), 1734–1737 (1990).

[5] W.H.G. Horsthuis and G.J.M. Krijnen, Simple measuring method for electro-optical coefficients in poled polymer waveguides, Appl. Phys. Lett. **55**(7), 616–618 (1989).

[6] C. Maertens, C. Detrembleur, P. Dubois, R. Jérôme, R. Blanche, Ph.C. Lemaire, Synthesis and electrooptic properties of a new chromophore dispersed or grafted in a carbazolyl methacrylate matrix, Chem. Mater. **10**, 1010–1016 (1998).

[7] M. Sigelle and R. Hierle, Determination of electrooptic coefficients of 3-methyl 4-nitropyridine 1-oxide by an interferometric phase-modulation technique, J. Appl. Phys. **52**(6), 4199–4204 (1981).

[8] M.J. Shin, H.R. Cho, J.H. Kim, S.H. Han, and J.W. Wu, Optical interferometric measurement of the electro-optic coeffcient in nonlinear optical polymer films, J. Korean Phys. Soc. **31**(1), 99–103 (1997).

[9] R. Meyrueix and O. Lemonnier, Piezoelectrically induced electrooptical effect and dipole orientation measurement in undoped amorphous polymers, J. Phys. D: Appl. Phys. **27**, 379–386 (1994).

[10] C. Greenlee, A. Guilmo, A. Opadeyi, R. Himmelhuber, R.A. Norwood, M. Fallahi, J. Luo, S. Huang, X.H. Zhou, A.K.Y. Jen, and N. Peyghambarian, Mach-Zehnder interferometry method for decoupling electro-optic and piezoelectric tensor components in poled polymer films, Proc. SPIE **7774**, 77740D–2 (2010).

[11] F. Qui, X. Cheng, K. Misawa, and T. Kobayashi, Multiple reflection correction in the determination of the complex electro-optic constant using a Mach-Zehnder interferometer, Chem. Phys. Lett. **266**, 153–160 (1997).

[12] P. Nagtegaele, E. Brasselet, and J. Zyss, Anisotropy and dispersion of a Pockels tensor: a benchmark for electro-optic organic thin-film assessment, J. Opt. Soc. Am. B **20**(9), 1932–1936 (2003).

[13] F. Abelès, La détermination de l'indice et de l'épaisseur des couches minces transparentes, J. Phys. Radium **11**(7), 310–314 (1950).

[14] M. Rutkis, A. Vembris, V. Zauls, A. Tokmakovs, E. Fonavs, A. Jurgis, and V. Kampars, Novel second-order nonlinear optical polymer materials containing indandione derivatives as a chromophore, Proc. SPIE **6192**, 61922Q (2006).

[15] R.A. Norwood, M.G. Kuzyk, and R.A. Keosian, Electro-optic tensor ratio determination of side chain copolymers with electro-optic interferometry, J. Appl. Phys. **75**(4), 1869–1874 (1994).

[16] S. Larouche and L. Martinu, OpenFilters: open-source software for design, optimization, and synthesis of optical filters, Appl. Opt. **47**(13), C219–C230 (2008).

[17] O. Ahumada, C. Weder, P. Neuenschwander, and U.W. Suter, Electro-optical properties of waveguides based on a main-chain nonlinearo-optical polyamide, Macromolecules **30**, 3256–3261 (1997).

[18] E. Nitiss, M. Rutkis, and O. Vilitis, Determination of electro-optic coefficient of thin organic films by Mach-Zehnder interferometric method, Latv. J. Phys. Tech. Sci. **46**(3), 5–14 (2009).

DAUGKARTINIO VIDINIO ATSPINDŽIO IR BANDINIO STORIO KITIMO ĮTAKA POLIMERINIO SLUOKSNIO ELEKTROOPTINIŲ KOEFICIENTŲ VERČIŲ NUSTATYMUI

E. Nitišs [a], M. Rutkis [a], M. Svilans [b]

[a] *Latvijos universiteto Kietojo kūno fizikos institutas, Ryga, Latvija*

[b] *Rygos technikos universiteto Medžiagotyros ir taikomosios chemijos fakultetas, Ryga, Latvija*

Santrauka

Naujos organinės netiesiškai optiškai aktyvios medžiagos yra naudojamos optoelektroniniuose ir fotoniniuose taikymuose. Tokių medžiagų tinkamumas minėtiems taikymams gali būti vertinamas pagal jų elektrooptinius (EO) koeficientus. Mes pritaikėme Macho ir Cėnderio (Mach–Zehnder, MZ) interferometrijos metodą plonų organinių sluoksnių EO koeficientams nustatyti. Nepaisant daugybės kitų EO koeficientų nustatymo ploniems sluoksniams optinių metodų, šį metodą pasirinkome todėl, kad jis pasižymi dideliu jautrumu fazės ir intensyvumo moduliacijoms interferometro bandinio petyje ir leidžia nepriklausomai matuoti abu plonojo sluoksnio EO koeficientus – r_{13} ir r_{33}. Parodėme, kad elektrostrikcija ir daugkartiniai vidiniai atspindžiai bandinyje stipriai veikia šviesos intensyvumą MZ interferometro išėjime. Atsižvelgdami į šiuos reiškinius, skaitmeniškai naudodami Abelės matricų formalizmą, sumodeliavome EO koeficientų poveikį MZ interferometro signalo kaitai arba moduliacijos gylį esant skirtingiems kritimo kampams. Pavyko parodyti, kad moduliuotas signalas MZ interferometro išėjime labai priklauso nuo bandinio sandaros ir yra stipriai lemiamas EO koeficientų. Moduliuoto signalo sandų analizei ir plonų polimerinių sluoksnių EO koeficientų nustatymui atlikome keliolika eksperimentų su PMMA ir 10 svorio % DMABI bandiniais.

Simple method for measuring bilayer system optical parameters

E. Nitiss*, R. Usans, M. Rutkis

Institute of Solid State physics, University of Latvia, Latvia

* *Corresponding author: edgars.nitiss@cfi.lu.lv*

ABSTRACT

A simple method for measuring bilayer system refractive indexes and thicknesses in the low absorbing part of spectra is demonstrated. The method is based on application of Savitzky – Golay smoothing filters and interference fringe separation in the reflected or transmitted spectra of the bilayer system. The refractive indexes and thicknesses are extracted from the wavelengths corresponding to extreme points in the spectrum. Due to the fact that wavelength difference of extreme points in the analyzed spectrum is defined by the product of both, the layer thickness and refractive index, one must generate an appropriate initial guess of these parameters. For refractive index approximation two different methods have been used – point by point and Sellmeier dispersion relation. The final optimization procedure is based on *a priori* assumption that the thickness calculated from permutations of all extreme points in the spectrum should be the same. Thus the optimal penalty parameter for finding the solution is the standard deviation of calculated thicknesses. In order to demonstrate the effectiveness of this simple method, results of thin organic film thicknesses and refractive indexes are presented.

INTRODUCTION

Thin layers as optical components are applied more and more frequently in novel optoelectronic devices. For development of such devices it is important to know the linear optical parameters and thicknesses of the layers which are determined experimentally. To avoid mechanical interaction with the sample commonly optical methods such as single wavelength or spectral ellipsometry [1-3], spectral interferometry [4], spectral reflectometry [5,6] and transmission spectroscopy [7] are used. With most of the mentioned methods it is possible to obtain the product of refractive index and thickness with a very high precision, even for samples with thickness of a couple of tens of nanometers. However, most of them require using sophisticated functions for transmission or reflection data approximation.

We propose a simple method for measuring bilayer system optical parameters in the low absorbance part of the sample transmittance or reflectance spectrum. Even though similar methods for single layer optical parameters have been proposed and used earlier [8,9] we have extended the application for bilayer systems and implemented specific penalty parameters for optimal method performance.

In this method the thicknesses and refractive indexes are determined by separating the interference fringes for each layer. Thus a mandatory requirement in order to have at least one exact solution of problem is that the layer

Optical Micro- and Nanometrology IV, edited by Christophe Gorecki, Anand K. Asundi, Wolfgang Osten, Proc. of SPIE Vol. 8430, 84301C · © 2012 SPIE · CCC code: 0277-786X/12/$18 · doi: 10.1117/12.922317

thicknesses must be comparable to light wavelength to have more than one interference fringe in the spectrum. The fringes are then separated by applying Savitzky – Golay smoothing filters [10] with two different orders of polynomial fits and window lengths. Eventually the wavelength values which correspond to the extreme points in the spectrum are obtained. For finding the solution of thicknesses and refractive indexes these values are then approximated using standard deviation of thicknesses as the penalty parameter.

To demonstrate the effectiveness of this method results of single thin organic film and bilayer system thicknesses and refractive indexes are presented. The system under investigation was ITO glass slide coated with polymer film and covered with another ITO glass slide. Such configuration is frequently used for NLO polymer poling where electric field is applied to a polymer layer. To estimate the poling fields it is necessary to know the thicknesses of each layer in the sample [11,12].

METHOD DESCRIPTION

The reflection spectroscopy is based on collecting reflected from the multi interface system and can be used to determine the optical path length of certain layers in the system. A schematic representation of light propagation in thin film is shown in Fig. 1. An incident light I_o on film is reflected from air – thin film and thin film – substrate interface. The reflected and transmitted light intensity I_R and I_T depend on refractive indexes of each layer and the thickness of thin film in which multiple internal reflections can take place. In such case in the reflected spectrum interference fringes can be noticed. The period of these fringes is determined by the optical path length of the thin film which is a product of refractive index and thickness.

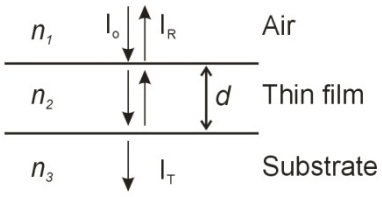

Fig. 1 Light propagation in a thin film where n_1 – refractive index of air, n_2 and d – refractive index and thickness of thin film respectively, n_3 – refractive index of substrate, I_o – incident light intensity, I_R – reflected light intensity, I_T – transmitted light intensity.

The reflectivity R of the non-absorbing thin film at zero light incidence angle can be calculated by

$$R = \left| \frac{r_{12} + r_{23} \exp(-2i\delta)}{1 + r_{12} r_{23} \exp(-2i\delta)} \right|^2 . \quad (1)$$

where

$$\delta = \frac{2\pi n_2 d}{\lambda}, \quad (2)$$

and r_{12} and r_{23} are the Fresnel coefficients [13] of the air – thin film and thin film – substrate interfaces respectively, λ - wavelength. The theoretical plot of reflectivity R of air - thin film – glass substrate system with refractive indexes of 1,

1.54 and 1.5 respectively and the film thickness of 1 μm as a function of wavelength λ according to (1) is shown in Fig. 2.

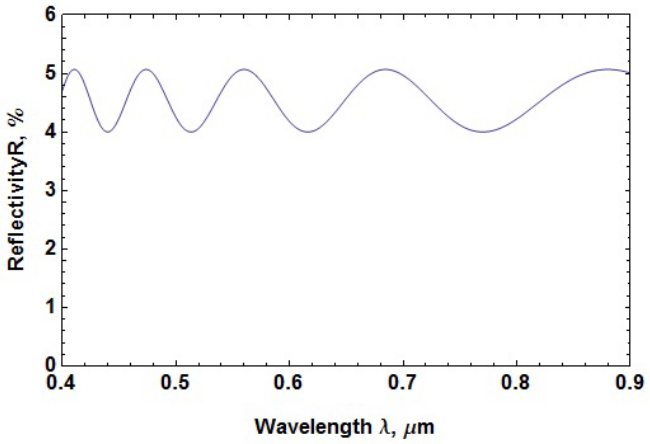

Fig. 2 The reflectivity *R* of air - thin film – glass substrate with refractive indexes of n_1=1, n_2=1.54 and n_3=1.5 respectively as a function of wavelength λ, thin film thickness *d*=1 μm.

However, the experimentally obtained reflectivity curve is usually not as smooth as the one shown in Fig. 2. It needs to be filtered to reduce the noise and be able to extract the wavelengths which correspond to the extreme points in the reflectivity curve. Thus to the collected raw data we apply the Savitzky-Golay smoothing (SG) filters [10,14]. The polynomial order and their window length can be varied. For fringes with longer periods usually SG filters with wider windows could be applied.

From the reflectivity data such as shown in Fig. 2 one can obtain the wavelengths λ_i and λ_j which correspond to the *i*-th and *j*-th of total *k* extreme points in the reflectance spectra. Afterwards, the thickness and refractive index of the thin can be calculated by

$$d_{ij} = \frac{j-i}{4\cdot\left[\frac{n_2(\lambda_i)}{\lambda_i} - \frac{n_2(\lambda_j)}{\lambda_j}\right]}, \tag{3}$$

where $i < j$. If we assume that $d_{ij}=d$ then solution for thickness *d* and refractive indexes $n_2(\lambda_i)$ can be found by an optimization procedure minimizing the penalty parameter *S*. We have chosen the penalty parameter *S* to be

$$S = \sqrt{\frac{1}{N}\sum_k \left(d_i - \overline{d}\right)^2}, \tag{4}$$

where *N* is the number of thicknesses calculated

$$N = \frac{k!}{2\cdot(k-2)!}. \tag{5}$$

Equation (5) shows that permutation of all points is used for thickness calculation thus increasing the credibility of the solution. For dispersion relation we use two type of methods – point by point where refractive index at each λ_k is calculated independently and Sellmeier equation [13] which can be expressed as

$$n_2(\lambda) = \sqrt{A + \frac{B\lambda^2}{|\lambda^2 - \lambda_o^2|}}, \quad (6)$$

where λ_o is the resonance frequency and A and B are characteristic constants.

The code and graphical user interface for calculation of optical parameters of layers is created in Matlab.

EXPERIMENTAL

For the method testing a single layer and bilayer samples were made. For single layer thin film a polymer sample, NLO host/guest polymer PMMA+DMABI 10 wt% (for detailed molecular structure see ref. [15]) was spin-coated from a chloroform solution onto a high refractive index ITO covered glass slide (SPI Supplies, ITO thickness 15 – 30 nm) as shown in Fig. 3(a). This polymer films were coated at different thicknesses by changing the concentration of the chloroform solution. Bilayer system was obtained by covering an ITO glass slide carrying the polymer film with another bare ITO glass slide. Afterwards both slides are squeezed together in the sample holder creating a system as shown in Fig. 3(b). On the micron scale the surface of the polymer sample, especially at slide edges, is rather rough causing the formation of an air gap between the surface of the polymer and second ITO layer thus a bilayer system in the micron scale is created.

The parameters of such sample structure are of a particular interest when it is necessary to apply en electric field to the polymer film, e.g., when NLO polymers are poled. Poling is a procedure during which under elevated temperatures an electric field is applied to a thin film to create overall NLO activity of the film. The effective electric field in the film is also referred as the poling field. The higher poling field is applied the higher the nonlinearity of the material could be achieved [11]. In case an air gap is formed between the electrodes, a significant part of applied voltage on the electrodes drops on the air gap causing reduction of the poling field [12]. In order to calculate the poling field one must know the thicknesses of the air gap and the thin polymer film, which can be calculated by the proposed interference fringe separation method.

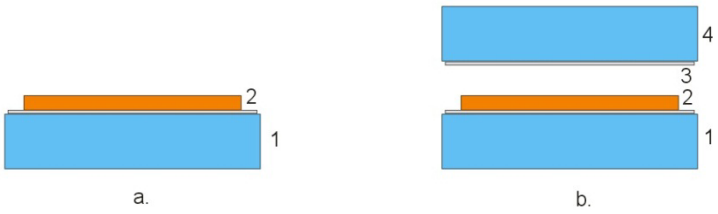

Fig. 3 Sample geometry a) single layer thin film sample: 1- ITO coated glass, 2 - PMMA+DMABI 10 wt% polymer. b) bilayer sample: 1, 4 - ITO coated glass, 2 - PMMA+DMABI 10 wt% polymer, 3 - air gap.

For the spectral reflectometry measurements we used a simple experimental configuration. The light from a light source (*OceanOptics* Mini-D2-GS) is transmitted through a reflection probe (*OceanOptics* QR200-7-VIS-NI) to the sample. The reflected light form the sample is then collected and transmitted to the spectrometer (*OceanOptics* HR4000CG-UV-NIR).

RESULTS AND DISCUSSIONS

First, the proposed method is tested on a single layer thin film such as shown in Fig. 3(a). The collected raw data, SG filtered data and extreme points are shown in the Fig. 4 and the calculated refractive index as a function of wavelength is shown in Fig. 5. As the thin film PMMA+DMABI 10 wt% has an absorption peak ~490 nm, the spectral data were registered in the non-absorbing wavelength region from 570 to 900 nm. The calculated thickness for this particular sample was 2.38±0.01 μm (point by point) or 2.39±0.21 μm (Sellmeier). Obviously, using the point by point dispersion relation one would obtain a thickness that mathematically would have smaller error than the one extracted by Sellmeier relation. However, by using Sellmeier dispersion relation a higher credibility of the approximated refractive index as a function of wavelength will take place.

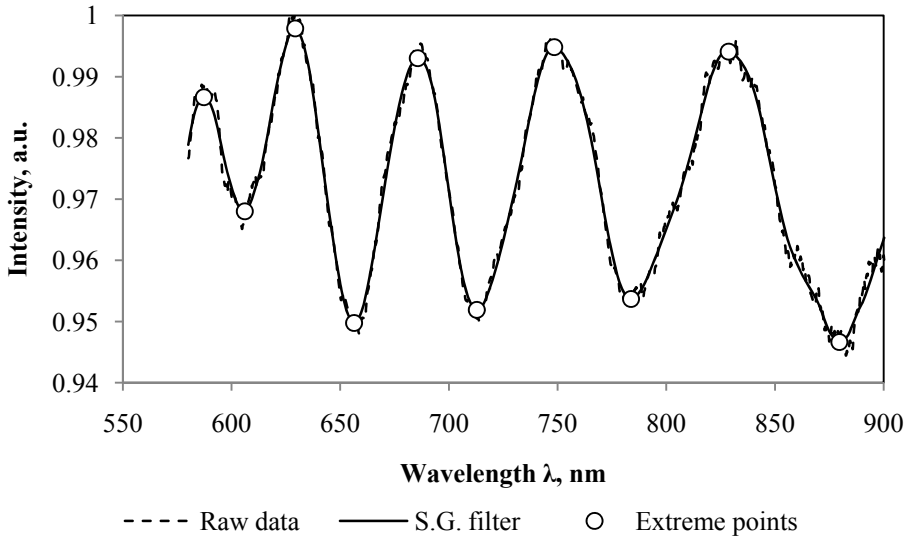

Fig. 4 Raw data, SG filtered data and extreme points in the reflected spectra. SG filter of third order and 121 points window length is applied.

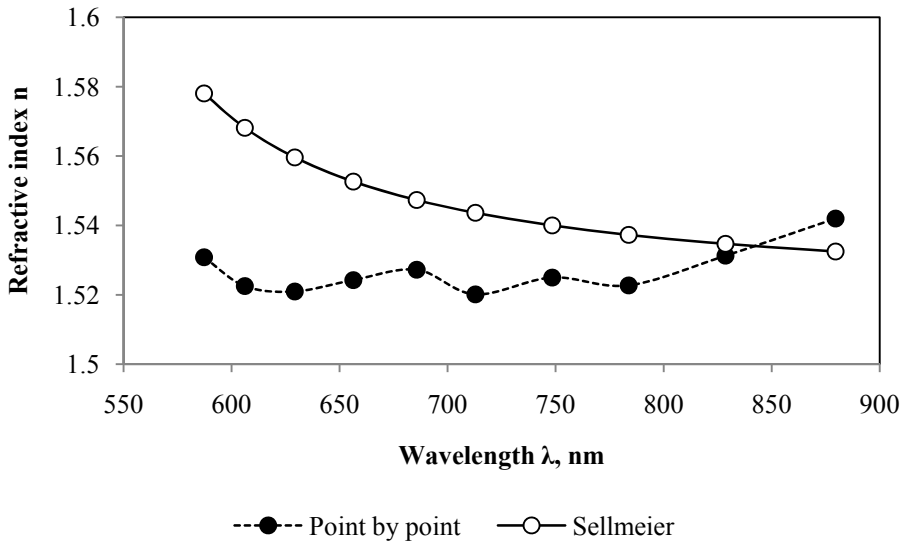

Fig. 5 Refractive index as a function wavelength calculated both by point by point and Sellmeier dispersion relation

To verify the calculated thicknesses of the thin films we compared the results with the ones obtained by the ATR technique described in [1]. As can be seen from Fig. 6 the thicknesses obtained by both techniques give almost the same results. Moreover, more reliable results are obtained if Sellmeier dispersion relation in the optimization procedure instead of point by point is used. However, there are cases when optimization fails to give good results if refractive index is characterized by the Sellmeier dispersion relation. It is also important to note that from some thin films we were not able to extract extreme points from reflected spectra which give us a plausible result for thin film parameters. In fact it was not possible for those thin films the surface roughness of which was above 100 nm. The surface irregularities cause the reflected light to be in different phase at different points in reflected light wave front. Thus the result of collecting reflected light from an irregular surface causes irregularities in the reflected light spectrum.

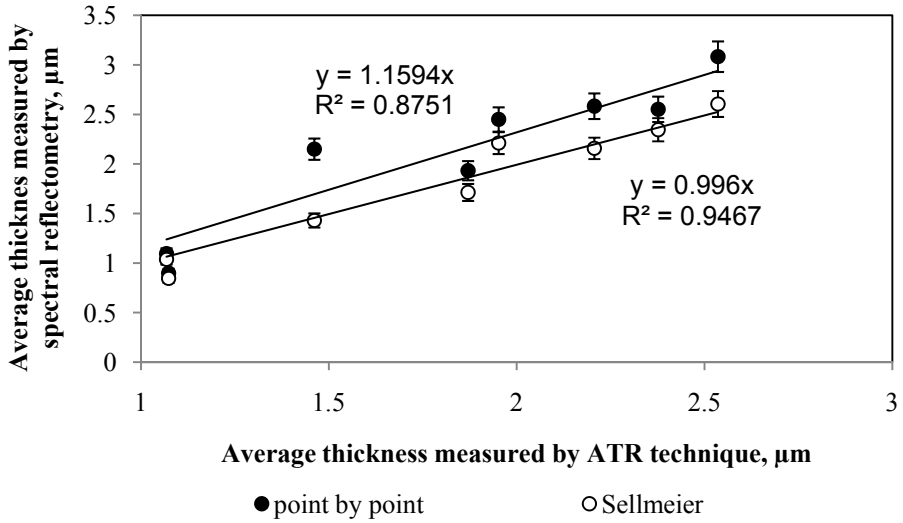

Fig. 6 Average thicknesses measured by spectral reflectometry and ATR technique using different dispersion relation approximations

The technique described above could be applied to a bilayer system. From a bilayer sample such as shown in Fig. 3(b) the collected light intensity spectral dependence or the raw data are shown in Fig. 7. It is clearly evident that the spectral intensity is governed by interference effects in two layers with different optical path lengths. In the reflected light spectrum the wavelength separation of fringes caused by the thicker layer should be smaller and for the thinner ones larger. Thus it is assumed that the long period fringes are caused by interference in the thin film, but the short period ones caused by the interference in the air layer. The optical parameters for each of the layers one can obtain by separation of the interference fringes. However, there are two conditions that must be meet in order to have sufficiently high contrast and different period of the interference fringes. First, method is applicable in case when the bilayer system is built from materials with high enough refractive index contrast. The higher refractive index contrast, the higher interference fringe amplitude will be registered. Second, interference fringe periods depend on the optical path length of the individual layer. To have interference fringes that can clearly be separated by SG filtering the layers must have optical path lengths that differ at least a couple of times.

For the collected raw data at first we apply SG filter with a 701 points wide window length to extract the interference fringe corresponding multiple internal reflections in the thin film. For the sake of clarity SG filter with such parameters will be referred as 1st SG filter. From the filtered data three extreme points are found. Using these points layer thickness and refractive indexes at three light frequencies are calculated applying the point by point dispersion relation. The calculated thickness of the thin film is 0.73±0.01 µm using the point by point and 0.91±0.01 µm using the Sellmeier dispersion relation. The corresponding thin film refractive indexes are show in Fig. 8. Unfortunately, in this case we were not able to get a good refractive index approximation using the Sellmeier dispersion relation. As can be seen from

Fig. 8 Sellmeier refractive index approximation gives anomalous dispersion however normal dispersion should take place. Such inadequate refractive index dispersion characteristics take place when there is low number of extremes and the extremes are smeared as seen in Fig. 7.

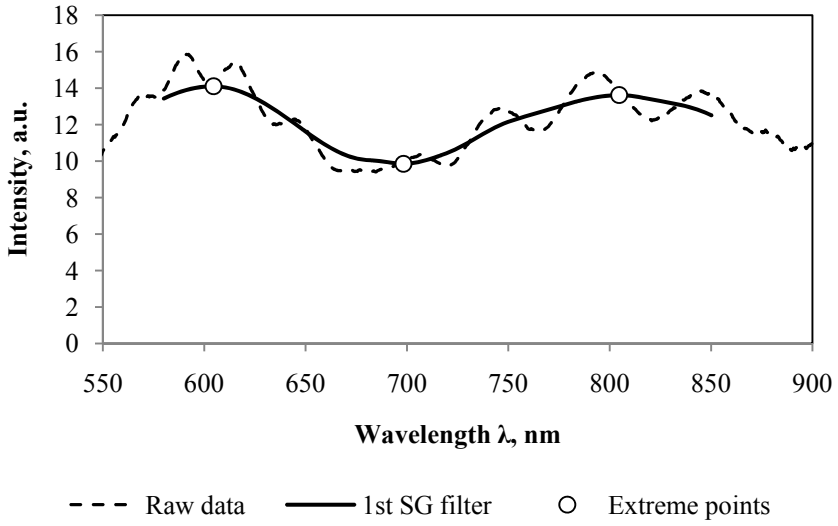

Fig. 7 Raw data, SG filtered data and extreme points in the reflected spectra. SG filter of third order and 701 points window length is applied.

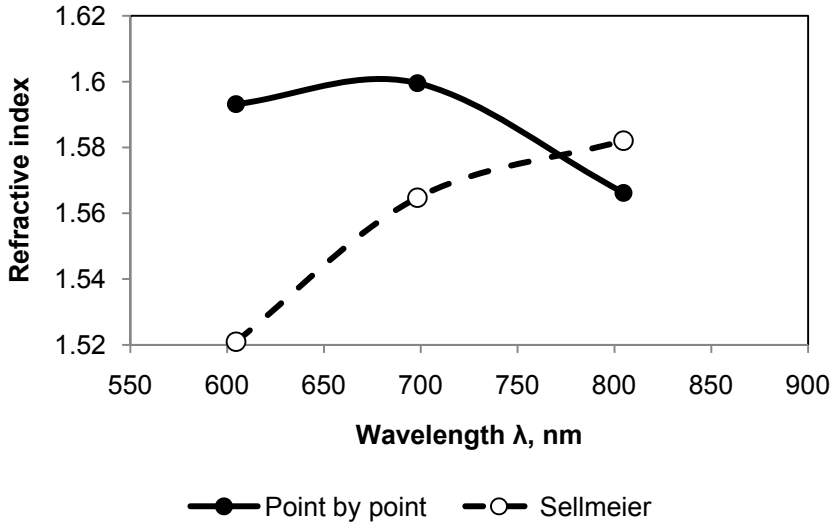

Fig. 8 Refractive index of polymer film as a function wavelength calculated by point by point dispersion relation

If the SG filtered values are subtracted from the raw data then the shorter period interference fringes can be separated. We will call these values the filtered raw data. From Fig.7 it can be seen that there are two wavelength ranges with shorter period interference fringes that are suitable for approximation. The ranges are 550 – 650 nm and 710 to 870 nm. Either of the two wavelength ranges can be used for determination of the layer parameters. The shorter period interference fringes or the filtered raw data in the spectral range from 710 to 870 nm are shown in Fig. 9. After application of SG filter of window length 101 points (2^{nd} SG filter) the wavelengths which correspond to the extreme points in the reflected spectra can be found. From these points the optical parameters of the air layer can be calculated giving layer thickness of 5.55±0.29 μm when using point by point method and 5.97±0.14 μm when using the Sellmeier dispersion relation in the 710 – 870 nm range. The refracted indexes are as shown in Fig. 10. For the 550 – 650 nm range the calculated thickness was 3.75±0.60 μm when using point by point method and 6.93±0.87 μm when using the Sellmeier dispersion relation. The results obtained from the extreme points in the 550 – 650 nm range show worse results which is explained by the adjacent absorption band.

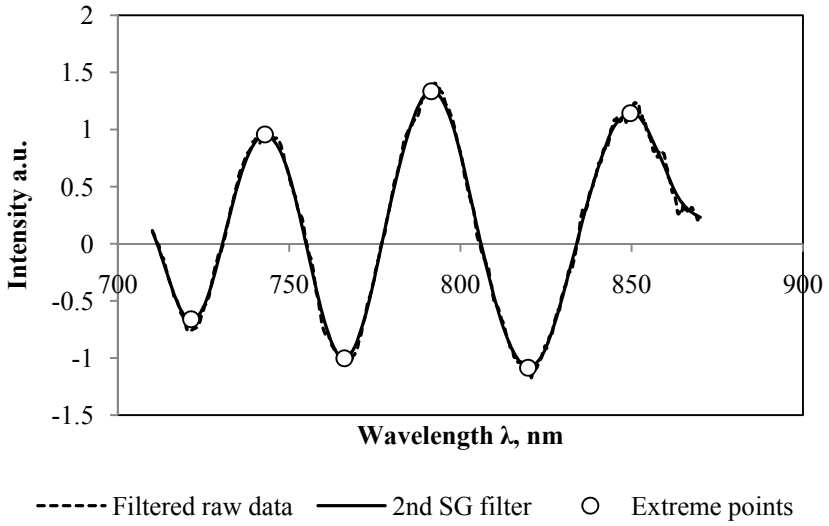

Fig. 9 Filtered raw data, SG filtered data and extreme points in the reflected spectra. SG filter of third order and 101 points window length is applied.

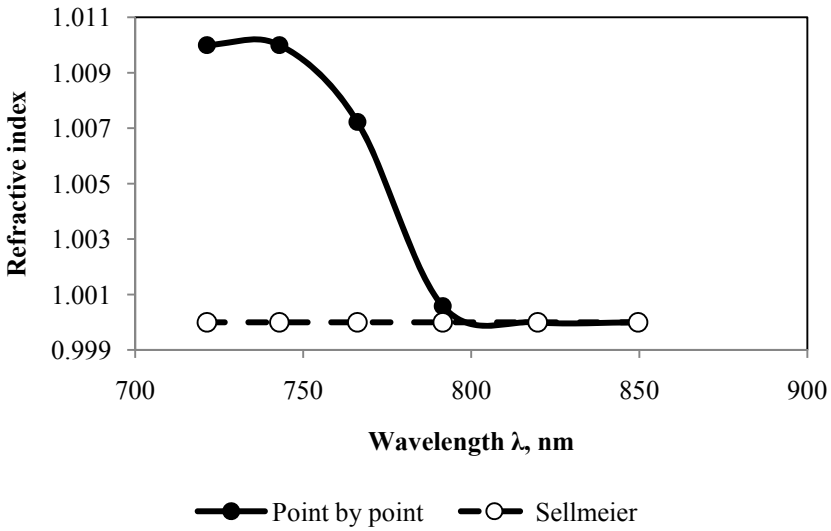

Fig. 10 Refractive index of air layer as a function wavelength calculated by point by point dispersion relation

CONCLUSIONS

We have applied a simple interference fringe separation technique for determination of refractive indexes and thicknesses of bilayer system. The optimal penalty parameter for finding the solution is the standard deviation of calculated thicknesses. For the thin film refractive index approximation point by point and Sellmeier dispersion relation was used. The comparison of results obtained by proposed method with the results obtained by the ATR technique confirmed that more reliable results are obtained in case when Sellmeier dispersion relation was used. Nonetheless, in some cases refractive index approximation with Sellmeier dispersion relation fails to give correct results. This is most probable to occur when approximation is performed for very thin films with few smeared extremes in the reflectance spectrum.

REFERENCES

[1] Swalen, J., D., "Optical Properties of Lanmuir-Blodget Films," Journal of Molecular Electronics 2, 155-181 (1986).

[2] Collins, R., W., An, I., Chen, C., Ferlauto, A., S., Zapien, J., A., "Advances in multichannel ellipsometric techniques for in-situ and real-time characterization of thin films," Thin Solid Films 469-470, 38-46 (2004).

[3] Franquet, A., De Laet, J., Schram, T., Terryn, H., Subramanian, V., Van Ooij, W., J., Vereecken, J., "Determination of the thickness of thin silane films on aluminium surfaces by means of spectroscopic ellipsometry," Thin Solid Films 384, 37-45 (2001).

[4] Costantino, S., Martínez, O., E., Torga, J., R., "Wide band interferometry for thickness measurement," Optics Express 11(8), 952-957 (2003).

[5] Etoh, K., "Determination method of optical properties," Applied Optics 34(1), 159-162 (1995).

[6] Hlubina, P., Luňáček, J., Ciprian, D., "Maxima of the spectral reflectance ratio of polarized waves used to measure the thickness of a nonabsorbing thin film," Optics and Lasers in Engineering 48, 786-791 (2010).
[7] Richards, B., S., Lambertz, A., Sproul, A., B., "Optical characterisation of sputtered silicon thin films on glass," 2nd WCPEC 1998b, 1294-1297 (1998).
[8] Manifacier, J., C., Gasiot, J., Fillard, J., P., "A simple method for the determination of the optical constants n, k and the thickness of a weakly absorbing thin film," J. Phys. E: Sci. Instrum. 9, 1002 - 1004 (1976).
[9] Khashan, M., A., El-Naggar, A., M., "A simple method of measuring and applying the dispersion of thin films," Optics Communications 187, 39-47 (2001).
[10] Savitzky, A., Golay, M., J., E., "Smoothing and Differentiation of Data by Simplified Least Squares Procedures," Analytical Chemistry 36 (8), 1627-1639 (1964).
[11] Dalton, L., R., Harper, A., W., Robinson, B., H., "The role of London forces in defining noncentrosymmetric order of high dipole moment- high hyperpolarizability chromophores in electrically poled polymeric thin films," Proc. Natl. Acad. Sci. USA Vol. 94, 4842-4847 (1997).
[12] Nitiss, E., Rutkis, M., Svilans, M., "Effects of the multiple internal reflection and sample thickness changes on determination of electrooptical coefficient values of a polymer film," Lithuanian Journal of Physics (article in press), xxx - (2012).
[13] Bass, M., Van Stryland, E., W., Williams, D., R., Wolfe, W., L., [Handbook of Optics], McGraw-Hill Professional, Second edition 1, 1 - 1664 (1995).
[14] Press, W., H., Flannery, B., P., Teukolsky, S., A., Vetterling, W., T., [Numerical Recipes in Fortran 77: The Art of Scientific Computing], Cambridge University Press, Second Edition 1, 1 - 933 (1992).
[15] Rutkis, M., Vembris, A., Zauls, V., Tokmakovs, A., Fonavs, E., Jurgis, A., Kampars, V., "Novel second-order nonlinear optical polymer materials containing indandione derivativatives as a chromophore, Proceedings of SPIE," Organic optoelectronics and photonics II 6192, 61922Q (2006).

Optics Communications 286 (2013) 357–362

Contents lists available at SciVerse ScienceDirect

Optics Communications

journal homepage: www.elsevier.com/locate/optcom

Electrooptic coefficient measurements by Mach Zehnder interferometric method: Application of Abelès matrix formalism for thin film polymeric sample description

E. Nitiss [a,*], M. Rutkis [a], M. Svilans [b]

[a] Institute of Solid State Physics, University of Latvia, Kengaraga 8, LV-1063, Riga, Latvia
[b] Faculty of Material Science and Applied Chemistry, Riga Technical University, Azenes 14/24, LV-1048 Riga, Latvia

ARTICLE INFO

Article history:
Received 15 December 2011
Received in revised form
4 September 2012
Accepted 6 September 2012
Available online 21 September 2012

Keywords:
Optical nonlinearities in organic materials
Interferometry
Phase modulation
Thin films
Optical properties
Other properties

ABSTRACT

In Mach–Zehnder interferometric (MZI) method for determination of thin organic film electrooptic (**EO**) coefficients r_{13} and r_{33} critical effects, like multiple internal reflections and sample thickness modulation due to electrostriction and piezoelectricity are usually overlooked. Ignoring these effects may lead to inaccurate calculation of EO coefficients from experimental data by the simplified equations. To describe the influence of the above mentioned effects on the output of a MZI containing a thin film polymer sample we have used the Abelès matrix formalism.

1. Introduction

Nonlinear optical (**NLO**) polymers have drawn considerable attention in the last couple of decades due to their potential for applications in electrooptic (**EO**) devices. Such organic EO materials are likely substitutes for the traditional inorganic ones, since they possess the advantages of easier processability, lower costs and higher nonlinearity coefficients [1]. High NLO activity is one of the most important material prerequisite for further successful application in EO devices. Therefore evaluation of this property is an important task for new material development.

Typically the organic EO material sample under investigation is a thin film spin-coated on an indium tin oxide (**ITO**) glass substrate and poled by an external electric field. Due to intrinsic properties of an oriented system in terms of EO performance, such a structure can be described by two EO coefficients—r_{13} and r_{33} [2]. Several optical methods have been applied to characterize the EO performance of organic materials. The most popular techniques are Teng–Mann reflection ellipsometry, attenuated total reflection (**ATR**) and Mach Zehnder interferometry (**MZI**) [3]. All of them possess some significant drawbacks. The widely used Teng–Mann technique can provide good measurement results of effective EO coefficient r_{ef} [4]. However, this technique is limited when it comes to determining both r_{13} and r_{33} independently. As r_{ef} is a function of r_{13} and r_{33}, the r_{33}/r_{13} ratio also needs to be known. Usually, if the film is poled at low poling fields ($\mu E < kT$), this ratio is assumed to be constant and equal to ~ 3 [5]. In contrast, with ATR r_{13} and r_{33} can be determined independently, however this method is quite complex and must be performed with high precision [6]. In spite of high sensitivity to acoustic and mechanical vibrations MZI techniques—both in transmission or in reflection mode—are being applied more and more often [7,8]. Researchers using the MZI technique in transmission mode have mostly excluded from their considerations multiple internal reflections and sample thickness change by electrostriction and piezoelectric effects. To our knowledge, there is a limited number of investigators who pay attention to these effects when determining EO coefficients of polymer films [9,10] and bulk crystals [11,12]. According to our observations, these effects can greatly contribute to the EO modulated AC signal maximal amplitude and location of that maximum in MZI phase shift scan. These effects become crucial when one would like to obtain both EO coefficients r_{13} and r_{33} from the EO modulated signal amplitude dependence on light propagation angle in the poled sample. The light intensity and phase transmitted by the multilayer EO sample can be described by Abelès matrix formalism [13,14]. An explicit analytical solution to EO modulations for a simple system in which only one layer is of thickness comparable to light wavelength has been shown earlier [15]. However, when expanding the system by adding glass and air layers and including thickness

* Corresponding author. Tel.: +371 29945814.
E-mail address: edgars.nitiss@cfi.lu.lv (E. Nitiss).

0030-4018/$ - see front matter © 2012 Elsevier B.V. All rights reserved.
http://dx.doi.org/10.1016/j.optcom.2012.09.020

modulation in polymer layer, the explicit analytical solution becomes too complicated. In this contribution we would like to present a numerical approximation for MZI transmission mode measurements of r_{13} and r_{33} using the closed form matrix formalism.

2. Experimental setup

We performed our EO measurements on a MZI setup as shown in Fig. 1. The sample was examined in transmission and reflection configurations. In contrast to reflection configuration, where the sample is used as a 45° mirror in the sample arm, using the transmission configuration we can obtain modulation amplitude values as a function of light incidence angle.

In our optical scheme we used a Helium–Neon laser (632.8 nm) as light source. Polarization of the incident light was controlled by halfwave plate $\lambda/2$. The beam is then split in sample and reference arms of the MZI by a 50/50 beam splitter. By means of a computer controllable translation stage and a small angle glass wedge in the reference arm the interference phase between the reference beam I_r and the sample beam I_s can be shifted and thus also the AC signal measurement point. To obtain an interference pattern the reference and sample beams are recombined by a second 50/50 beam splitter. A large area Si photodiode was used to capture the entire interference pattern. As the MZI is highly sensitive to any vibrations the elements of the optical setup must be fixed firmly. Ultra stable beam splitter and mirror holders are suggested. The modulation voltage was provided by a computer controlled lock-in amplifier (*Stanford Research Systems SR830*) and a driver amplifier (*Trek PZD350*). The light intensity modulation (AC signal) as well as overall MZI output light intensity (DC signal) was measured with the lock-in amplifier and recorded by the computer. It is important to note that the AC signal recovered by the lock-in amplifier contained a notable contribution of crosstalk from the sample drive signal, which could be recognized by its presence in the detection system with the laser turned off. The crosstalk creates an additional offset value in the signal detected by lock-in, not dependent on MZI phase.

Typically the polymer sample, PMMA+DMABI 10 wt% (for detailed molecular structure see ref. [16]), used in this investigation, was spin-coated from a chloroform solution onto an ITO covered glass slide (SPI Supplies, ITO sheet resistivity 70–100 Ω). The glass transition temperature of the sample is approximately 110 °C.

For EO measurements it is necessary to have the EO active layer between two electrodes or, in other words, in a sandwich type structure. Two main sandwich sample structures were used.

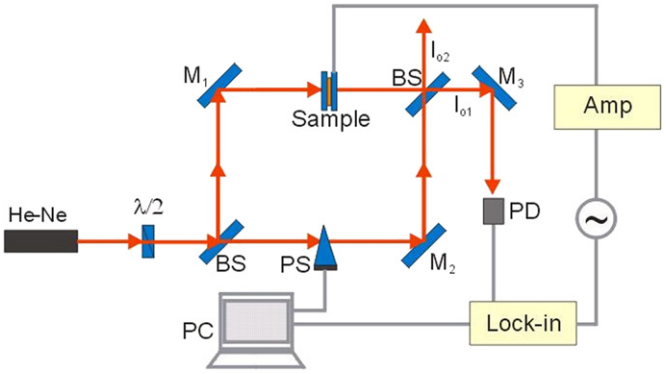

Fig. 1. Experimental setup MZI for determination of EO coefficients of a thin organic film. He–Ne–Helium–Neon laser 632.8 nm, $\lambda/2$—half wave plate, BS—beam splitter, M1, M2 and M3—mirrors, PS—phase shifter, Sample, PD—photodiode, Lock-in—Lock-in amplifier, Amp—amplifier, PC—computer.

In the first case, an ITO glass slide carrying the polymer film is covered with another bare ITO glass slide as shown in Fig. 2(a), after which both slides are squeezed together in the sample holder. On the micron scale the surface of the sample, especially at slide edges, is rather rough, causing the formation of an air gap between the surface of the polymer and second ITO electrode.

In the second case, a top electrode comprising an Al layer with thickness of ~25 nm is sputtered directly onto the polymer film as shown in Fig. 2(b). In this case the overall optical transmission coefficient of the sample is reduced, thereby lowering the contrast of the interference pattern. However the required voltages on the electrodes for material poling and EO modulation are also lowered.

The electrical connections to the ITO electrodes were made using silver paste. The in situ poling was performed at 100 °C for 30 minutes with an applied voltage of 80 V for sample 1 and 50 V for sample 2. The parameters of the sandwich type samples shown in Table 1 served as initial conditions for fitting measurements to the model. The corresponding electric field in the polymer was estimated to be 3.0 V/μm and 41.3 V/μm for samples 1 and 2, respectively.

The thickness and refractive index of the polymer film was determined by a prism coupler (*Metricon 2010*), the extinction coefficient by measuring the absorption coefficient (*Ocean Optics HR4000CG-UV-NIR*). The air gap thickness was evaluated by interference fringe separation in the low absorbance part of the sample transmittance spectrum.

The EO experiment was performed as follows. Modulation voltage (typically 50 V rms for sample 1 and 15 V rms for sample 2) at 4 kHz was applied to the electrodes. The output light intensity of MZI (DC signal) and the light modulation amplitude (AC signal) was detected with the Si photodiode and measured with the lock-in amplifier. Measurements were performed at several MZI interference phase points, at each of which data were collected for 20 s and then averaged. The measurement series was done with ***s*** and ***p*** polarized light at several incident angles. Fig. 3 shows typical measurement results where the interference phase is scanned in the reference arm of the MZI.

From Fig. 3 the maximal modulation depth is calculated by

$$m_{\max} = \frac{I_{ac\max} - I_{ac\min}}{(I_{\max} - I_{\min})}, \quad (1)$$

where $I_{ac\ max}$ and $I_{ac\ min}$ are the AC maximal and minimal modulated signal amplitudes, I_{max} and I_{min} are the maximal and minimal values of DC signal obtained from the MZI phase scan. Maximal modulation depth is a dimensionless number used to describe the relative AC modulation intensity.

2.1. The influence of EO effect on output of MZI

The EO coefficient tensor r_{ijk} characterizes the ability of a material to change its refractive index n when low frequency

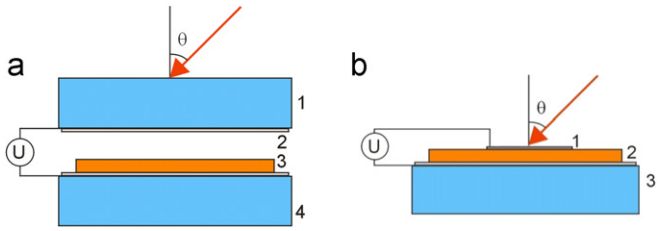

Fig. 2. Sample 1 geometry: 1, 4—ITO coated glasses, 2—air gap, 3—PMMA+DMABI 10 wt% polymer, θ—light incidence angle; Sample 2 geometry: 1—sputtered Al layer, 2—PMMA+DMABI 10 wt% polymer, 3—ITO coated glass, θ—light incidence angle.

Table 1
Parameters of sandwich type samples.

Layer	Thickness	Sample 1	
		Refractive index n (at 632.8 nm)	Extinction coefficient k (at 632.8 nm)
Glass	1 ± 0.02 mm	1.5	0
ITO	15–30 nm	1.76	0
Air gap	5.95 ± 2.38 μm	1.00	0
Polymer	0.90 ± 0.09 μm	1.54	$(10.4 \pm 0.01)10^{-3}$
ITO	15–30 nm	1.76	0
Glass	1 ± 0.02 mm	1.50	0
		Sample 2	
Layer	Thickness	Refractive index n (at 632.8 nm)	Extinction coefficient k (at 632.8 nm)
Al layer	25 ± 1 nm	1.45	7.54
Polymer	1.21 ± 0.09 μm	1.54	$(10.4 \pm 0.01)10^{-3}$
ITO	15–30 nm	1.76	0
Glass	1 ± 0.02 mm	1.50	0

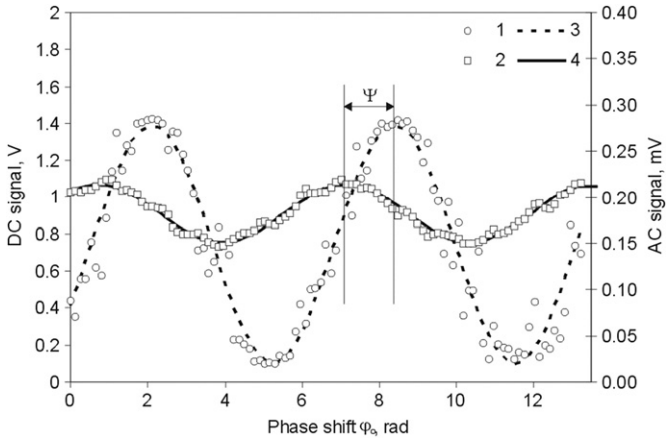

Fig. 3. Typical EO measurement performed at 8° incidence angle with s polarized light: 1—I_{DC} signal experimental data, 2—I_{AC} signal experimental data, 3—I_{DC} signal sine fit, 3—I_{AC} signal sine fit, Ψ—AC and DC signal maxima phase difference.

electric field E is applied

$$\left(\frac{1}{\Delta n^2}\right) = \sum_k r_{ijk} E_k \tag{2}$$

Due to Kleinman symmetry r_{ijk} can be rewritten in as r_{il} which is a 6×3 tensor. In a poled polymer with a point group symmetry of $C_{\infty v}$ the effective EO coefficient for ***s*** polarized light can be written [17]

$$r_{ef} = r_{13} \tag{3a}$$

and for ***p*** polarized light

$$r_{ef} = r_{13}\cos^2\alpha + r_{33}\sin^2\alpha, \tag{3b}$$

where r_{13} and r_{33} are the EO coefficients, and α is the angle between the externally applied electric field (normal to the plane of the EO active layer) and light propagation direction

$$\alpha = \sin^{-1}\left(\frac{1}{n_{EO}}\sin\theta\right), \tag{4}$$

where n_{EO} is the refractive index of EO layer and θ is the angle of incidence on the sample. It is convenient to use the ratio r_{33}/r_{13} to check the validity of the experimentally determined EO coefficient values. For polymer films poled at low electric fields this ratio should be in the range from 1 to 3 [18].

The light intensity at the MZI output can be described by the two beam interference equation

$$I_{o1} = \frac{1}{2}\left(I_r + I_s + 2\sqrt{I_r I_s}\cos(\varphi)\right) \tag{5}$$

where I_r is the light intensity in the reference arm, I_s is the light intensity in the sample arm, φ is the interference phase difference (adjustable by phase shifter). If the phase of one of the beams is AC modulated, and both intensities I_r and I_s are constant then we expect to see an AC signal proportional to a derivative of MZI output DC signal with respect to interference phase φ [3]. In other words the AC signal maxima should be ahead of the DC signal (light intensity) maxima of MZI output by phase difference $\Psi = const = \pi/2$. After performing numerous series of measurements we have found that the above mentioned phase difference is not constant but varies with incidence angle and from sample to sample. To explain these observations we conclude that the sample modulates not only the phase φ, but also the intensity of I_s.

If an AC electrical field is applied to a sample the transmission T and phase φ are also modulated and defined by many sample and acquisition parameters

$$T = T(N, pol, r_{ef}, \theta, d, V) \tag{6}$$

$$\varphi = \varphi(N, pol, r_{ef}, \theta, d, V), \tag{7}$$

where N is the complex refraction index, *pol*—polarization of light, r_{ef}—effective EO coefficient, d—thickness, V—modulation voltage and θ—light incidence angle on the sample.

Thus the detected output light intensity and therefore the AC signal amplitude is a function of these parameters. As the sample is a complex multilayer system its optical transmission and reflection characteristics may be calculated using the Abelès matrix formalism; however the values of parameters of (6) and (7) must be known. The thicknesses and complex refraction indices for each layer could be obtained from independent experiments. The aim is to determine the effective coefficient r_{ef} of the EO active polymer film from MZI experiments.

2.2. Abelès matrix formalism

To describe the intensity and phase of light transmitted through the sandwich sample at a certain applied voltage one can use Abelès matrix formalism. The characterization of a multilayer optical system begins by creating a characteristic matrix for the i-th layer

$$M_i = \begin{pmatrix} \cos\left(\frac{2\pi N_i d_i \cos\theta_i}{\lambda}\right) & \frac{j}{\gamma_i}\sin\left(\frac{2\pi N_i d_i \cos\theta_i}{\lambda}\right) \\ j\gamma_i \sin\left(\frac{2\pi N_i d_i \cos\theta_i}{\lambda}\right) & \cos\left(\frac{2\pi N_i d_i \cos\theta_i}{\lambda}\right) \end{pmatrix} \tag{8}$$

where $i=1$ is the first layer crossed by light and

$$\gamma_i = N_i \cos\theta_i (\text{s}-\text{polarisation}) \tag{9a}$$

$$\gamma_i = \frac{N_i}{\cos\theta_i}(\text{p}-\text{polarisation}) \tag{9b}$$

$$N_i = n_i - jk_i \tag{10}$$

and d_i is the thickness of the i-th layer, N_i—complex refractive index of i-th layer at wavelength λ, n_i—refractive index of i-th layer, k_i—extinction coefficient of i-th layer, θ_i—angle of light propagation in i-th layer. For describing the multilayer system one must calculate the characteristic matrix of the system

$$M = \prod_i M_i \tag{11}$$

If the elements of M are described by

$$M = \begin{bmatrix} m_{11} & m_{12} \\ m_{21} & m_{22} \end{bmatrix}, \tag{12}$$

then the transmission and reflection amplitudes are given by

$$t = \frac{2\gamma_{in}}{\gamma_{in}m_{11} + \gamma_{out}m_{22} + \gamma_{out}\gamma_{in}m_{12} + m_{21}}, \tag{13}$$

$$r = \frac{\gamma_{in}m_{11} - \gamma_{out}m_{22} + \gamma_{out}\gamma_{in}m_{12} - m_{21}}{\gamma_{in}m_{11} + \gamma_{out}m_{22} + \gamma_{out}\gamma_{in}m_{12} + m_{21}} \tag{14}$$

from where transmittance and reflectance are determined [19] as

$$T = \frac{\gamma_{out}}{\gamma_{in}}|t|^2 \tag{15}$$

$$R = |r|^2 \tag{16}$$

The phase difference caused by the sample is

$$\Delta\varphi = \arctan\left(\frac{\text{Im}r}{\text{Re}r}\right). \tag{17}$$

By modulating n_i in (10) and combining the sample transmittance (15), phase difference (17) with the equation describing the MZI output intensity (5) one can attempt to fit experimental AC signal data by adjusting n_i, the refractive index and d_i, the thickness of the polymer film as well as the thickness of the air gap in sample 1, from which the EO coefficients of the material under investigation may be deduced. We used the MatLab option "trust region reflective" as the data fit algorithm which is the default.

3. Results and discussions

For sample 1 according to our observations the maximal modulation depth m_{max} decreases as the incidence angle is increased. To describe the experimental data it was necessary to include sample thickness modulations in our model. Thickness changes may be caused by electrostriction or piezoelectric effects. To prove the existence of these effects and evaluate the magnitude of the sample polymer layer thickness modulation we used the MZI method in reflection configuration [10]. In this case mirror M1 of the MZI was replaced by a sample mirror consisting of an ITO glass slide covered by a spin coated thin film (~1 μm) of polymer (PMMA+DMABI 10 wt%). It was enclosed by a reflective Al layer 100 nm thick deposited on top of the polymer sample film with the Al layer facing the incident beam. Such a sample has the same configuration as sample 2; however the Al layer is thicker so that light will not penetrate into the polymer film causing multiple internal reflections. In this configuration, when voltage is applied to the electrodes, the electric field caused the sample thickness to change, thereby mechanically altering the optical path length in the sample arm of the MZI. To evaluate the actual thickness change of the sample we have to derive the modulation depth equation for the situation where phase modulation takes place only due to changes in sample arm physical path length. In this case the light intensity at the MZI output, or DC signal, a phase difference of $\Psi = \pi/2$ with respect to the AC modulated signal was observed as the phase in the reference arm was scanned (cf. Fig. 3), as expected.

For the maximal measured modulation depth of 7.10^{-5} on an unpoled sample, a sample thickness alteration of approximately 14 pm was deduced. In Fig. 4 the modulation depth, determined according to (1), is shown as a function of applied modulation voltage. The maximal modulation depth dependence on modulation voltage is seen to consist of two components: an electrostriction effect (quadratic) and piezoelectric effect (linear). Moreover, both of these effects increase when the polymer films are poled. As can be seen from Fig. 4 the electrostriction effect increases almost 5 times (the quadratic coefficient increases from $1.68\cdot10^{-5}$ to $7.95\cdot10^{-5}$), while the piezoelectric effect grows only 2 times (the linear coefficient increases from $2.51\cdot10^{-4}$ to $5.22\cdot10^{-4}$) after poling. From these coefficients it is possible to estimate the voltages at which the electrostriction effects will start to dominate over the piezoelectric contribution for the thickness change. For the unpoled film the electrostriction will start to dominate at around 15 V while for the poled film at 6.6 V.

In Fig. 5 the maximal modulation depth of sample 1 (see Table 1 and Fig. 2) at different light incidence angles is shown. The measurement was performed with the MZI in transmission configuration by applying 50 V rms to the ITO electrodes. The most important thing to notice in Fig. 5 is that the maximal modulation depth for ***s*** polarized light is higher than that for ***p*** polarized light. From Eqs. (3a and 3b)) the refractive index change and therefore the maximal modulation depth for ***p*** polarized light are expected to be higher because the effective EO coefficient r_{ef} is a combination of both r_{13} and r_{33}. Due to electrostriction and piezoelectric effects the sample thickness changes causing the modulation depth decrease for greater incidence angles. The fit is performed by allowing the preliminary experimental results of polymer film and air gap thicknesses to vary so that the polymer EO coefficients r_{13} and r_{33} and thickness alteration Δl due to electrostriction and piezoelectric effects can be deduced.

For sample 1 experimental data fitting we used glass–ITO–polymer–air gap–ITO–glass layer system (Fig. 2(a) and Table 1), which includes the interference effects caused by multiple reflections in the glass slides. If the glass slides are excluded from the fit model the noise like interference fringes in the fit lines disappear leaving smooth lines instead. However, in this case it would be

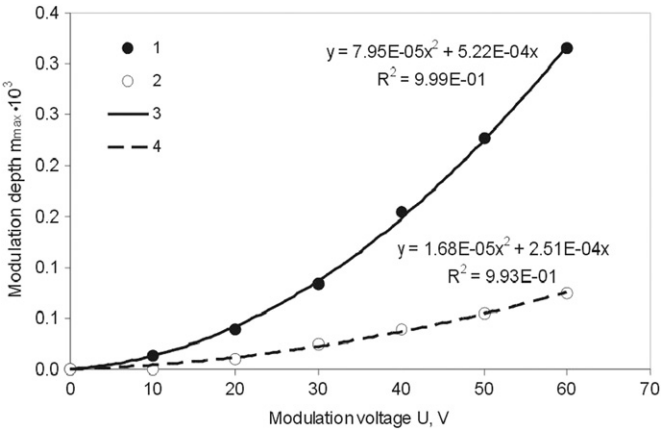

Fig. 4. Modulation depth m_{max} as a function of modulation voltage U for a MZI in reflection configuration. Quadratic function regression is applied. 1—modulation depth m_{max} of poled film, 2—modulation depth m_{max} of unpoled film, 3—quadratic fit of modulation depth m_{max} of poled film, 4—quadratic fit of modulation depth m_{max} of unpoled film.

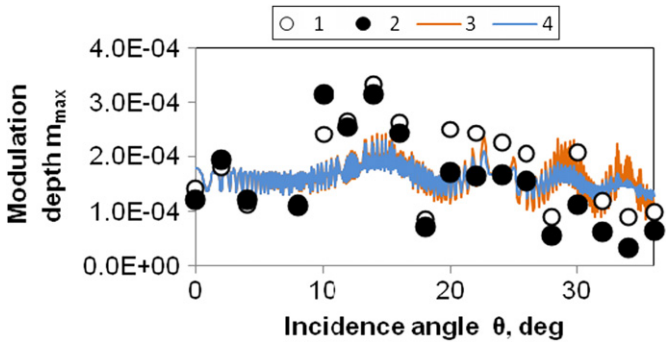

Fig. 5. Modulation depth dependence from incidence angle in MZI in transmission configuration for sample 1: 1, 2—experimental data for ***s*** and ***p*** polarized light, respectively; 3, 4—fit with MatLab based on Abelès matrix formalism for ***s*** and ***p*** polarized light, respectively.

Table 2
Sample 1 parameters deduced from numerical fit results.

Parameter	Value
Polymer film thickness l	0.85 ± 0.05 μm
Air gap l_{air}	5.90 ± 0.10 μm
Δl_{air}	170 ± 5 pm

hard to explain the dispersion of experimental data. From initial fits to sample 1 data it was evident that the modulation depth is a linear combination of both the sample layer thickness and refractive index modulations. Taking both into account yields EO coefficients with r_{33}/r_{13} ratio value ~10, giving r_{33} a value of approximately 100 pm/V, which is considerably higher than published values [18]. For confirmation, Maker fringes were captured determining a NLO coefficient ratio of $d_{33}/d_{13}=1.86$ which should be the same as that for r_{33}/r_{13}. We also tried to fit the experimental data by permitting only polymer layer thickness modulations. The amplitude of these thickness modulations were a lot higher than expected if one considers the experimental results done earlier (Fig. 4). Therefore the final fit was performed with only the air gap Δl_{air} as fitting variable assuming that the glass slide separation is modulated by the attractive force of the electrostatic field. Further experiments showed modulation depth dependence on the modulation frequency and even modulation depth increase at frequencies below 1 kHz. This can be explained only by some mechanical oscillations in the system where increase is caused by mechanical oscillation resonance. Only a reasonable agreement with experimental data could be achieved if air gap modulations were allowed. The experimental data and best fit are shown in Fig. 5. The fit values are shown in Table 2, from which the polymer film thickness and air gap thickness are seen to be in good agreement with the preliminary experimental results. Also from Fig. 5 one can notice that the model describes the overall tendency of modulation depth versus the incidence angle quite well, however with some outliers. This could be caused by the sample illumination point, being slightly offset from the rotation axis of the sample, thereby causing movement over local variations of the surface.

To determine the EO coefficients of sample 1 more accurately, the air gap thickness modulation effects which have the dominating contribution to the overall modulation depth values would need to be reduced. This could be achieved with very high modulation frequencies, several tens of kHz, however in our case the measurements were limited by the 20 kHz cutoff frequency of the photodetector.

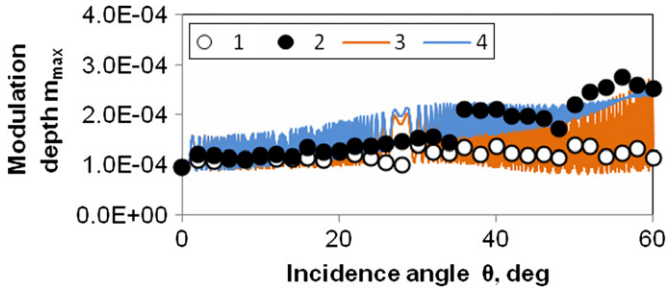

Fig. 6. Modulation depth dependence on incidence angle in MZI in transmission configuration for sample 2: 1, 2—experimental data for ***s*** and ***p*** polarization, respectively; 3, 4—MatLab fit to functions based on Abelès matrix formalism for ***s*** and ***p*** polarization, respectively.

Table 3
Calculated sample 2 parameters from numerical fit results.

Parameter	Value
Thickness l_1	1.34 ± 0.05 μm
r_{13}	0.19 ± 0.02 pm/V
r_{33}	0.55 ± 0.06 pm/V

The modulation depth dependence on incidence angle for sample 2 can be seen in Fig. 6, which includes a fit to the glass–ITO–polymer–Al layer structure model. Modulation depth measurements showed a linear dependence on the applied voltage. As shown before, the thickness changes are quadratically dependent on the applied voltage. Since the theory predicts a linear dependence of modulation depth amplitude on the applied electric field, one can assume that thickness modulations have small influence on the overall modulation depth for sample 2. Therefore in fitting to the model only refractive index changes in the polymer layer were allowed, arriving at the values shown in Table 3.

As mentioned earlier, Ψ is a function of light incidence angle on the sample and for simple sample configuration one can also have a good fit for the phase difference Ψ changes. However, in the case when relatively thick (~1 mm) glass slides are used the Ψ value oscillates strongly with variations in incidence angle and layer thickness, having noise like character which complicates the fitting procedure.

4. Conclusions

We have demonstrated that both EO coefficients (r_{13} and r_{33}) of poled polymer films can be determined by applying Abelès matrix formalism to the interpretation of experimental MZI data of a sandwich sample structure at different incidence angles. Using a simple MZI reflection technique we have shown that for PMMA+DMABI 10 wt% polymer films, thickness changes due to an applied electric field influence on the detected modulation depth and therefore must be taken into account. Moreover, if an air gap is formed in the sample, the modulated signal in the MZI is usually dominated by the air gap thickness modulation. Experimental data fits show that thickness modulations of an air gap result in beam intensity modulations which are at least one order larger in amplitude than those of the polymer layer. In this case, the thickness modulations of the air gap also override the EO modulations of polymer layer, so that the EO coefficients for such a system cannot be reliably determined. For a sample structure that has no air gap the modulated signal in the MZI is mainly caused by EO modulations. The proposed experimental procedure and data treatment for determining the EO coefficients resulted in

values of $r_{13}=0.19\pm0.02$ pm/V and $r_{33}=0.55\pm0.06$ pm/V for a poled PMMA+DMABI 10 wt% polymer film.

Acknowledgments

This research was granted by ERDF 2.1.1.1 activity Project no. 2010/0308/2DP/2.1.1.1.0/10/APIA/VIAA/051 "Development of polymer EO modulator prototype device" and Latvian National Research "Development of novel multifunctional materials, signal processing and information technologies for competitive knowledge-based products".

References

[1] L.R. Dalton, Journal of Physics: Condensed Matter 15 (2003) 897.
[2] A. Knoesen, M.E. Molau, D.R. Yankelevich, M.A. Mortazavi, A. Dienes, International Journal of Nonlinear Optical Physics 1 (1) (1992) 73.
[3] M. Aillerie, N. Theofanous, Applied Physics B, Lasers and Optics 70 (2000) 317.
[4] C.C. Teng, H.T. Man, Applied Physics Letters 56 (18) (1990) 1735.
[5] C. Maertens, C. Detrembleur, Chemistry of Materials 10 (1998) 1010.
[6] W.H.G. Horsthuis, G.J.M. Krijnen, Applied Physics Letters 55 (7) (1989) 616.
[7] M. Sigelle, R. Hierle, Journal of Applied Physics 52 (6) (1981) 4199.
[8] M.J. Shin, H.R. Cho, Journal of the Korean Physical Society 31 (1) (1997) 99.
[9] R. Meyrueix, O. Lemonnier, Journal of Physics D: Applied Physics 27 (1994) 379.
[10] C. Greenlee, A. Guilmo, A., Opadeyi, R. Himmelhuber, R.A. Norwood, M. Fallahi, J. Luo, S. Huang, X.H. Zhou, A.K.Y. Jen, N. Peyghambarian, Mach–Zehnder interferometry method for decoupling electro-optic and piezoelectric tensor components in poled polymer films, Proceedings of the SPIE, vol. 7774, p. 77740D-2.
[11] A.S. Andrushchak, B.G. Mytsyk, N.M. Demyanyshyn, M.V. Kaidan, O.V. Yurkevych, I.M. Solskii, A.V. Kityk, W. Schranz, Optics and Lasers in Engineering 47 (1) (2009) 31.
[12] A.S. Andrushchak, B.G. Mytsyk, N.M. Demyanyshyn, M.V. Kaidan, O.V. Yurkevych, I.M. Solskii, A.V. Kityk, W. Schranz, Optics and Lasers in Engineering 47 (1) (2009) 24.
[13] Etienne Patrice Nagtegaele, Joseph Brasselet, Journal of the Optical Society of America B 20 (9) (2003) 1932.
[14] F. Abelès, J. Phys. Radium (1950) 310.
[15] F. Qiu, X. Cheng, K. Misawa, T. Kobayashi, Chemical Physics Letters 266 (1997) 153–160.
[16] M. Rutkis, A..Vembris, V..Zauls, A..Tokmakovs, E..Fonavs, A..Jurgis, V..Kampars Proceedings of the SPIE, Organic Optoelectronics and Photonics II, vol. 6192, p. 61922Q, 2006.
[17] R.A. Norwood, M.G. Kuzyk, R.A. Keosian, Journal of Applied Physics 75 (4) (1994) 1869.
[18] P. Rondou, M.V. Beylen, C. Samyn, A. G. S'heeren, Makromolecular Materials and Engineering 193 (12) (1992) 3045.
[19] S. Larouche, L. Martinu, Applied Optics 47 (13) (2008) C219.

THE JOURNAL OF PHYSICAL CHEMISTRY B

Article

pubs.acs.org/JPCB

Poling Induced Mass Transport in Thin Polymer Films

Edgars Nitiss,[†] Eduards Titavs,[†] Karlis Kundzins,[†] Andrej Dementjev,[‡] Vidmantas Gulbinas,[‡] and Martins Rutkis*[,†]

[†]Institute of Solid State Physics, University of Latvia, Kengaraga street 8, Riga, Latvia

[‡]Lithuanian Center of for Physical Sciences and Technology, A. Gostauto street 11, Vilnius, Lithuania

ABSTRACT: In this study we report investigation of the polymer film morphology modifications during their corona poling for fabrication of nonlinear optically (NLO) active materials. We demonstrate that at certain poling conditions surface and spatial inhomogeneities in the poled area of the sample appear. Densities of the inhomogeinities depend on the strength of the poling field, the sample temperature during the poling, and the prepoling conditions. Optimization of the poling conditions directed toward avoiding surface modifications enables us to increase the overall observable effective nonlinearity of the sample up to 10 times. To investigate, understand, and eventually explain the formation of the spatial and surface structure inhomogeinites in the poled material we have used optical, second harmonic, and scanning electron microscope measurements, as well as the conductivity measurements of the thin films. We present results of poled polymer host−guest films where (dimethylamino)benzylidene-1,3-indandione and low dipole moment 2,2′,2″-(4,4′,4″-nitrilotribenzylidene)triindan-1,3-dione were used as guests in poly(methyl methacrylate), polystyrol, and polysulfone matrixes doped at 10 wt %.

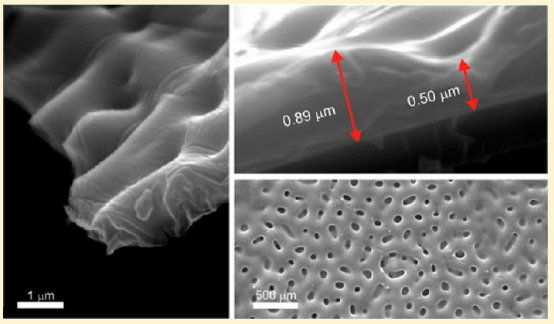

INTRODUCTION

Nonlinear optically (NLO) active polymers doped with polar molecules are promising substitutes of NLO active inorganic materials for modern electronics. An increasing interest to new nonlinear optical (NLO) active organic materials is related to their low cost, easy processability, and potential applications as optical components in electro-optic (EO) modulators, optical switches, sensors, etc.[1,2] Such materials must possess large second-order nonlinear coefficients, which can be obtained by electric poling with corona discharge.[3−9] For maximal possible NLO efficiency one must achieve the highest polar order of dopant molecules in the system maintaining the chromophore structure, concentration, and optical properties of thin films. For polymer poling purposes the corona triode device is very attractive because one can have good control of the ion source and the poling field. The poling efficiency depends on multiple parameters such as poling temperature, electric field, etc. The corona poling possesses also several drawbacks. It takes a lot of effort for one to obtain controllable corona discharge and poling conditions due to the complexity of the discharge process. It has also been reported that poling with corona discharge may influence the surface quality of the film which is usually attributed to the bombardment of the film by accelerated ions.[10−12]

The second-order nonlinearity of poled material can be characterized using the second-order polarizability $\chi_{zzz}^{(2)}$

$$\chi_{zzz}^{(2)} = C\beta_{\mu}\langle\cos^3\vartheta\rangle \tag{1}$$

where C is the chromophore concentration, β_{μ} is the molecular second-order polarizability projection on the dipole moment of molecule, and $\langle\cos^3\vartheta\rangle$ is the order parameter or the averaged cosine cube of angular difference between the dipole moment of the molecule and poling field.[13] The order parameter, according to an analytic approximation,[14] can be expressed as

$$\langle\cos^3\vartheta\rangle = \frac{\mu E}{5kT}\left[1 - L^2\left(\frac{W_{es}}{kT}\right)\right] \tag{2}$$

where E is the poling field, T is the poling temperature, k is the Boltzmann constant, μ is the dipole moment of the molecule, L is the Langevin function, and W_{es} is the chromophore−chromophore electrostatic energy. The relation 2 may be divided into two parts. The first part, $\mu E/5kT$ describes the order parameter as a function of poling (μE) and the thermal depolarization (kT). As can be seen from (2), it is desirable to have the poling (μE) energy as high as possible for maximal ordering. This obviously can be achieved by increasing the poling field E strength. However, surface irregularities may appear, as shown previously.[10−12] As a result, optical quality of the film is reduced and light scattering takes place. The second part of (2) ($1 - L^2(W_{es}/kT)$) expresses the dipole−dipole interactions in the material, which tend to reduce the order parameter due to repulsion of dipoles oriented in same direction. The dipole−dipole interactions could be also

Received: November 6, 2012
Revised: January 24, 2013
Published: February 12, 2013

responsible for the reduction of the NLO efficiency by stimulating formation of centrosymmetric NLO inactive aggregates, especially in guest–host systems where chromophores can move within a matrix.

In this contribution we present investigation of the spatial and surface irregularities in the guest–host polymer films poled at high field strength by the corona triode device. We have used a computer controlled corona triode device, which allows us to capture current–voltage characteristics of the system as well as to perform NLO polymer poling at constant grid potential or sample current. We show that similar changes in thin film morphology appear for all used host materials.

EXPERIMENTAL SECTION

The investigated polymer host–guest films were prepared as follows. We used (dimethylamino)benzylidene-1,3-indandione (DMABI[15]) and low dipole moment 2,2′,2″-(4,4′,4″-nitrilotribenzylidene)triindan-1,3-dione (A3BI[16]) chromophores as guests in various matrixes (poly(methyl methacrylate) (PMMA, Sigma-Aldrich), polystyrene (PS, Sigma-Aldrich), and polysulfone (PSU, Sigma-Aldrich)) doped at 10 wt %. The films were spin-coated from a chloroform solution onto an ITO covered glass slide (SPI Supplies, ITO sheet resistivity 70–100 Ω). The glass transition temperatures of the samples were approximately 110 °C for the PMMA, 63 °C for the PS, and 119 °C for the PSU thin films. The thickness of the spin-coated samples was around 2 μm.

For sample poling we used a computer controlled corona triode device, which allows us to monitor and control the poling conditions. The principal scheme of corona triode setup[17] is shown in Figure 1. During the corona poling, high

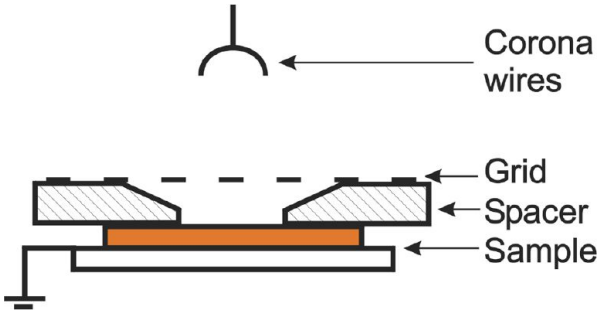

Figure 1. Principal scheme of corona discharge device.

voltage is applied to corona wires. By varying the grid voltage, we are able to control the polymer poling voltage. The voltage difference between corona wires and grid was kept constant of 9 kV to ensure invariable corona discharge conditions at different grid voltages. Ambient air in the corona chamber was replaced by nitrogen to keep the corona generated ionic composition and conductivity independent of temperature and moisture. The sample was put on the heater with precisely controlled temperature. We have also used spacers for varying the grid to sample distance. The spacer hollow has a conical shape; therefore, it acts as a lens for the ion flux allowing one to reduce the sample charging time at the beginning of the poling.

The resulting NLO efficiency and optical quality of the polymer films were found to depend on the poling procedure. One of the most common poling procedures includes turning on corona voltage after heating of the polymer to the glass transition temperature.[18,19] This procedure has an advantage of having polymer disposed of solvent and absorbed gases such as air and water vapor before chromophore orientation. However, at high guest concentrations many of chromophores tend to form aggregates and even crystals, which significantly reduce the NLO efficiency and the film quality. Turning on external electric field during the heating of the polymer film can prevent crystallization.[20] We used two poling procedures, which are schematically shown in Figure 2a,b. During the first poling

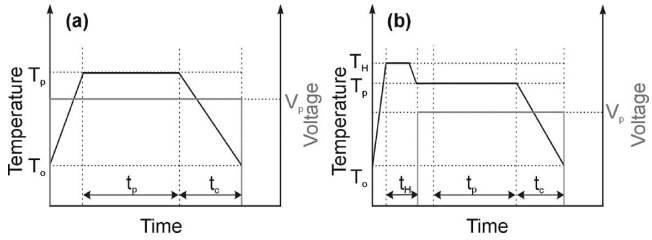

Figure 2. Time scale and parameters of (a) first corona poling procedure and (b) second poling procedure. T_o, T_p, and T_H are the room, poling, and heating temperatures, respectively, V_p is the poling/grid voltage, and t_h, t_p, and t_c are the heating, poling, and cooling times, respectively.

procedure, as suggested by Vembris et al.,[20] the poling voltage was applied and kept constant while the sample was heated up to poling temperature T_p, poled and then cooled down to ambient temperature T_o. Such an approach reduced the amount of aggregates and crystals formed during the poling. However, we noticed that this poling procedure significantly increased probability of formation of spatial and surface inhomogeneities in the poled area of the sample. Therefore, we implemented the second poling procedure suggested by Lee et al.,[12] which allowed us to maintain good optical quality of poled thin films. It starts with a prepoling phase t_H of approximately 3–5 min, during which the sample is heated to the preheating temperature T_H with no poling field applied. The performed experiments show that this period of time is short enough to avoid formation of centrosymmetric crystals, but sufficiently long to dispose major part of the solvent and absorbed gases for the thin film. Afterward, the sample is poled like in the first poling procedure.

We used second harmonic generation (SHG) measurements with a setup[15] to evaluate the NLO efficiency of the poled polymers. From the SHG scan we are able to obtain the NLO efficiency profiles of the poled polymer. The SH intensity was then normalized to the SH intensity generated in quartz crystal. The obtained value is the effective nonlinear optical (NLO) coefficient d_{eff}.

Optical (bright field) microscope (Nikon ECLIPSE L150), scanning electron microscope (SEM) (Carl Zeiss EVO 50 XVP), and two photon excitation luminescence (TPEL) and SHG microscopes were used for investigation of irregularities in the poled polymer films.

Both TPEL and SHG images of poled polymer films were obtained through raster scanning of samples using a nonlinear optical scanning microscope. Excitation with picosecond pulses at 1064 nm wavelength and 1 MHz repetition rate was applied. An integral TPEL signal in a range from 540 to 710 nm was collected by using two cutoff filters (Thorlabs, Asahi-Spectra). The SHG signal was filtered with a laser line filter at 532 nm with the fwhm of 10 ± 2 nm (Thorlabs). The SHG imaging was performed at two perpendicular polarizations.

dx.doi.org/10.1021/jp310961a | J. Phys. Chem. B 2013, 117, 2812–2819

RESULTS

Sample corona poling by the first procedure at certain poling conditions caused appearance of optical inhomogeneities in the poled part of the film. The optical inhomogeinities were caused by surface and/or spatial irregularities. As the size of inhomogeneities is close to the optical wavelength, light scattering takes place, and the poled area looks frosted. Optical microscope images of the unpoled region of PMMA+DMABI 10 wt % thin films and poled by the first poling procedure are shown in Figure 3a,b.

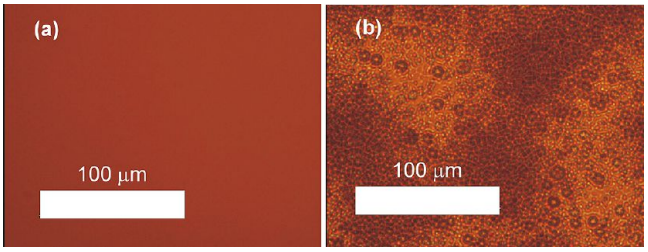

Figure 3. Optical images of the unpoled (a) and poled (b) regions of PMMA+DMABI (10 wt %) thin film obtained by the first poling procedure.

As mentioned before, higher NLO efficiencies should be obtained by increasing the poling field strength. However, as the poling field strength increases, the overall observable NLO efficiency drops down. This can be seen in Figure 4 where the

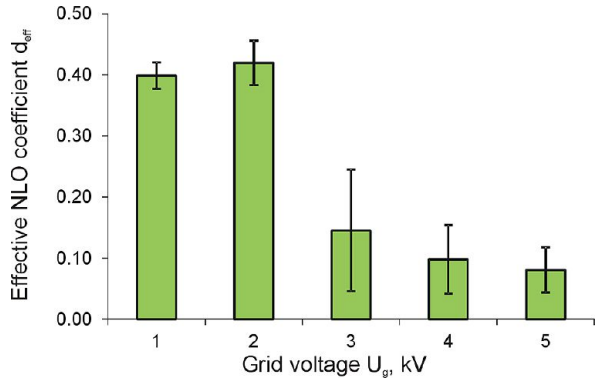

Figure 4. Effective NLO coefficient d_{eff} of PMMA+DMABI (10 wt %) thin films as a function of grid voltage for the samples poled by the first poling procedure.

effective NLO coefficient d_{eff} as a function of the grid voltage is shown. Clearly modification of the morphology of the poled area plays a significant role for the overall observable NLO efficiency. According to our observations, the inhomogeinities appear for all of the used hosts (PMMA, PS, and PSU). In Figure 5 optical images of poled areas of PMMA+DMABI (10 wt %), PS+DMABI (10 wt %), and (c) PSU+DMABI (10 wt %) thin films are shown.

The extent of the inhomogeneity was characterized by measuring the scattered light intensity. We found that the scattered light intensity depends on the poling electric field strength and the poling temperature, or simply on the ratio of poling and thermal energies. Figure 6 shows the scattered light

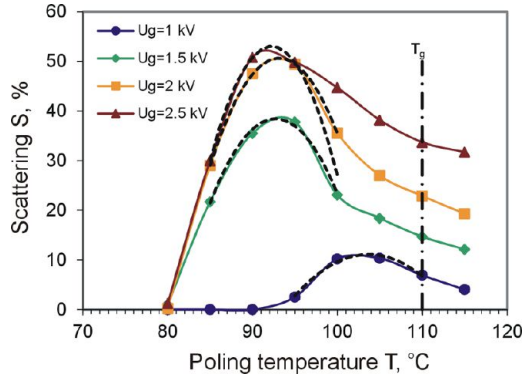

Figure 6. Scattered light percentage as a function of poling temperature at different grid voltages for PMMA+DMABI (10 wt %) thin films.

intensity as a function of poling temperature at different grid voltages. The light scattering from the poled part of the sample appears above the poling temperature of 80 °C. The scattered light intensity reaches maximum for sample poled at about 90 °C and then decreases as the poling temperature increases. The decrease is most probably caused by the reduction of amount of scattering elements due to decrease in viscosity, which favors the film fluidity and thus, reduction of film damage or some kind of "self-curing" takes place. The maximum of the scattered light intensity appears when higher grid voltages are applied at lower poling temperatures.

Figure 7 shows the poling temperatures at which the maximal scattered light intensity was obtained as a function of poling voltages. These values were obtained from the data displayed in Figure 6, where the points around the maximal scattering value are approximated by a second-order polynomial function. After the temperatures at which maximal light scattering takes place are identified, they are displayed as black points in Figure 7. The black point approximation suggests that the product of poling temperature at which maximum scattering is obtained

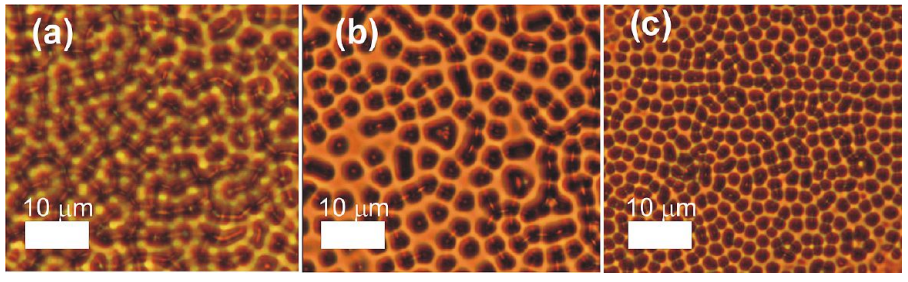

Figure 5. Optical images of the poled regions (a) PMMA+DMABI (10 wt %), (b) PS+DMABI (10 wt %), and (c) PSU+DMABI (10 wt %) poled applying first poling procedure.

dx.doi.org/10.1021/jp310961a | J. Phys. Chem. B 2013, 117, 2812−2819

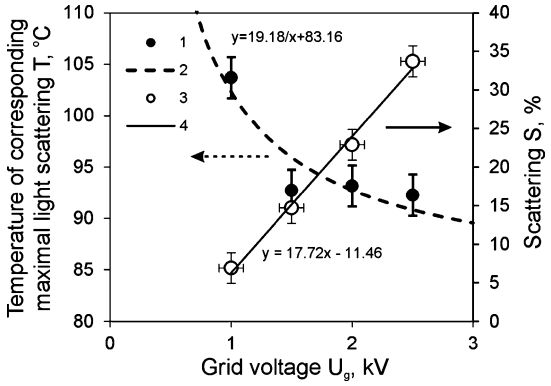

Figure 7. Temperature of corresponding maximal scattering as a function of poling temperature (1) and fit (2), scattering as a function of grid voltage for samples poled at T_g = 110 °C (3), and linear fit (4) for PMMA+DMABI (10 wt %) thin films.

and the respective grid voltage at which poling is performed is constant or simply $T{\cdot}E$ = const. The temperature and grid voltage relation clearly attributes to the amount of energy necessary for the formation of scattering structure in the PMMA+DMABI (10 wt %) thin films. Figure 7 also shows the scattering intensity as a function of grid voltage for the samples poled at glass transition temperature T_g = 110 °C. The scattering intensity in this case is directly proportional to the grid voltage value. Extrapolation of the linear dependence of scattering intensity to zero value gives that approximately 650 V is necessary for the surface irregularities to appear if the guest–host film is poled at glass transition temperature T_g.

Formation of the scattering structure depends also on the distance between the sample and the grid. Increase of the grid to sample distance reduces the ion energy and also weakens formation of the scattering structure. Figure 8 shows that the scattering intensity approximately linearly decreases with increase in the grid to sample distance.

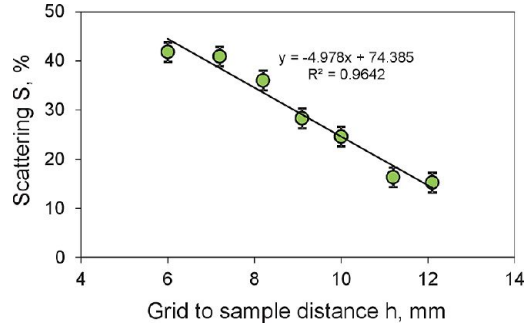

Figure 8. Scattered light percentage as a function of grid to sample distance for sample poled by the first poling procedure at constant grid voltage U_g = 1.5 kV and poling temperature 95 °C.

Figure 9 shows the SEM image of the poled PMMA+DMABI (10 wt %) film. It reveals the "hilly" structure of the film surface, with the typical "hill" to "hollow" height differences of about 0.4 μm, i.e., close to the half of the film thickness. Parts a–d of Figure 10 show optical, SHG, and two photon excitation luminescence (TPEL) images of the poled sample area. As a first approximation, we assume that locally the TPEL signal is proportional to the concentration of chromophores, but the SH intensity characterizes the amount of noncentrosymmetric elements. Parts a–d of Figure 10 show that dark spots in optical images are also dark in the TPEL images, again suggesting that the dark spots are hollows meaning that the mass is dragged away from the center of the hollow during the poling. It shall be also noticed that there is an increased TPEL and SH signal around the hollows.

From the analysis of the SH images, we see that only the hollow slopes are NLO active as is shown in Figure 11a,b at orthogonal excitation light polarizations. Such pattern in SHG image is typical for radial arrangement of the nonlinear dipoles. Because the SH intensity characterizes the amount of noncentrosymmetric elements, the pattern in SHG image suggests that the chromophores (dipoles) are oriented toward or away from the hollow centers.

The thin films maintain their optical quality if they are poled by the second poling procedure described above. When we compare NLO efficiencies at the centers of the samples poled at the same temperature and grid voltage, we find the samples poled by the second poling procedure show at least 6 times higher efficiency compared to the ones poled by first poling procedure. The effective NLO coefficients d_{eff} are shown in Figure 12. One would expect higher NLO activity from material poled by the first poling procedure than from material poled by the second procedure, due to the fact that fewer molecules are expected to form aggregates and crystals during the heating phase.[9] However, as the light scattering in the poled area takes place, the overall observable effective NLO activity of material is reduced. We also measured the NLO efficiency of the poled thin films as a function of grid voltage. From the experimental data shown in Figure 4 it can be seen that for the sample poled by the first poling the NLO efficiency decreases by increasing the grid voltage, on the contrary the NLO efficiency increases with the grid voltage as shown in Figure 13a if the second poling procedure was applied.

Because the effective NLO coefficient of the poled thin film depends on the electric field, we investigated also how the effective poling voltage depends on the grid to sample distance. In Figure 13b the effective NLO coefficient d_{eff} as a function of grid to sample distance for the films poled by second poling procedure at grid voltage 1.5 kV is shown indicating no clear dependence. This means that the sample was charged to a certain voltage (not higher than the grid voltage) regardless of the sample to grid distance.

We have analyzed surfaces of the PMMA+DMABI (10 wt %) samples how they depend on the prepoling and poling temperatures (Figure 14). For the characterization of the sample surfaces we used two possible states. Filled circles in Figure 14 mark the samples, which have changed their surface morphology, and empty circles represent the samples that have maintained their optical properties after the poling. All the samples were poled using the second poling procedure at 2.5 kV grid voltage. The dotted lines mark the glass transition temperature. On the basis of these results, we were able to determine the boundary at which in case second poling procedure is used the samples change their surface morphology. This boundary is indicated as a line dividing gray and white regions in the graph (Figure 14). If the prepoling and poling temperature values are chosen with coordinates (T_{pp}, T_p) that correspond to a point in the gray (white) region in Figure 14, the surface inhomogeinities will (will not) appear during the poling. It should also be noted that if samples are poled above glass transition temperature, there will always be changes in the sample surface morphology. To get the highest possible nonlinearity of the thin film, one should pole the samples

dx.doi.org/10.1021/jp310961a | J. Phys. Chem. B 2013, 117, 2812–2819

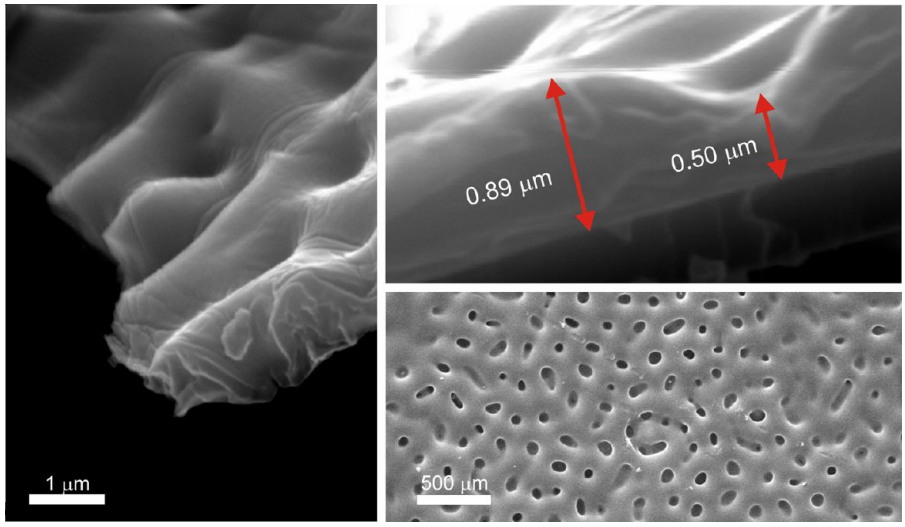

Figure 9. Electron microscope image of poled part of PMMA+DMABI (10 wt %) thin film.

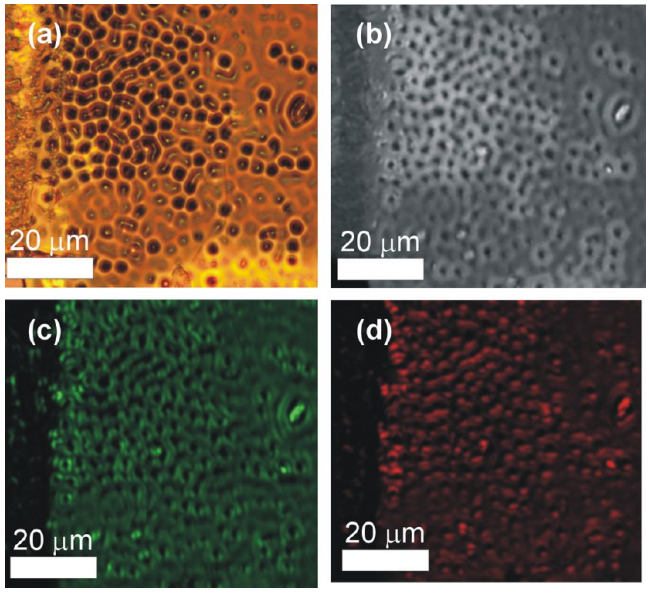

Figure 10. (a) Optical image, (b)TPEL, (c) SHG horizontally polarized (0°) and (d) SHG vertically polarized (90°) images of poled area of PMMA+DMABI (10 wt %) thin film.

using second poling procedure with prepoling and poling temperatures corresponding to a point that is as close as possible to the intersection of the glass transition temperature lines, but below the gray–white region boundary line. In this particular case for PMMA+DMABI (10 wt %) sample the poling temperature should be 105 °C and the prepoling temperature 115 °C.

Because the conductivity of the thin film could also influence the formation of surface irregularities, we investigated whether there are differences in the conductivity of the nonpreheated and preheated samples. For these measurements a 100 nm thick Al electrode was sputtered on the thin films and $I-V$ characteristics were captured. The results are shown in Figure 15. It can be clearly seen that the current at respective voltages is lower for the preheated samples.

DISCUSSION

As shown above, formation of the film inhomogenieties depend on the poling and prepoling procedures. There could be three main reasons for the formation of inhomogenieties in the guest host films during the poling. First, we suggest that the hollows are formed by the charged ions, which ram the soft polymer. The speed and therefore kinetic energy of ions depend on the grid potential and on the grid to sample distance. A second hypothesis would be that the hollows are formed due to mass transport induced by the poling field and chromophore dipole interaction. Numerical Langevin dynamics calculations imply that molecules, if not bound, due to dipole–dipole interactions can move, forming high-order structures during the poling procedure,[21] or in other words, mass transport can take place. In such a way chromophores, while creating polar elements, could drag the surrounding polymer. Finally, we would like to propose that the hollows could be made by local electrical breakdown of the polymer.

In the first two cases, polymer must be sufficiently soft for the changes in the morphology of the film to take place. Therefore, polymers must be poled at temperature higher than some critical value (Figure 6) for the inhomogeinities to appear. Unfortunately, both the formation of hollows due to high energy ion bombardment and the dipole moment–electric field interaction induced mass transport depend on the polymer poling temperature and poling field. This fact causes the difficulties to favor either of these two hypotheses on formation of surface inhomogeinities.

There are facts that would favor either the first or the second hypothesis of the formation of surface inhomogeinities. From Figure 8 it is obvious that the density of scattering elements grows if the grid is closer to the sample. This clearly favors the hypothesis that the hollows are formed during the ion impact. Increasing the grid to sample distance (assuming that the free path length does not change) we increase the probability for the charged ion to lose part of its kinetic energy during impacts in the space between grid and sample. Therefore, at the same initial potential energy conditions determined by the grid voltage, at higher sample to grid distances, the ions will have less kinetic energy left to transfer to the polymer film. Because the thin film poling voltages do not depend on the sample to grid distance (Figure 13b), the magnitude of poling field and

dx.doi.org/10.1021/jp310961a | J. Phys. Chem. B 2013, 117, 2812–2819

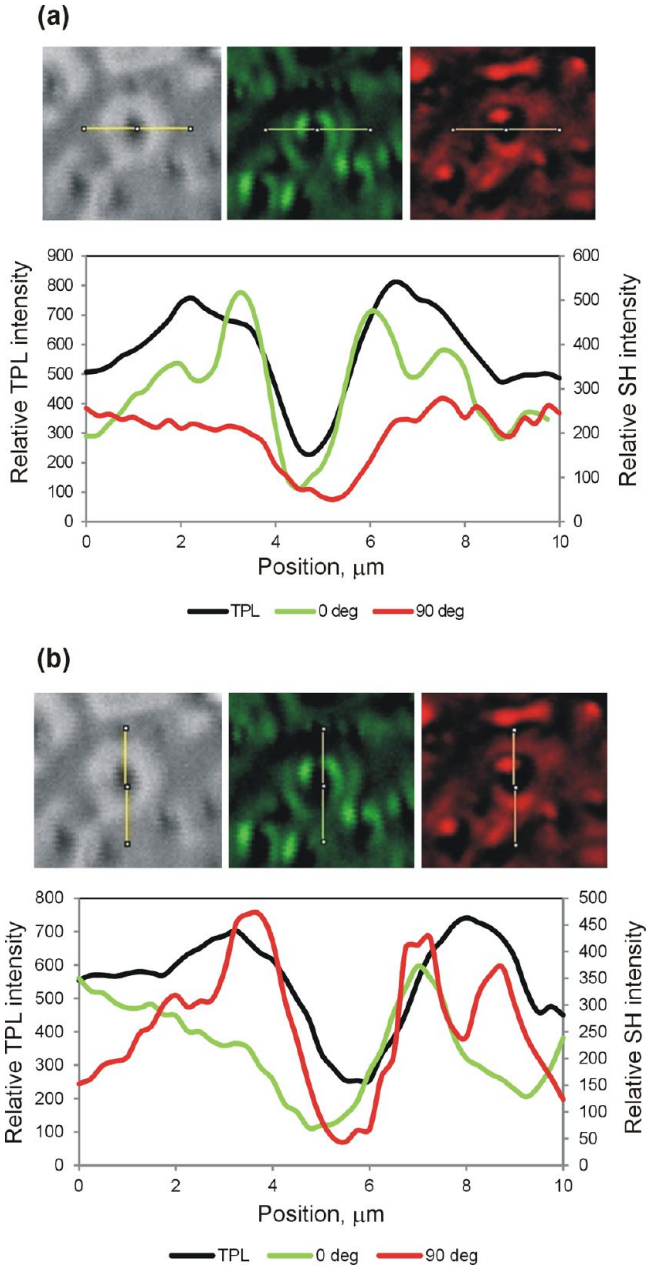

Figure 11. Caption TPEL and SHG intensities of the hollows scanned (a) vertically and (b) horizontally after excited by horizontally polarized (0°) and vertically polarized (90°) light.

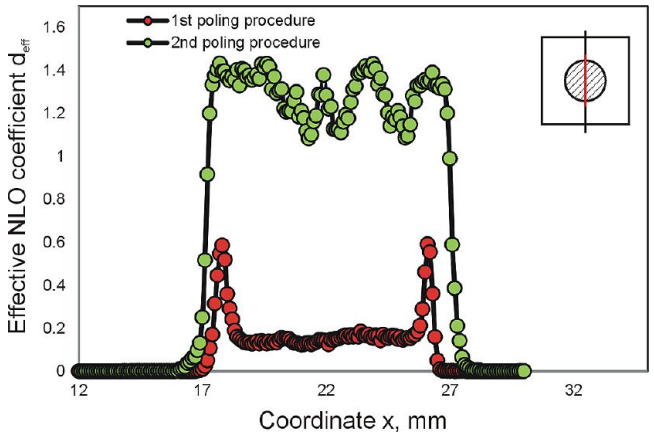

Figure 12. SHG scan: effective NLO coefficient d_{eff} of PMMA +DMABI (10 wt %) thin films poled of using first and second procedure.

molecule dipole moment interaction also would not change. This again favors the fact that hollows are formed during the ion impact. As mentioned previously, to eliminate the chromophore and electric field interaction effect on the formation of hollows, samples with nonpolar A3BI chromophores were made and poled. We were not able to observe any changes in the sample morphology. This clearly suggests that the chromophores in guest–host films must possess a dipole moment so that the changes in thin film morphology would take place. The result favors the second hypothesis that the hollows are formed due to mass transport induced by the poling field and chromophore dipole moment interaction. The probability of hollow formation due to mechanical impact and poling field and chromophore dipole moment interaction is also influenced by the poling temperature, which defines the viscosity of the polymer. Partial reduction of inhomogeinities at higher poling temperatures suggests that polymer is sufficiently soft (fluent) for the hollows to close.

The reason why there are no inhomogeinities in the sample to which prepoling procedure is applied could be the following. After sample preparation, the films still contain some amount of solvent, so the ambient gases and water accumulate in polymer pores. Heating the sample causes the solvent and absorbed gases to leave the pores, thus increasing the polymer glass transition temperature.[22]

Therefore, after the preheating of the film, the glass transition temperature of polymer increases making the mass transfer less probable. We also performed hardness measurements for the thin PMMA+DMABI (10 wt %) films, which showed that the hardness of the thin film to which prepoling procedure was applied increased only by 18%. Such a small increase in hardness could not be the reason for such a dramatic change in the surface irregularity concentration. Because after the spin coating the molecules are frozen not in the energetically most favorable condition from the molecular interaction point of view, we suppose that the prepoling procedure enhances the relaxation processes in the film. Thus, after the prepoling procedure, the molecules have compacted, therefore reducing the probability of poling induced mass transport.

Finally, we found that conductivity of the preheated samples is lower than for the samples poled by the first poling procedure (Figure 15). This finding leads to our third hypothesis for the formation of surface irregularities. We propose that the hollows could be made by local electrical breakdown of the polymer. Because the samples poled by the first poling procedure have higher conductivities than the ones poled by the second poling procedure, it is more likely that local electrical breakdown will take place during the first poling procedure. At temperatures beyond glass transition temperature T_g, the solvent and absorbed gases have left the sample. This means that at temperature beyond the T_g the conductivity would not depend on the prepoling procedure used. Because the conductivity of the polymer grows rapidly around T_g, the probability of electrical breakdown is a lot higher for samples poled at temperatures higher than T_g. This explains why the irregularities appear for both poling procedures at high enough poling temperatures.

dx.doi.org/10.1021/jp310961a | J. Phys. Chem. B 2013, 117, 2812–2819

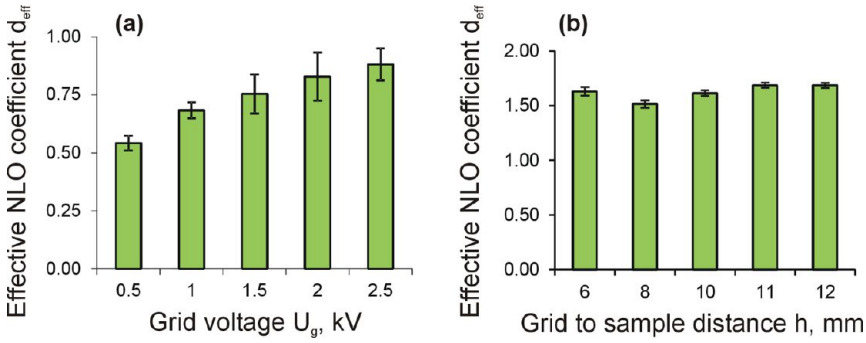

Figure 13. Caption effective NLO coefficient d_{eff} of PMMA+DMABI (10 wt %) thin films as a function of (a) grid voltage for the samples poled by the second poling procedure and (b) sample to grid distance for the samples poled by the second poling procedure at U_g = 1.5 kV.

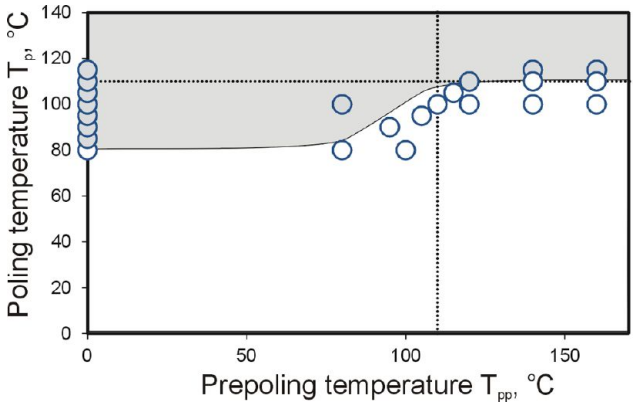

Figure 14. "Inhomogeneity" chart: surface condition at respective prepoling T_{pp} and poling T_p temperatures using the second poling procedure. The filled circles represent the samples, which have changed their surface morphology, and the empty circles represent the samples that maintained their optical properties. Black dotted lines represent the coordinates of the glass transition temperature.

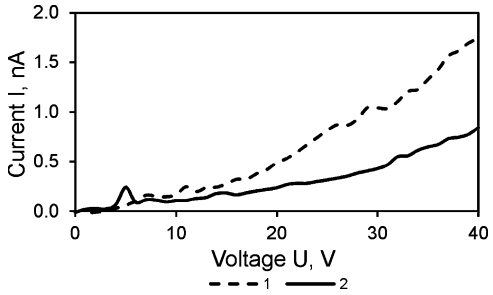

Figure 15. Current–voltage (I–V) characteristics of (1) nonpreheated and (2) preheated sample.

CONCLUSIONS

In conclusion, we have investigated morphology changes of thin host–guest polymer films caused by corona poling procedure. Formation of surface irregularities was observed by reaching threshold poling temperatures at high poling fields for all used host polymers. The appearance of irregularities may be controlled by prepoling and poling conditions. A certain prepoling procedure helps to avoid formation of irregularities. It involves the film heating to temperatures higher than the poling temperature for a short period of time with no poling field applied. This approach helps to suppress formation of inhmogeinities for PMMA, PS, and PSU thin films doped with DMABI and increases the effective NLO efficiency. We also demonstrate that greater grid to sample distances additionally help to avoid irregularities, while keeping the poling efficiency unaffected.

We propose three hypotheses that could explain the effect of surface and morphology changes in the sample during the corona poling. The inhomogenieties in the form of hollows could be formed due to high energy ion bombardment. We have shown that the density of scattering elements or hollows grows if we increase the kinetic energy of the ions, which can be done either by increasing grid voltage or by decreasing the distance between the grid and sample surface. However, we were not able to observe any changes in the sample morphology when nonpolar chromophores are dissolved in the host. This suggests that polar molecules are required in the thin film to observe formation of inhomogenieties. Thus possibly the changes in the sample morphology are induced by the poling field and chromophore dipole moment interaction, which causes mass transport to take place. The mentioned hollows could also be formed by local electrical breakdown in the film. This hypothesis is encouraged by the fact that we were able to observe a correlation between the sample conductivity and probability for the changes in sample morphology to take place during the poling. Unfortunately, the mechanism of formation of these inhomogeneities is still unclear.

AUTHOR INFORMATION

Corresponding Author

*E-mail: martins.rutkis@cfi.lu.lv.

Notes

The authors declare no competing financial interest.

ACKNOWLEDGMENTS

This work has been supported by ERDF project (agreement No. 2010/0308/2DP/2.1.1.1.0/10/APIA/VIAA/051) and by the European Social Fund within the project "Support for Doctoral Studies at University of Latvia". We also acknowledge Roberts Zabels at the Institute of Solid State Physics for the polymer hardness measurements.

REFERENCES

(1) Dalton, L. R. Rational Design of Organic Electro-Optic Materials. *J. Phys.: Condens. Matter* **2003**, *15*, 897–934.

(2) Cho, M. J.; Choi, D. H.; Sullivan, P. A.; Akelaitis, A. J. P.; Dalton, L. R. Recent Progress in Second-Order Nonlinear Optical Polymers. *Prog. Polym. Sci.* **2008**, *33*, 1013–1058.

(3) Hou, A.; Zhang, D.; Chen, K.; Yi, M. Poling of Organic Polymer Films for External Electro-Optic Measurement. *Proc. SPIE* **2000**, *3943*, 299–305.

(4) Marshall, J. M.; Zhang, Q.; Whatmore, R. W. Corona Poling of Highly (001)/(100)-Oriented Lead Zirconate Titanate Thin Films. *Thin Solid Films* **2008**, *516*, 4679−4684.
(5) Mönckе, D.; Mountrichas, G.; Pispas, S.; Kamitsos, E. I.; Rodriguez, V. SHG and Orientation Phenomena in Chromophore DR1-Containing Polymer Films. *Photonics and Nanostructures − Fundamentals and Applications* **2011**, *9*, 119−124.
(6) Yun, B.; Hui, G.; Lu, C.; Cui, Y. Study on Dipolar Orientation and Relaxation Characteristics of Guest-Host Polymers Affected by Corona Poling Parameters. *Opt. Commun.* **2009**, *282*, 1793−1797.
(7) Giacometti, J. A.; Fedosov, S.; Costa, M. M. Corona Charging of Polymers: Recent Advances on Constant Current Charging. *Braz. J. Phys.* **1999**, *29*, 269−279.
(8) Fukuda, T.; Matsuda, H.; Someno, H.; Kato, M.; Nakanishi, H. An Effective Poling of High Tg NLO Polymers. *Mol. Cryst. Liq. Cryst.* **1998**, *315*, 105−110.
(9) Vembris, A.; Rutkis, M.; Laizane, E. Influence Of Corona Poling Procedures on Linear and Non-Linear Optical Properties of Polymer Materials Containing Indandione Derivatives as Cromophores. *SPIE Proceedings, Organic Optoelectronics and Photonics III* **2008**, *6999*, 699924.
(10) Min, Y. H.; Lee, K.-S.; Yoon, C. S.; Do, L. M. Surface Morphology Study of Corona-Poled Thin Films Derived From Sol-Gel Processed Organic-Inorganic Hybrid Materials for Photonics Application. *J. Mater. Chem.* **1998**, *8* (5), 1225−1232.
(11) Hill, R. A.; Knoesen, A.; Mortazavi, M. A. Corona Poling of Nonlinear Polymer Thin Films for Electro-Optic Modulators. *Appl. Phys. Lett.* **1994**, *65*, 1733−1735.
(12) Lee, S.-S.; Garner, S. M.; Chuyanov, V.; Zhang, H.; Steier, W. H.; Wang, F.; Dalton, L. R.; Udupa, A. H.; Fetterman, H. R. Optical Intensity Modulator Based on a Novel Electrooptic Polymer Incorporating a High $\mu\beta$ Chromophore. *IEEE J. Quantum Electron.* **2000**, *36* (5), 527−532.
(13) Burland, D. M.; Miller, R. D.; Walsh, C. A. Second-Order Nonlinear Optical Active Calix[4]arene Polyimides Suitable for Frequency Doubling in the UV Region. *Chem. Rev.* **1994**, *94*, 31−75.
(14) Dalton, L. R.; Harper, A. W.; Robinson, B. H. The Role of London Forces in Defining Nocentrosymmetric Order of High Dipole Moment-High Hyperpolarizability Chromophores in Electrically Poled Polymeric Thin Films. *Proc. Natl. Acad. Sci. U. S. A.* **1997**, *94*, 4842−4847.
(15) Rutkis, M.; Vembris, A.; Zauls, V.; Tokmakovs, A.; Fonavs, E.; Jurgis, A.; Kampars, V. Novel Second-Order Non-Linear Optical Polymer Materials Containing Indandione Derivatives as Chromophores. *Proc. SPIE* **2006**, *6192*, 61922Q.
(16) Mihailovs, I.; Kreicberga, J.; Kampars, V.; Miasojedovas, S.; Jursenas, S.; Skuja, L.; Rutkis, M. Hyper-Rayleigh Scattering and Two-Photon Luminiscence of Phenylamine-Indandione Chromophores. *IOP Conf. Series: Mater. Sci. Eng.* **2012**, *38*, 012035.
(17) Vilitis, O.; Titavs, E.; Nitiss, E.; Rutkis, M. Chromophore poling in thin films of organic glasses. 3. Corona triode discharge setup. *Latv. J. Phys. Tech. Sci.* **2013**, *1*, 66−75.
(18) Mortazavi, M. A.; Knoesen, A.; Kowel, S. T. Second Harmonic Generation and Absorption Studies of Polymer-Dye Films Oriented by Corona-Onset Poling at Elevated Temperatures. *J. Opt. Soc. Am. B* **1989**, *6* (4), 733−741.
(19) Dao, P. T.; Williams, D. J.; McKenna, W. P.; Berarducci, K. G. Constant Current Corona Charging as a Technique for Poling Organic Nonlinear Optical Thin Films and the Effect of Ambient Gas. *J. Appl. Phys.* **1993**, *73*, 2043−2050.
(20) Vembris, A.; Rutkis, M.; Laizane, E. Effect of Corona Poling and Thermo Cycling Sequence on NLO Properties of the Guest-Host System. *Mol. Cryst. Liq. Cryst.* **2008**, *485*, 873−880.
(21) Rutkis, M.; Jurgis, A. Insight in NLO Polymer Material Behavior from Langevin Dynamic Modeling of Chromophore Poling. *Integr. Ferroelectr.* **2011**, *123*, 53−65.
(22) Wissinger, R. G.; Paulaiti, M. E. Glass Transitions in Polymer/CO2Mixtures at Elevated Temperatures. *J. Polym. Sci. Part B: Polym. Phys.* **1991**, *29* (5), 631−633.

Optical propagation loss measurements in electro optical host - guest waveguides

E. Nitiss*, J. Busenbergs, M. Rutkis
Institute of Solid State physics, University of Latvia, Latvia
* *Corresponding author:* edgars.nitiss@cfi.lu.lv

ABSTRACT

Thin organic waveguiding layers are applied more and more frequently as optical components in novel optoelectronic devices. For development of such devices it is important to know the optical properties of the used waveguides. One of the most important parameters is optical propagation loss in the waveguide. In this paper we present optical propagation loss measurements in planar electro optical waveguides using travelling fiber method. Using this method attenuation coefficient α at 633 nm as a function of chromophore concentration for the first two guiding modes in the slab waveguide was determined.

Keywords: organic electro optical materials, light propagation losses in waveguides, travelling fiber method.

1. INTRODUCTION

Optical waveguides are one of the key enabling elements for the development of high performance and low cost nanoscale photonics devices such as switches, modulators, sensors etc. For the later waveguides with excellent nonlinear optical (NLO) and linear optical properties have to be produced. Currently significant effort is directed towards developing organic, whether polymer or organic glass, NLO materials for the mentioned applications. These investigations are mainly driven by the fact that NLO active organic materials would possess multiple advantages over the traditional inorganic materials such as low cost, easy processability, low dielectric constants and thus could be used as electro optically active components in high bandwidth electro optic (EO) modulators [1,2]. For the development of waveguide devices the optical quality of the waveguide is a crucial factor and is one of main performance characteristics [3]. Provisionally a commercially available electro optic modulator using organic NLO material requires optical propagation loss in the waveguide to be no more than 1 dB/cm [4]. In order to fulfill this criterion one has to avoid light scattering in the core and cladding materials as well as choose the NLO core material with optical absorption as low as possible in the operating wavelength. Taking these facts into consideration it is clear that before the development of the waveguide devices the losses of the waveguides have to be estimated. There are multiple methods for measuring optical propagation losses in waveguides [5,6]. The most commonly applied is the cut-back method in which the transmission of light for waveguide with different lengths is compared [7-10]. This is a destructive method and works if one assumes that for each measurement identical coupling conditions are met. One can also use nondestructive methods such as prism coupling [11], multiple reflection [12] or scattering light methods such as travelling fiber method [11,13]. For our measurements of optical propagation losses in planar waveguides a computer controlled setup based on travelling fiber method was implemented. We used this setup for investigation of light propagation losses in planar host/guest polymer PMMA+DMABI waveguides and to determine the loss dependence on the NLO active chromophore concentration in the polymer host. The results will determine the limiting concentration of DMABI at which the propagation loss requirements mentioned previously can be satisfied. The guest concentration will also determine the load parameter an therefore the NLO efficiency of the material.

Nonlinear Optics and Applications VII, edited by Mario Bertolotti, Joseph Haus, Alexei M. Zheltikov,
Proc. of SPIE Vol. 8772, 87721L · © 2013 SPIE · CCC code: 0277-786X/13/$18 · doi: 10.1117/12.2017226

2. EXPERIMENTAL

For measuring optical propagation losses we used the travelling fiber method [14]. The prism coupling technique was applied for coupling light into planar optical waveguides [6, 15].

The principal scheme of this method is displayed in Fig. 1. The incident beam is coupled through a high refractive index prism into a planar waveguide. The light can be coupled at incidence angles that correspond to mode resonance angles in the waveguide. As optical mode propagates in the thin film part of the intensity is scattered at the waveguide – air boundary. This scattered light is collected using a multimode optical fiber. If we assume that surface roughness and waveguide inhomogeneity is maintained throughout the film and that the scattered light intensity is proportional to the light intensity in the waveguide core, then the propagation losses can be estimated. This method possesses multiple commonly known disadvantages - the waveguide surface must scatter the light which of course causes additional losses, it does not work for buried waveguides and it requires precise mechanical operation [16]. The main advantage of this method is the simplicity of execution and even though an indirect optical loss measurement is performed, it can give good results.

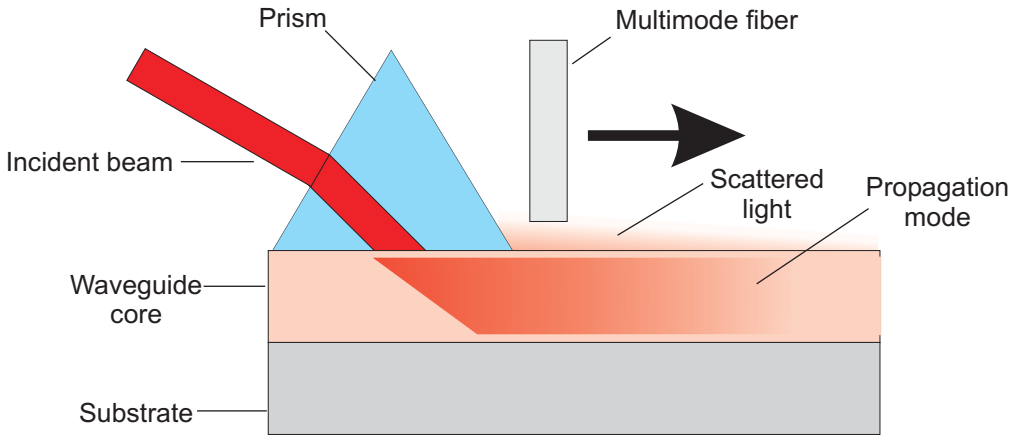

Figure 1. The principal scheme of light propagation loss measurement by travelling fiber method, the light coupling into the waveguide is performed by the prism coupling technique.

Full scheme of the experimental setup is shown in Fig. 2. The prism coupling is performed on a goniometric stage. We used a He-Ne laser as light source. Using a computer controlled motorized one axis stage the fiber can be moved along light propagation path and the scattered light can be collected. The scattered light intensity is registered using the PC.

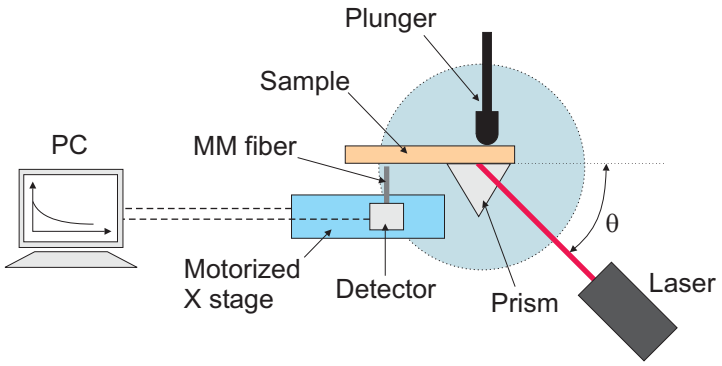

Figure 2. Experimental setup for measuring light propagation losses in planar waveguides.

Planar NLO host/guest polymer PMMA+DMABI (for detailed molecular structure see ref. [17]) waveguides, were spin-coated from a chloroform solution onto glass substrates. Guest concentrations were varied and waveguides doped at 7.5 %, 10%, 12.5% and 15% were prepared. There are two reasons why such concentrations were chosen. From the previous investigations it is expected that NLO efficiency will grow as the chromophore concentration is increased [17]. It reaches its maxima at approximately 15% which in this investigation is chosen as the upper limit of the guest concentration. The lower limit is determined by the thin waveguiding parameters where theoretically in order to have a waveguide in which at least two modes can be coupled chromophore concentration has to higher than 4.5 wt%. As will be shown later this value is underestimated. The waveguide thickness was kept constant at approximately 2 μm.

The scattered light intensity as a function of propagation length x is approximated using an exponential function

$$I = A \cdot e^{-\alpha' \cdot x}, \quad (1)$$

where A is the light intensity in counts at x=0, α' characterizes the exponential decay. If propagation length is displayed in mm, then the attenuation coefficient α in dB/cm can be expressed as

$$\alpha = 10 Log_{10}(e) \cdot \alpha', \quad (2)$$

where e is the Euler's number.

3. RESULTS AND DISCUSSIONS

The measured scattered light intensity as a function of light propagation distance is shown in Figure 3. It can be seen that light intensity decays exponentially as the light propagates through the waveguide. The experimental data do not lie smoothly on the approximation curve and some bumps can be noticed. These are caused by additional scattering elements in the sample such as dust or crystalic phase. The scattering objects are formed during the sample preparation, but should be avoided for good optical propagation loss measurement. The approximation of the experimental data shown in Figure 3 yields that the optical propagation loss for this particular measurement is 9.6 dB/cm.

The measured attenuation coefficient α dependence on the chromophore concentration in the matrix is shown in Figure 4. The loss measurements were performed for the first two TE modes of the slab waveguide. We were not able to couple the second TE mode in the waveguides with guest concentration of 7.5 wt%. Since the used laser light wavelength 633 nm is close to the absorption maxima, the measured attenuation coefficients are quite high. From the graph it can also be seen that measured attenuation coefficient values at higher guest concentrations are higher than expected (indicated by lines). This is due to the fact that at higher chromophore concentrations they tend to form crystalic aggregates which reduce the optical quality of the film. Due to this the last point of the first TE mode is no taken into account when determining attenuation coefficient dependence on chromophore concentration.

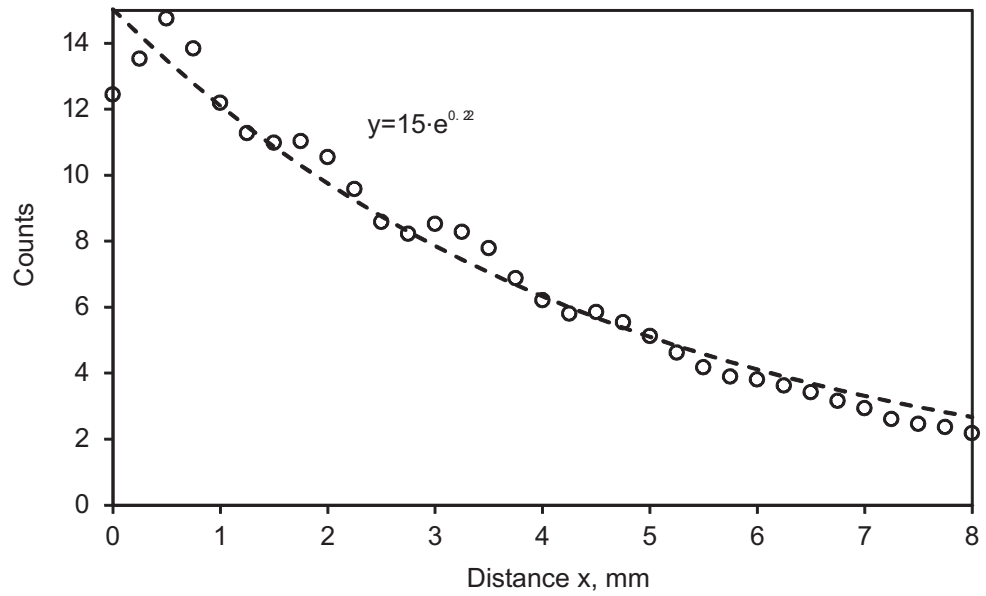

Figure 3. Scattered light intensity as a function of light propagation length x

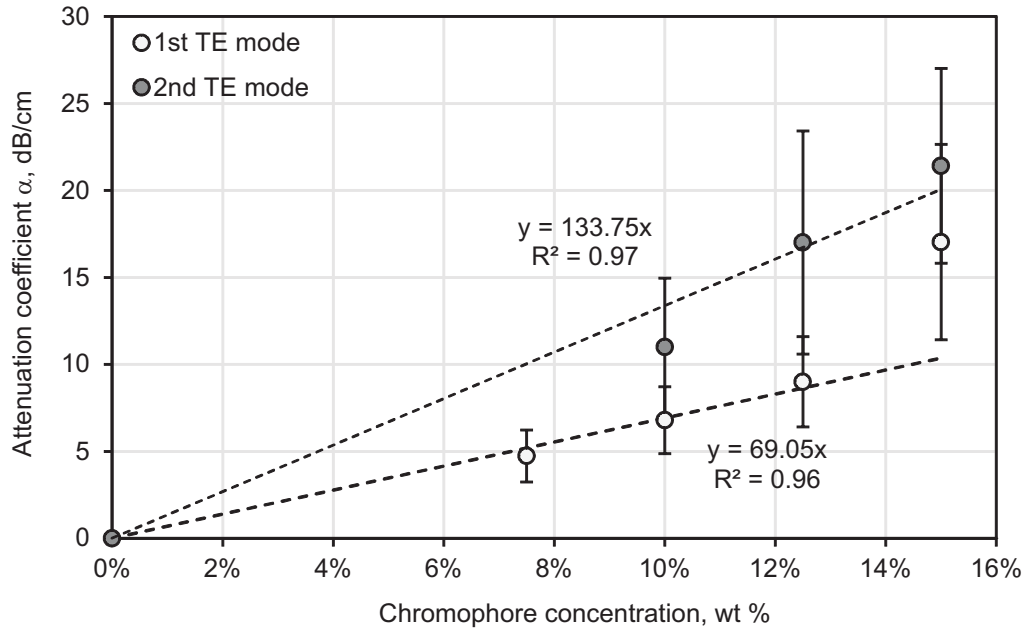

Figure 4. Attenuation coefficient α at 633 nm wavelength as a function of chromophore (DMABI) concentration in host (PMMA)

4. CONCLUSIONS

We have applied the travelling fiber method for measuring light propagation losses at 633 nm of thin organic waveguiding layers and determined the attenuation coefficient α dependence on the NLO active DMABI chromophore concentration in the PMMA matrix. It is found that α grows linearly as the chromophore concentration is increased. Linear growth can be noticed with DMABI concentration up to approximately 12.5 wt%. If the concentration is increased above the mentioned value the propagation losses grow rapidly due to formation of crystalic aggregates which increase the losses due to light scattering. So for low chromophore concentrations the attenuation coefficient is mainly determined by the light absorption, but above the critical value – by the light scattering from crystalic aggregates.

The measured propagation losses are quite high mainly due to the fact that the measurement was performed spectrally close to absorption peak which is at 490 nm. In order to satisfy the material application requirements $\alpha < 1$ dB/cm, the NLO chromophore concentration at 633 nm should be approximately 1.5 wt% which for DMABI doped PMMA thin films gives the refractive index 1.496. From this value the appropriate waveguide thickness can be found. Theoretically the waveguide thickness that would satisfy the single mode conditions in such a configuration should be around 1.3 μm.

ACKNOWLEDGEMENTS

This work has been supported by the European Social Fund within the project "Support for Doctoral Studies at University of Latvia" and by the ERDF project (agreement No. 2010/0308/2DP/2.1.1.1.0/10/APIA/VIAA/051).

REFERENCES

[1] Dalton, L., R.., "Rational design of organic electro-optic materials," J. Phys.: Condens. Matter 15, 897–934 (2003)
[2] Cho, M., J., Choi, D., H., Sullivan, P., A., Akelaitis, A., J., P., Dalton, L., R., "Recent progress in second-order nonlinear optical polymers and dendrimers," Progress in Polymer Science 33, 1013–1058 (2008).
[3] Agrawal, G., P., [Fiber Optic Communication Systems], Wiley, Third edition, 1-546 (2002).
[4] Robinson, B., H., Dalton, L., R., Harper, A., W., Ren, A., Wang, F., Zhang, C., Todorova, G., Lee, M., Aniszfeld, R., Garner, S., Chen, A., Steier, W., H., Houbrecht, S., Persoons, A., Ledoux, I., Zyss, J., Jen, A., K., Y., "The molecular and supramolecular engineering of polymeric electro-optic materials," Chemical Physics 245, 35-50 (1999).
[5] Nguyen, T.,N., Lengle, K., Thual, M., Rochard, P., Gay, M., Bramerie, L., Malaguti, S., Bellanca, G., Le, S., D., Chartier, T., "Nondestructive method to measure coupling and propagation losses in optical guided structures," J. Opt. Soc. Am B 29(12), 3393-3397 (2012).
[6] Tien, K., "Light waves in thin films and integrated optics," Applied Optics 10(11), 2395-2413 (1971)
[7] Hunsberger, R., G., [Integrated Optics: Theory and Technology], Springer-Verlag, Sixth edition, 1-501
[8] Vlasov, Y., A., Sharee, J., M., "Losses in single-mode silicon-on-insulator strip waveguides and bends," Optics Express 12(8), 1622-1631 (2004).
[9] Toyoda, S., Ooba, N., Hikita, M., Kurihara, T., Imamura, S., "Propagation loss and birefringence properties around 1.55 μm of polymeric optical waveguides fabricated with cross-linked silicone," Thin Solid Films 370, 311-314 (2000).
[10] Zhu, S., Fang, Q., Yu, M., B., Lo, G., Q., Kwong, D., L., "Propagation losses in undoped and n-doped polycrystalline silicon wire waveguides," Optics Express 17(23), 20891-20899 (2009).
[11] Weber, H., P., Dunn, F., A., Leibolt, W., N., "Loss measurements in thin-film optical waveguides," Applied Optics 12(4), 755-757 (1973).
[12] Chen, S., Yan, Q., Xu, Q., Fan, Z., Liu, J., "Optical waveguide propagation loss measurement using multiple internal reflections method," Optics Communications 256, 68-72 (2005).
[13] Wang, F., Liu, F., Chang. G., K., Adibi, A, "Precision measurements for propagation properties of high-definition polymer waveguides by imaging of scattered light," Optical Engineering 47(2), 024602-1-4 (2008).

[14] Himel, M., D., Gibson, U., J., "Measurement of planner waveguide losses using a coherent fiber bundle," Appl. Optics 25(23), 4413-4416 (1986).
[15] Ulrich, R., Torge, R., "Measurement of thin film parameters with a prism coupler," Appl. Optics 12(12), 2901-2908 (1973).
[16] Barai, S., Selvarajam, A., Srinivas, T., Madhan, T., Fazludeen, R., "A novel technique to measure propagation loss of optical waveguides," Electron devices for microwave and optoelectronics, 250-254 (2003).
[17] Rutkis, M., Vembris, A., Zauls, V., Tokmakovs, A., Fonavs, E., Jurgis, A., Kampars, V., "Novel second-order nonlinear optical polymer materials containing indandione derivativatives as a chromophore, Proceedings of SPIE," Organic optoelectronics and photonics II 6192, 61922Q (2006).

Hybrid silicon on insulator/polymer electro-optical intensity modulator operating at 780 nm

Edgars Nitiss,* Janis Busenbergs, and Martins Rutkis

Institute of Solid State Physics, University of Latvia, Kengaraga Street 8, Riga, Latvia
**Corresponding author: edgarsn@cfi.lu.lv*

Received May 22, 2014; revised July 18, 2014; accepted August 25, 2014;
posted August 25, 2014 (Doc. ID 212416); published September 24, 2014

Currently inorganic materials prevail as the nonlinear active medium for light modulation in electro-optical (EO) device technology. A recent promising trend is to consider organic nonlinear optical materials for application in EO modulators due to their multiple advantages including low costs and high EO coefficients. In this paper, we proposed a new type of polymer EO modulator whose fabrication is compatible with the currently used silicon on insulator technology. Our numerical optimization of the proposed structure demonstrates that it is theoretically possible to achieve a half-wave voltage as low as 1.56 V for a 1 cm long modulator structure operating at 780 nm. Based on the results of the numerical calculations, we also outline the advantages and drawbacks of the design.

OCIS codes: (130.4110) Modulators; (130.5460) Polymer waveguides.
http://dx.doi.org/10.1364/JOSAB.31.002446

1. INTRODUCTION

Broadband electro-optical (EO) modulators are among the key elements for the future development of communication technology. In order to satisfy the ever growing need for an increase in data transfer rate, there is a demand for a high speed, low loss, and low production cost EO modulator. Several directions of EO modulator technology development have been advanced in the last decade. It has been shown that a further increase in data transfer speeds of modulators based on inorganic EO components may be achieved by optimizing the structure and introducing new concepts and materials with enhanced nonlinear properties [1–7]. Nevertheless the main disadvantages such as high fabrication costs and dielectric losses would still remain. Furthermore, the high dielectric constants of inorganic nonlinear optical (NLO) materials set limits to the maximal bandwidth obtainable in a travelling wave modulator design. Due to the low EO coefficients of the inorganic materials, the light and the electric field interaction length should be long in order to achieve low driving voltages, thus causing the light wave and the microwave propagation velocity to mismatch [8]. Thus considerable attention has been devoted to new EO active organic materials due to their multiple advantageous properties such as low cost, easy processability, low dielectric constants, and high nonlinearity [9]. Devices based on highly NLO EO materials with EO coefficients up to 300 pm/V could satisfy the future bandwidth and chip scale requirements [10,11]. Various groups are already implementing organic materials as optical NLO active waveguide components. One of the most promising ways to introduce the organic EO material into silicon photonics would be to implement a polymer in a Si trench [12,13]. Such design is complementary metal oxide semiconductor (CMOS) compatible but is limited to operation only in the IR range. Another CMOS compatible design would employ SiN waveguides with EO active polymer claddings [14]. SiN based waveguides with EO active polymer claddings would be able to operate in the visible range but are expensive and have insufficient efficiency due to the fact that only a small part of the light penetrates the low refractive index cladding. Multiple modulator designs which are able to operate at high speeds and possess low light propagation losses and low switching voltages employ purely polymeric or hybrid waveguides [15–24]. Disadvantages of such designs are the complexity of preparation and the fact that compatible materials should be considered. From this perspective it would be highly desirable if CMOS processes could be used for the development of the design. Some new types of waveguide structures that are compatible with silicon on insulator (SOI) technology have been demonstrated earlier, most of which are hybrid or polymeric waveguides transferred to silicon or SOI wafers [25–32]. These designs possess the same disadvantages as mentioned above.

In this contribution we present a new type of a SOI/polymer EO modulator design capable of operating in the telecommunication first wavelength window. The ease of processing and the compatibility with the widely used SOI technology suggest that the proposed principle of the design can be applied for developing a wide variety of passive and active photonics components. In the suggested design, the operating wavelength of the demonstrated waveguide and the respective modulator parameters are determined by the properties of the EO polymer core. In most cases it can be used for operation in the visible spectral range, which is not accessible to the active Si lightguide components due to the high optical absorption. In the proposed structure, the doped Si serves only as an electrode and is optically isolated from the waveguide core. The mentioned wavelength range could be particularly relevant for short range communication and realising the promising concept that suggests using multimode graded index polymer optical fibers as capillaries of the network [33].

For the visible and near IR range cheap light sources and detectors could be employed.

For optimal modulator performance, one has to perform several optimization steps which include determination of the geometrical parameters for a single mode and for a nonbirefringent regime, microwave and optical refractive index matching in a travelling wave modulator, and microwave loss. In this contribution, we would like to present the optimization of hybrid SOI/polymer travelling wave Mach–Zehnder interferometric (MZI) modulator structure based on data obtained from experimental light propagation loss measurements and numerical simulations carried out with Comsol Multiphysics Modules and CAvity Modelling FRamework (CAMFR) [34].

2. SOI/POLYMER WAVEGUIDE STRUCTURE

Optical waveguides are the key building elements of integrated photonic circuits. An interesting and yet very simple waveguiding structure comprising a polymer waveguide (core) on oxidized Si (cladding) has been discussed and demonstrated [26]. We suggest extending the principle of the waveguide design—waveguide on oxidized Si—for building passive and active waveguide components on SOI platforms following the steps shown in Fig. 1.

Such waveguide design could be used for building passive, as well as active, photonic components. It is obvious that the Si layer, if doped, could serve as an electrode, thus allowing access to the EO properties of the waveguide core material.

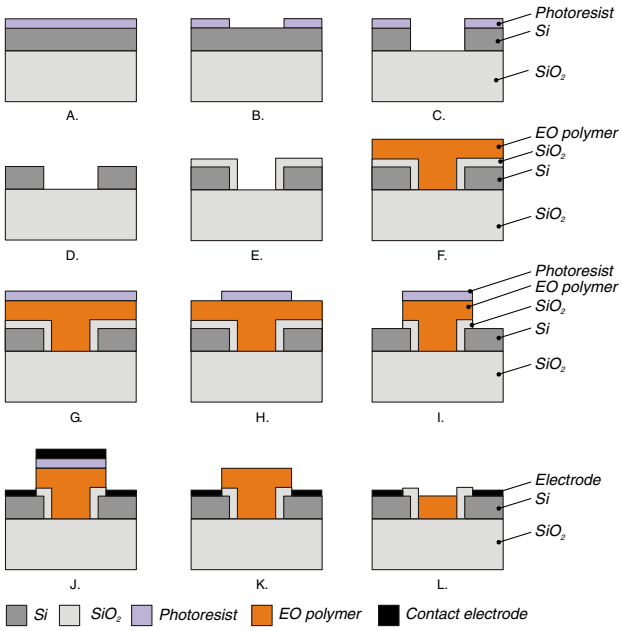

Fig. 1. Preparation steps of SOI/polymer waveguide: (a) A photoresist masking layer is applied on the SOI wafer. (b)–(d) The Si layer is patterned using conventional lithography steps, thus yielding a trench for further waveguide formation. (e) The SiO_2 cladding layer is obtained by thermal oxidation of Si for a fixed period of time to obtain the required thickness of SiO_2 [35]. (f) Afterward, a ridge waveguide core is created in the formed trench by spin coating or blade casting of EO polymer [36]. (g)–(i) Additional photolithography steps are applied in order to remove the polymer and SiO_2 layers where (j) contact metal electrodes will be applied. (k) The photoresist layer is removed and, if necessary, (l) the EO polymer thickness is reduced via etching. Step (l) is optional and could be applied in order to obtain a waveguide core with desired parameters.

The EO activity of the polymer core could be achieved during polymer poling—a procedure in which a static electric field is applied over the polymer heated close to the glass transition temperature. The reorientation and ordering of the chromophore molecules in the material yields a noncentrosymmetric structure which is compulsory for EO activity. For this purpose, a contact poling technique employing Si electrodes can be used for the proposed structure of the waveguide, and no additional electrodes are required. It should be mentioned that a high uniformity and a low conductivity of SiO_2 cladding could enable an increase in the poling voltage without an electrical breakdown of EO polymer.

One could have doubts that the waveguide mode would propagate only through the polymer core and not couple into the high refractive index Si layer. The concern was that the SiO_2 cladding layer would have to be very thick to avoid this loss. Since the thermal oxidation limit for an oxide layer of decent quality on Si is approximately 1 μm, the buffer layer will have to be less than the mentioned thickness. In Fig. 2 we show the measured propagation loss in a slab waveguide made by a spin coating guest–host system dimetilaminobenzylidene-1,3-indandione [37] + polysulphonate (DMABI + PSU) 10 wt. % waveguide ($n = 1.67$ at 780 nm) on oxidized Si substrate as a function of SiO_2 layer thickness. Even though the suggested waveguide is a ridge type waveguide, measurements of propagation loss in a slab waveguide can provide a sufficient amount of information about the behavior of light in the waveguide core. The light propagation loss was measured using the moving fiber method described elsewhere [38–40]. As can be seen in Fig. 2, the propagation loss decreases as the SiO_2 layer thickness is increased. At SiO_2 thickness of 0.7 μm, the optical propagation loss saturates at the value 5 dB/cm. This value includes both the scattering loss and the absorption loss in the waveguide core and can be reduced by decreasing the chromophore concentration in the host and by improving the smoothness of the waveguide surface. The optical propagation loss due to light penetration in the Si layer was also calculated numerically using CAMFR. In the numerical model, the waveguide core was separated by a SiO_2 waveguide cladding with various thicknesses from the absorptive Si layer.

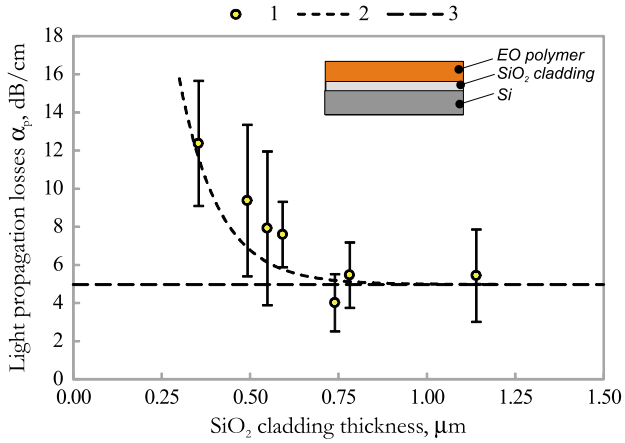

Fig. 2. Optical propagation loss α_p of a slab waveguide consisting of DMABI + PSU 10 wt. % as the waveguide core and a SiO_2 cladding layer which is on an absorbing high refractive index Si substrate: 1, experimental result; 2, numerical result obtained by CAMFR; 3, baseline corresponding only to the light propagation loss in the waveguide.

The light intensity in the core was then evaluated as the light propagated in the core. In the simulation the refractive indices of Si and SiO_2 are set to $n_{Si} = 3.9$ and $n_{SiO_2} = 1.45$, respectively. Also for propagation loss measurement it was necessary to define the extinction coefficient of Si, which was set to $k_{Si} = 0.006$. It is worth noting that in the simulation the light that has left the polymer core and penetrates the Si layer is considered lost. Therefore, it is very important to specify both of the parameters in the propagation loss calculations. As can be seen from the experimental data of the propagation loss (dots), a characteristic decrease is in good correspondence with the numerical results obtained by CAMFR (dashed line).

For low propagation loss in the etched Si waveguide structures, it is desired to have smooth sides of the waveguide. One of the great strengths of our proposed structure is the fact that after Si etching and oxidation or waveguide cladding growth, the boundaries of the waveguide are greatly improved [41].

3. PROPOSED STRUCTURE OF HYBRID SOI/POLYMER INTENSITY MODULATOR

As mentioned previously, our proposed preparation steps could be used for building active waveguide components. One such could be a MZI type hybrid SOI/polymer modulator, which is shown in Fig. 3. It consists of buried oxide or SiO_2 layers, Si elements, and the EO polymer layer. The proposed waveguide structure possesses a very important advantage over other suggested structures—it is expected to have a high overlap between the optical mode and the electrical field in the waveguide since the EO active waveguide core is very close to the doped and the conducting Si layers which could serve as electrodes. The proposed structure is simple to fabricate using commonly known methods, applying the processing steps which were illustrated in Fig. 1.

4. MODELING METHODS

To achieve an optimal optical performance of the above-described device, it is preferable to have a single mode and low birefringence conditions fulfilled in the waveguide [42–45]. A low birefringence condition is essential for having high efficiency light coupling into the device. If the effective refractive indices are equal for the TE and TM polarized light it should be possible to couple both polarizations simultaneously without losing any polarization component. Optical mode calculations were performed using the Comsol Multiphysics radio frequency (RF) module. Even though simpler and faster methods such as the Marcatillis extended approach [46] or effective index method [47] for solving two-dimensional (2D) waveguide problems can be used, the numerical full-vectorial FEM method was chosen because it gives more precise results. The polymer core should have a higher refractive index than the SiO_2 layer. To our knowledge, refractive index values up to $n_p = 1.67$ at 780 nm can be easily achieved in an organic NLO active material such as a guest–host DMABI + PSU. The refractive indices of Si and SiO_2 are $n_{Si} = 3.9$ and $n_{SiO_2} = 1.45$, respectively. Since the Si is relatively far from to EO polymer core, the n_{eff} of the waveguide depends only slightly on the real and imaginary parts of the refractive index of Si. We will use the effective refractive index n_{eff} for characterizing the optical propagation mode. For finding the single mode and nonbirefringence conditions, only geometrical parameters of the waveguide core will be varied. It is usually assumed that, in order to have the single mode condition, waveguides have to have a small cross section area. Unfortunately, the smaller the waveguide, the higher the coupling loss due to the mismatch of mode field and focal point diameters. Experiments have suggested that for a ridge waveguide the actual cross section can be increased, at the same time maintaining the single mode propagation condition [48,49]. According to [50–52], such an occurrence can be obtained by preserving a certain relation between the geometrical parameters of the ridge waveguide. To realize a single mode large cross section waveguide, the ridge waveguide width W_p and height consisting of H_{ox}, H_s, and H_p are fixed through the following relation:

$$\frac{a}{b} \le u \cdot \frac{1 - 0.05\sqrt{v^2 - 1}}{\sqrt{v^2 - 1}}, \tag{1}$$

where

$$u = \frac{q + 4\pi b}{4\pi b}, \tag{2}$$

$$v = \frac{q + 4\pi b}{q + 4\pi r b}, \tag{3}$$

$$a = \frac{W_p}{2\lambda}, \tag{4}$$

$$b = \frac{H_s + H_{ox} + H_p}{2\lambda}, \tag{5}$$

$$r = \frac{H_p}{H_p + H_s + H_{ox}}. \tag{6}$$

The parameter q for TE polarized light is expressed as

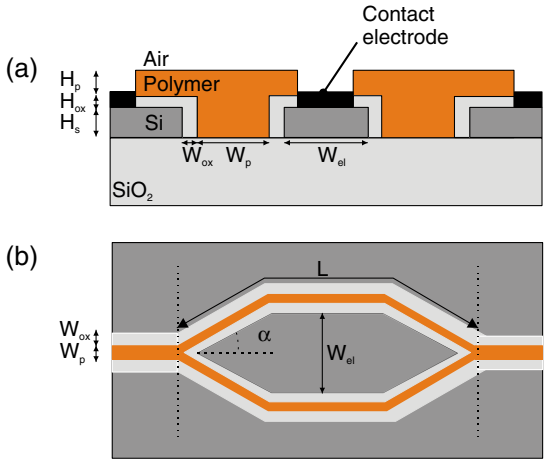

Fig. 3. (a) Cross-section and (b) top view of the MZI SOI/polymer waveguide intensity modulator: $\mathbf{W}_p$, polymer waveguide width; $\mathbf{W}_{el}$, central Si electrode width; $\mathbf{H}_s$, Si electrode height; $\mathbf{W}_{ox} = \mathbf{H}_{ox}$, SiO_2 cladding thickness; H_p, EO polymer thickness above the trench; L, length of the MZI modulator arm.

$$q = \frac{1}{\sqrt{n_{\mathrm{pol}}^2 - 1}} + \frac{1}{\sqrt{n_{\mathrm{pol}}^2 - n_{\mathrm{SiO_2}}^2}}, \tag{7}$$

and for TM polarized light as

$$q = \frac{1}{n_{\mathrm{pol}}^2\sqrt{n_{\mathrm{pol}}^2 - 1}} + \frac{n_{\mathrm{SiO_2}}^2}{n_{\mathrm{pol}}^2\sqrt{n_{\mathrm{pol}}^2 - n_{\mathrm{SiO_2}}^2}}. \tag{8}$$

Equation (1) sets the waveguide width and height ratio depending on the core and cladding refractive indices and on the slab part height of the ridge H_p and the total ridge waveguide height ratio $r > 0.5$. Such a condition restricts the propagation of the second vertical mode in the waveguide and, therefore, ensures single mode operation. The further numerical optical mode calculations will be performed for ridges that fulfill the requirements set by Eq. (1); thus the waveguides will operate in a single mode propagation regime.

As mentioned previously, high bandwidth modulators operate in the travelling wave regime. This means that the optical mode and the modulating signal, usually at the microwave frequency, propagate at the same velocity, characterized by the effective refractive indices n_{eff} and n_{mw}, respectively. The operating bandwidth of the travelling wave modulator is determined by two factors: (1) optical and microwave field velocity mismatch and (2) microwave propagation loss. Both of them are included in the simplified optical response equation for an impedance matched modulator [53]:

$$\frac{V_\pi(f)}{V_\pi(0)} = \left|\exp(-ju)\frac{\sin u}{u}\right|^2, \tag{9}$$

where

$$u = \frac{\pi f L(n_{\mathrm{eff}} - n_{\mathrm{mw}})}{c} - j\frac{\alpha(f)L}{2}, \tag{10}$$

and where L is the interaction length (see Fig. 3), c is the speed of light in vacuum, f is the microwave frequency, α is the microwave attenuation constant, j is an imaginary unit, and V_π is the half-wave voltage of the modulator. In this work, the modulator parameters will be adjusted in order for the refractive index n_{eff} and n_{mw} difference in Eq. (10) to be around zero. If the refractive index n_{eff} and n_{mw} difference is set to zero from Eq. (9), we find that the optical response equation of the travelling wave modulator will be determined by the microwave propagation loss.

To estimate the electrical parameters of the modulator, quasi static–transverse electromagnetic (TEM) analysis was used [54,55]. The quasi static–TEM analysis is a popular method for characterization of microwave transmission lines and has frequently been applied [56–61]. In this approach, the electric field calculations are performed for a static case. Even though it is a rough approximation since it does not include the frequency dispersion and other parameters of the system, it is a common, powerful, and efficient tool for most cases [62]. The finite element calculations for finding the electric field distribution were performed with the Comsol Multiphysics AC/DC module. From the electrostatic field distribution in the system it is possible to estimate the microwave effective refractive index n_{mw} and the characteristic impedance Z. In these calculations, it is necessary to define the dielectric parameters of the materials. The dielectric constants of Si, SiO_2, and EO polymer are set to be 11.7, 3.9, and 3.9, respectively. These values are estimated for the gigahertz range; thus the capacitances and characteristic impedances will also be estimated in the respective frequency range.

So the first step toward the evaluation of the microwave refractive index and characteristic impedance is to calculate the electric field distribution E in the system. Afterward the electric field intensity is integrated over the central electrode using Eq. (11), and the charge value is obtained:

$$Q = \oint_l \vec{s}\varepsilon\varepsilon_o\vec{E}\mathrm{d}l, \tag{11}$$

where s is the unit vector directed normal to the integration path, ε_o and ε are respectively the vacuum and material permittivity given above, and l is the contour path. Knowing the charge value, the capacitance can be calculated by Eq. (12):

$$C = \frac{Q}{V}, \tag{12}$$

where Q is the charge per unit length of the electrode, and V is the applied voltage difference.

The effective refractive index of the microwave n_{mw} is calculated from the ratio of capacitance C in case the electrodes are surrounded by a dielectric medium (SiO_2 and polymer) and of C_o in case the same electrodes are in vacuum. The n_{mw} is determined by Eq. (13):

$$n_{\mathrm{mw}} = \sqrt{\frac{C}{C_o}}, \tag{13}$$

where C is capacitance per unit length of the SOI modulator, and C_o is capacitance per unit length of the SOI modulator if the EO and SiO_2 layers are replaced by vacuum. If the capacitance of the system is known, it is also possible to estimate the characteristic impedance Z using Eq. (14):

$$Z = \frac{1}{c\sqrt{CC_o}}. \tag{14}$$

It is important to know the characteristic impedance Z, since the input, the output, and the active sections of the modulator should be impedance-matched for the best device performance.

In most cases, the quasi-TEM approach is extended for estimation of attenuation constant α_{mw}, which characterizes the microwave loss in the system and is calculated by the incremental inductance formula [63–65]. It would be very tempting to estimate the attenuation coefficient in our calculations in such a way; however, it would not be entirely correct. This approach can be used only for a metallic strip where the skin depth of the layer is usually smaller than the strip thickness. In the doped Si layer, the resistivity is several orders higher than that of a metal. Thus the skin depth would be comparable to the Si layer thickness. For EO modulator bandwidth estimation we will use a microwave propagation loss parameter α_{mw}, which is measured and discussed elsewhere [66]. Unfortunately, estimation of the modulator bandwidth is not a simple task because the α_{mw} is an unknown function of frequency

and therefore cannot be introduced directly in Eq. (9). Therefore, to estimate the bandwidth of the modulator a rough approximation can be used, suggesting that

$$f_{3\,\mathrm{dB}} = \left(\frac{6.84}{\alpha_{\mathrm{mw}} L}\right)^2, \tag{15}$$

where L is the length of the MZI arm (see Fig. 3), α_{mw} is the attenuation coefficient in the form of decibels per unit length normalized at 1 GHz, and 6.84 is an empirical constant. Equation (15) is an empirical equation used for estimation of $f_{3\,\mathrm{dB}}$ based on the microwave loss value at a 1 GHz frequency and gives a decent approximation of the bandwidth of the modulator [59,67]. Referring to the measurement results described in [66] at 10 GHz, we would expect a 10 dB/mm loss in Si with resistivity of 10 $\Omega \cdot$ cm.

An important parameter for characterization of the system is the half-wave voltage V_π of a push–pull MZI modulator [3], which at modulation frequency $f = f_{3\,\mathrm{dB}}$ can be estimated by Eq. (16):

$$V_\pi = \frac{\lambda W_p \eta}{2 n^3 r \Gamma L}, \tag{16}$$

where λ is the light wavelength, W_p is the waveguide core width, Γ is the overlap integral, n is the refractive index of the waveguide core, r is the EO coefficient, and η is the ratio between the voltage drop on polymer V_p and total applied voltage V. The parameter η is defined by the cladding and core thickness and the dielectric constant ratio. The overlap integral Γ value is estimated from the results obtained numerically by Eq. (17) [20,68]:

$$\Gamma = \frac{\int_{\mathrm{core}} E_{\mathrm{opt}}^2 E_{\mathrm{el}}\,\mathrm{d}S}{\int_{\mathrm{all}} E_{\mathrm{opt}}^2 E_{\mathrm{el}}\,\mathrm{d}S}, \tag{17}$$

where E_{opt} and E_{el} are the amplitudes of the optical field and modulus of the electrical field, respectively.

Optical waveguide devices require having bent and split waveguides. Since in the suggested MZI structure there are only wide angle bends, in the modeling of optical properties of the device we will only account for the optical loss caused by waveguide splitting. The MZI arm splitting angle α is shown in Fig. 3. To estimate the light power loss due to waveguide splitting, numerical simulations with the Comsol RF module were performed. The obtained results will suggest the optimal MZI modulator splitting angle α range.

5. RESULTS

A. Effective Index Matching

During the design and optimization of a travelling wave EO modulator it is necessary to consider the optical group velocity, which is a function of optical phase velocity characterized by effective optical refractive index n_{eff} and the dispersion at the corresponding wavelength. The dispersion may arise from two factors. The first factor is the dispersion in the material, and the second is dispersion due to waveguiding conditions which are wavelength dependent. In the case where large area single mode waveguides are used and the waveguide core has low dispersion, the overall dispersion can be neglected, and the group velocity is equal to phase velocity. Therefore, in our case we consider optimization of effective optical refractive index n_{eff}. For this task we will vary the geometrical parameters of the core at fixed core and cladding refractive indices. From Fig. 3 it can be seen that the geometry variables of the waveguide core are the polymer thickness above the trench H_p, trench width W_p, trench depth determined by Si layer thickness H_s, and oxide thickness H_{ox}. The H_{ox} is kept constant at 0.7 μm, which as shown previously is sufficient for the optical mode not to penetrate into the Si layer during the propagation. It is not an easy task to find the parameters for matching the effective refractive indices, because the microwave effective refractive index n_{mw} depends on the same geometrical variables as n_{eff}. An exception is the central electrode width which affects only n_{mw}.

Since we will use large cross section waveguides that will operate in a single mode propagation regime it is expected that the effective optical refractive index n_{eff} will be close to the refractive index of the core, which is 1.67. The optical mode calculations show that by changing the trench width W_p from 1.5 to 6 μm, the effective refractive index varies in the range from 1.65 to 1.66. The calculated values of TE and TM polarized light effective refractive indices and the corresponding effective mode index differences (birefringence) are shown in Fig. 4. These results indicate that we will not be able to vary the effective optical refractive index n_{eff} greatly; thus the refractive index matching should be mainly performed by adjusting the n_{mw}. Also, we were not able to reduce birefringence to zero by adjusting the geometrical parameters. It seems that due to geometrical asymmetry of the waveguide core there will always be a nonzero birefringence. However, the effective index difference of the two polarization modes can be reduced to a value less than 10^{-3}, suggesting that the light coupling loss due birefringence could be insignificant.

The refractive index matching requires the microwave effective refractive index n_{mw} to be the same as the optical effective refractive index n_{eff}. Using the formalism described above, we calculated the n_{mw} at various geometrical parameters of the modulator structure. In Fig. 5 the n_{mw} and impedance as a function of the slab thickness H_p above the trench calculated at various Si electrode heights H_s is shown.

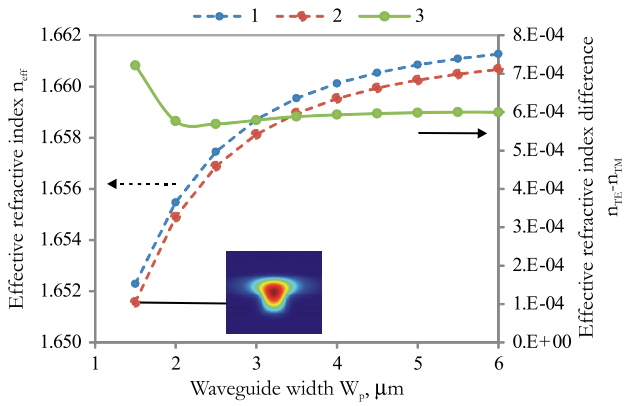

Fig. 4. Calculated values of TE and TM polarized light effective refractive indices n_{eff} and the corresponding effective mode index difference as a function of waveguide width W_p: 1 (primary axis), n_{eff} for TE polarized light; 2 (primary axis), n_{eff} for TM polarized light; 3 (secondary axis), birefringence. Other parameters are kept constant: $H_{\mathrm{ox}} = 0.7$ μm, $H_s = 0.4$ μm, $H_p = 1.1$ μm.

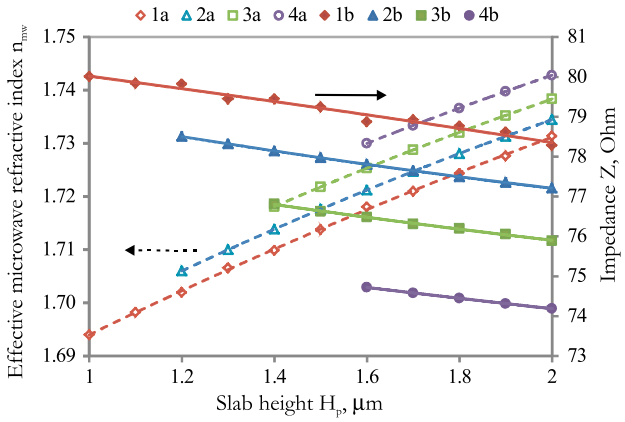

Fig. 5. Effective microwave refractive index n_{mw} (a, primary axis) and impedance Z (b, secondary axis) as a function of slab height H_p at various Si electrode heights H_s:1, $H_s = 0.3$ μm; 2, $H_s = 0.5$ μm; 3, $H_s = 0.7$ μm; 4, $H_s = 0.9$ μm. Other parameters are kept constant: $H_p = 2$ μm, $H_{el} = 70$ μm, $H_{ox} = 0.7$ μm.

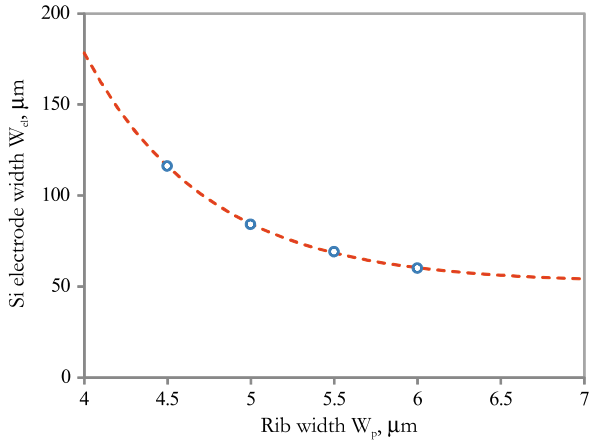

Fig. 7. Central Si electrode width W_{el} as a function of rib width W_p at which refractive indices are matched. Other parameters are kept constant: $H_p = 1.1$ μm, $H_s = 0.4$ μm, $H_{ox} = 0.7$ μm.

The data points correspond to geometrical parameters for which the ratio $r > 0.5$. As can be seen from Fig. 5, an increase in the slab thickness H_p and the central electrode height H_s gives rise to n_{mw} but lowers the impedance Z of the device. Similarly, we estimated the influence of central Si electrode width W_{el} and the rib width W_p on n_{mw} and Z. From Fig. 6 it can be seen that if the central Si electrode width and the ridge width are increased, n_{mw} decreases. The results from Fig. 5 and Fig. 6 show that the microwave can propagate faster if the bulk size of the electrode is increased. It also tells us that n_{mw} and Z cannot be simultaneously adjusted by optimization of the slab and the electrode height—we would not be able to increase or decrease both at the same time, because the incremental derivative of these values have opposite signs.

For a maximal optical bandwidth, the velocity of microwave and optical wave must be matched according to Eq. (9). As suggested by the results displayed in Fig. 6, it is possible to match n_{eff} and n_{mw} at a specific combination of the geometrical parameters of the device.

We chose to fix specific variables at the values of H_p, H_s, and H_{ox} and to find the central Si electrode width W_{el} and the respective rib width W_p relation for which the difference between n_{eff} and n_{mw} is zero. The oxide layer thickness H_{ox} is set to 0.7 μm, which is required for minimal outcoupling loss (see Fig. 2). We also set $H_p = 1.1$ μm and $H_s = 0.4$ μm since at these values n_{mw} is expected to be below the 1.67 (see Fig. 6), which is the maximal possible n_{eff}. The obtained results are displayed in Fig. 7. The red line indicates the central Si electrode width W_{el} value at which the refractive indices n_{eff} and n_{mw} are matched for the respective rib width W_p. For example, if the rib width W_p is set to be 5 μm, for the refractive indices n_{eff} and n_{mw} to be matched the Si electrode must be 84 μm wide. This gives the impedance Z value of 92 Ω. For a broadband device, the impedances between the high frequency signal generator (usually having impedance value of 50 Ω) and the device must be matched [23,53]. The obtained value of 92 Ω is quite far from the desired 50 Ω. One way of slightly reducing the impedance Z is to increase the central electrode width W_{el}. However, from the obtained results we can suggest that it will be impossible to reduce the impedance Z down to 50 Ω.

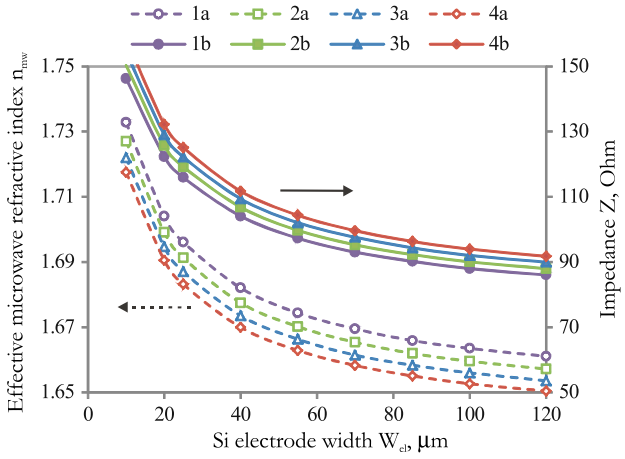

Fig. 6. Effective microwave refractive index n_{mw} (a, primary axis) and impedance Z (b, secondary axis) as a function of central Si electrode width W_{el} at various rib widths W_p:1, $W_p = 4.5$ μm; 2, $W_p = 5$ μm; 3, $W_p = 5.5$ μm; 4, $W_p = 6$ μm. Other parameters are kept constant: $H_p = 1.1$ μm, $H_s = 0.4$ μm, $H_{ox} = 0.7$ μm.

B. Microwave Propagation Loss

In an EO modulator the microwave propagation loss is usually the bandwidth limiting factor. In this section we will provide a rough estimate of microwave propagation loss in Si electrodes. Unfortunately, application of Si materials as electrodes in high speed EO devices has not yet been discussed. However, there is a paper that present Si microwave transmission coefficient measurements in the gigahertz range [66]. The gigahertz wave absorption arises from the free carriers that appear in the Si during the doping. By increasing the carrier density, the absorption is enhanced according to the Drude model [69]. As mentioned above for our rough approximation we assume that at 10 GHz, we would expect a 10 dB/mm loss in Si with resistivity of 10 Ω · cm. Then the estimated α_{mw} in Eq. (15) is ~10 dB/(GHz · cm). We will use this value to evaluate the overall performance of an optimized hybrid SOI/polymer EO modulator structure.

C. Optical Propagation Loss

The optical loss in the waveguide modulator is an important parameter for the characterization of the device performance.

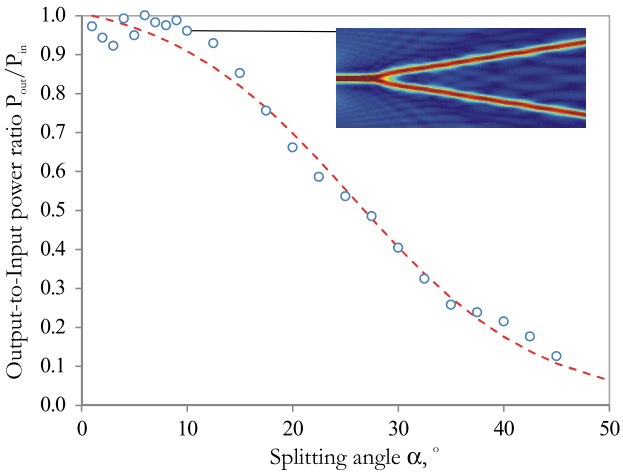

Fig. 8. 2D numerically simulated output to input power ratio P_{out}/P_{in} as a function of splitting angle α, $n_p = 1.67$.

The optical loss in the suggested structure will mainly depend on the light absorption coefficients of the waveguide material, the magnitude of the scattering at the boundary of the waveguide core interface, the light outcoupling from the core with further absorption in the Si layer, and the light coupling efficiency in the MZI arms, henceforth the output to input power ratio P_{out}/P_{in}. The ratio P_{out}/P_{in} is the light power coupled in the arms of the MZI versus the light intensity before the actual waveguide splitting. It is desired to couple as much light into the MZI arms as possible. The ratio P_{out}/P_{in} will depend on the waveguide core and the cladding refractive index difference and on the splitting angle. The splitting angle will not only determine the light power coupled into theMZI arms but also the device size. Lower splitting angles will require the modulator to be longer to achieve the optimal electrode width. It is therefore important to choose a splitting angle that will satisfy both the length and the loss requirements.

In Fig. 8 one could find the 2D numerically simulated output to input power ratio P_{out}/P_{in} as a function of splitting angle α. In the simulation, the waveguide core refractive index n_p is set to 1.67, and the cladding is SiO_2 with a refractive index of n_{SiO_2} equal to 1.45. As can be seen for lower optical loss during light coupling into the MZI arms, a significant decrease in output to input power ratio P_{out}/P_{in} takes place if the splitting angle α is higher than 10°. Thus it is suggested to choose $\alpha < 10°$.

D. Overall Performance Evaluation

Taking into account the simulation and experimental results we can estimate the parameters of the optimized structure of the proposed hybrid SOI/polymer ($n_p = 1.67$) EO modulator for operation at 780 nm.

The geometrical parameters of the optical waveguide that would operate at a single mode propagation regime and would be almost nonbirefringent are as follows: $H_p = 1.1$ μm, $H_s = 0.4$ μm, $H_{ox} = 0.7$ μm, and $W_p = 5.5$. These values were obtained during effective refractive index n_{eff} and n_{mw} matching. If the central Si electrode width W_{el} is chosen to be 84 μm, then the effective microwave and optical indices would be equal: $n_{mw} = n_{eff} = 1.658$. For the minimal optical loss in the modulator, the MZI arms should split in a <10° angle, and the SiO_2 layer should be $H_{ox} = 0.7$ μm thick. Using Eq. (17) the calculated overlap integral Γ for this system is found to be 0.96. The overlap integral Γ is almost 1 due to the fact that the optical mode almost does not penetrate into the cladding. One of the main parameters for EO modulator characterization is the half-wave voltage interaction length $V_\pi L$. If the polymer EO coefficient r_{33} is equal to 100 pm/V, then the $V_\pi L$ estimate in Eq. (16) of our proposed EO modulator at frequency $f = f_{3\,dB}$ would be around 1.56 V · cm for TE polarized light. Due to material internal symmetry the modulation of theTE mode would be higher than for the TM mode due to different effective EO coefficients. The modulation voltage for TE polarized light would be determined by r_{33} and for the TM polarized light by r_{13}, which is usually smaller than r_{33} by a factor of three. For bandwidth estimation we use Eq. (15). We assume that a commercially available highly doped Si with a rather low resistivity of 10 Ω · cm is used as an electrode for the intensity modulator. ASi electrode with such parameters results in the microwave propagation loss α_{mw} of ~10 dB/cm at 1 GHz (see Section 5.B). If the total length of the modulator is presumed to be 0.5 cm, then, at the mentioned modulator parameters, the $f_{3\,dB}$ value would theoretically be around 1.9 GHz and the half-wave voltage $V_\pi = 2.12$ V. The two most important parameters that have a crucial effect on the modulator bandwidth are the length of the modulator and the microwave propagation loss in the Si. In the case where the modulator length is increased to 1 cm, the $f_{3\,dB}$ value would drop down to around 0.5 GHz and the half-wave voltage V_π to 1.56 V.

For optical modulation, it would also be possible to use the metallic strips that are on the Si. This could enable high speed operation of the modulator for an optimized structure [70,71]. However, optimization of such a design is not the aim of this work.

6. CONCLUSIONS

We have proposed a design for a new type of hybrid SOI/polymer waveguide EO modulator that could operate both in the visible and the IR wavelength range. By optimizing the travelling wave modulator structure parameters using a rough modulator bandwidth estimation model, we have shown that it is theoretically possible to achieve a half-wave voltage interaction length of 1.56 V · cm and a bandwidth of 1.9 GHz for an MZI modulator with 0.5 cm long arms and an EO coefficient of 100 pm/V. The advantages of the proposed modulator structure that should be emphasized are the simplicity of preparation, low drive voltages values, and expected low light propagation loss.

Unfortunately, such a design also possesses an important drawback. The operational bandwidth of the MZI type EO modulator on a SOI platform would not exceed a couple of gigahertz. Thus we doubt that it could be used for an ultrahigh speed light modulation. Despite this we believe that such an active waveguide structure and preparation technology could find application in making light switches, array waveguides for dense wavelength division multiplexing, and other electro-optical devices.

ACKNOWLEDGMENTS

This work has been supported by the 2nd Latvian National Research Programme, “Development of Innovative Multifunctional Materials, Signal Processing and Information Technologies for Competitive Science Intensive Products” and by the

European Social Fund within the project "Support for Doctoral Studies at University of Latvia."

REFERENCES

1. P. Tang, D. J. Towner, T. Hamano, A. L. Meier, and B. W. Wessels, "Electrooptic modulation up to 40 GHz in a barium titanate thin film waveguide modulator," Opt. Express **12**, 5962–5967 (2004).
2. D. M. Gill, D. Jacobson, C. A. White, C. D. W. Jones, Y. Shi, W. J. Minford, and A. Harris, "Ridged $LiNbO_3$ modulators fabricated by a novel oxygen-ion implant/wet-etch technique," J. Lightwave Technol. **22**, 887–894 (2004).
3. L. N. Binh, "Lithium niobate optical modulators: devices and applications," J. Cryst. Growth **288**, 180–187 (2006).
4. A. Liu, L. Liao, D. Rubin, N. Nguyen, B. Ciftcioglu, Y. Chetrit, R. Cohen, N. Izhaky, J. Basak, and M. Paniccia, "Recent advances in high speed silicon optical modulator," Proc. SPIE **6477**, 647710 (2007).
5. Z. Lu and W. Zhao, "Nanoscale electro-optic modulators based on graphene-slot waveguides," J. Opt. Soc. Am. B **29**, 1490–1496 (2012).
6. K. Ogawa, K. Goi, Y. T. Tan, T.-Y. Liow, X. Tu, Q. Fang, G.-Q. Lo, and D.-L. Kwong, "Silicon Mach–Zehnder modulator of extinction ratio beyond 10 dB at 10.0–12.5 Gbps," Opt. Express **19**, B26–B31 (2011).
7. M. Ziebell, D. M. Morini, G. Rasigade, J.-M. Fédéli, P. Crozat, E. Cassan, D. Bouville, and L. Vivien, "40 Gbit/s low-loss silicon optical modulator based on a pipin diode," Opt. Express **20**, 10591–10596 (2012).
8. T. Liljeberg and J. E. Bowers, "Velocity mismatch limits in semiconductor lasers and amplifiers," in *Proceedings of IEEE Conference on Lasers and Electro-Optics* (IEEE, 1997), pp. 341–342.
9. R. A. Noorwood, C. Derose, Y. Enami, H. Gan, C. Greenlee, R. Himmelhuber, O. Kropachev, C. Loychik, D. Mathine, Y. Merzylak, M. Fallahi, and N. Peyghambarian, "Hybrid sol–gel electro-optic modulators: beating the drive voltage/loss tradeoff," J. Nonlinear Opt. Phys. **16**, 217–230 (2007).
10. B. H. Robinson, L. R. Dalton, A. W. Harper, A. Ren, F. Wang, C. Zhang, G. Todorova, M. Lee, R. Aniszfeld, S. Garner, A. Chen, W. H. Steier, S. Houbrecht, A. Persoons, I. Ledoux, J. Zyss, and A. K. Y. Jen, "The molecular and supramolecular engineering of polymeric electro-optic materials," Chem. Phys. **245**, 35–50 (1999).
11. S. J. Benight, D. H. Bale, B. C. Olbricht, and L. R. Dalton, "Organic electro-optics: understanding material structure/function relationships and device fabrication issues," J. Mater. Chem. **19**, 7466–7475 (2009).
12. L. Alloatti, D. Korn, R. Palmer, D. Hillerkuss, J. Li, A. Barklund, R. Dinu, J. Wieland, M. Fournier, J. Fedeli, H. Yu, W. Bogaerts, P. Dumon, R. Baets, C. Koos, W. Freude, and J. Leuthold, "42.7 Gbit/s electro-optic modulator in silicon technology," Opt. Express **19**, 11841–11851 (2011).
13. J.-M. Brosi, C. Koos, L. C. Andreani, M. Waldow, J. Leuthold, and E. Freude, "High-speed low-voltage electro-optic modulator with a polymer-infiltrated silicon photonic crystal waveguide," Opt. Express **16**, 4177–4191 (2008).
14. B. A. Block, T. R. Younkin, P. S. Davids, M. R. Reshotko, P. Chang, B. M. Polishak, S. Huang, J. Luo, and A. K. Y. Jen, "Electro-optic polymer cladding ring resonator modulators," Opt. Express **16**, 18326–18333 (2008).
15. K. Liang, Q. Song, F. Lu, B. Wu, W. Chen, H. Peng, C. Liu, and S. Luo, "Optimizing design for the traveling wave electrodes in low-drive high-speed electro-optic polymer modulators," Fiber Integrated Opt. **24**, 521–528 (2005).
16. H. Zhang, M. C. Oh, A. Szep, W. H. Steier, C. Zhang, L. R. Dalton, H. Erlig, Y. Chang, D. H. Chang, and H. R. Fetterman, "Push–pull electro-optic polymer modulators with low half-wave voltage and low loss at both 1310 and 1550 nm," Appl. Phys. Lett. **78**, 3136–3138 (2001).
17. H. Chen, B. Chen, D. Huang, D. Jin, J. D. Luo, A. K.-Y. Jen, and R. Dinu, "Broadband electro-optic polymer modulators with high electro-optic activity and low poling induced optical loss," Appl. Phys. Lett. **93**, 043207 (2008).
18. D. M. Gill and A. Chowdhury, "Electro-optic polymer-based modulator design and performance for 40 GB/s system applications," J. Lightwave Technol. **20**, 2145–2153 (2002).
19. M.-C. Oh, H. Zhang, C. Zhang, H. Erlig, Y. Chang, B. Tsap, D. Chang, A. Szep, W. H. Steier, H. R. Fetterman, and L. R. Dalton, "Recent advances in electrooptic polymer modulators incorporating highly nonlinear chromophore," IEEE J. Sel. Top. Quantum Electron. **7**, 826–835 (2001).
20. Y. Shi, W. Lin, D. J. Olson, J. H. Bechtel, H. Zhang, W. H. Steier, C. Zhang, and L. R. Dalton, "Electro-optic polymer modulators with 0.8 V half-wave voltage," Appl. Phys. Lett. **77**, 1–3 (2000).
21. F. Yi, F. Ou, B. Liu, Y. Huang, S.-T. Ho, Y. Wang, J. Liu, T. J. Marks, S. Huang, J. Luo, A. K.-Y. Jen, R. Dinu, and D. Jin, "Electro-optic modulator with exceptional power–size performance enabled by transparent conducting electrodes," Opt. Express **18**, 6779–6796 (2010).
22. I. E. Araci, R. Himmelhuber, C. T. Derose, J. D. Luo, A. K.-Y. Jen, R. A. Norwood, and N. Peyghambarian, "Alignment-free fabrication of a hybrid electro-optic polymer/ion-exchange glass coplanar modulator," Opt. Express **18**, 21038–21046 (2010).
23. C. T. Derose, R. Himmerlhuber, D. Mathine, R. A. Norwood, J. Luo, A. K.-Y. Jen, and N. Peyghambarian, "High Δn strip-loaded electro-optic polymer waveguide modulator with low insertion loss," Opt. Express **17**, 3316–3321 (2009).
24. C. T. DeRose, D. Mathine, Y. Enami, R. A. Norwood, J. Luo, A. K.-Y. Jen, and N. Neyghambarian, "Electrooptic polymer modulator with single-mode to multimode waveguide transitions," IEEE Photon. Technol. Lett. **20**, 1051–1053 (2008).
25. T. Gorman, S. Haxha, and J. J. Ju, "Novel ultra-high-speed deeply etched polymer electro-optic modulator," Proc. SPIE **7354**, 73540E (2009).
26. D. Cristea, P. Obreja, M. Kusko, E. Manea, and R. Rebigan, "Polymer micromachining for micro- and nanophotonics," Mater. Sci. Eng. C **26**, 1049–1055 (2006).
27. T. Begou, B. Beche, A. Goullet, J. P. Landesman, A. Granier, C. Cardinaud, E. Gaviot, L. Camberlein, N. Grossard, G. Jezequel, and J. Zyss, "First developments for photonics integrated on plasma-polymer-HMDSO: single-mode TE00–TM00 straight waveguides," Opt. Mater. **30**, 657–661 (2007).
28. D. S. Bodas, S. K. Mahapatra, and S. A. Gangal, "Comparative study of spin coated and sputtered PMMA as an etch mask material for silicon micromachining," Sens. Actuator A **120**, 582–588 (2005).
29. F. Dell'Olio, V. M. N. Passaro, and F. De Leonardis, "Simulation of a high speed interferometer optical modulator in polymer materials," J. Comput. Electron. **6**, 297–300 (2007).
30. W.-N. Gao, M.-Q. Tian, X.-Q. Sun, W. Wang, L. Deng, L. Gao, and D. M. Zhang, "A strip-loading optical waveguide using well poled stability organic/inorganic hybrid materials," Chin. Phys. Lett. **26**, 034205 (2009).
31. G. T. Paloczi, Y. Huang, A. Yariv, J. Luo, and A. K.-Y. Jen, "Replica-molded electro-optic polymer Mach–Zehnder modulator," Appl. Phys. Lett. **85**, 1662–1664 (2004).
32. S. Park, J. J. Ju, J. Y. Do, S. K. Park, and M.-H. Lee, "Multichannel electro-optic polymer modulator based on a novel side-chain polymer," J. Nonlinear Opt. Phys. Mater. **13**, 329–334 (2004).
33. T. Koonen, A. Ng'oma, P. Smulders, H. V. D. Boom, I. T. Monroy, and G.-D. Khoe, "In-house networks using multimode polymer optical fiber for broadband wireless services," Photon. Netw. Commun. **5**, 177–187 (2003).
34. P. Bienstman, "CAMFR," http://camfr.sourceforge.net.
35. B. E. Deal and A. S. Grove, "General relationship for the thermal oxidation of silicon," J. Appl. Phys. **36**, 3770–3778 (1965).
36. T. Suhara, "Integrated optics," in *Comprehensive Microsystems*, Y. B. Gianchandani, O. Tabata, and H. Zappe, eds. (Oxford, 2007), pp. 165–200.
37. M. Rutkis, A. Vembris, V. Zauls, A. Tokmakovs, E. Fonavs, A. Jurgis, and V. Kampars, "Novel second-order non-linear optical polymer materials containing indandione derivatives as a chromophore," Proc. SPIE **6192**, 61922Q (2006).
38. E. Nitiss, J. Busenbergs, and M. Rutkis, "Optical propagation loss measurements in electro optical host–guest waveguides," Proc. SPIE **8772**, 87721L (2013).

39. S. Barai, A. Selvarajan, T. Srinivas, T. Madhan, and R. Fazludeen, "A novel technique to measure propagation loss of optical waveguides," in *11th IEEE International Symposium on Electron Devices for Microwave and Optoelectronic Applications* (IEEE, 2003), pp. 250–254.
40. M. D. Himel and U. J. Gibson, "Measurement of planar waveguide loss using a coherent fiber bundle," Appl. Opt. **25**, 4413–4416 (1986).
41. W. H. Juan and S. W. Pang, "Controlling sidewall smoothness for micromachined Si mirrors and lenses," J. Vac. Sci. Technol. B **14**, 4080–4084 (1996).
42. T. Begou, B. Beche, N. Grossard, J. Zyss, A. Goullet, G. Jezequel, and E. Gaviot, "Marcatili's extended approach: comparison to semi-vectorial methods applied to pedestal waveguide design," J. Opt. A **10**, 055310 (2008).
43. P. D. Trinh, S. Yegnanarayanan, F. Coppinger, and B. Jalali, "Silicon-on-insulator (SOI) phased-array wavelength multi/demultiplexer with extremely low-polarization sensitivity," IEEE Photon. Technol. Lett. **9**, 940–942 (1997).
44. W. Shi, Y. J. Ding, C. Fang, Q. Pan, and Q. Gu, "Single-mode rib polymer waveguides and electro-optic polymer waveguide switches," Opt. Lasers Eng. **38**, 361–371 (2002).
45. J. Sun, C. Chen, L. Gao, X. Sun, W. Gao, C. Ma, and D. Zhang, "Polarisation-insensitive strip-loaded waveguide for electro-optic modulators and switches," Opt. Commun. **282**, 2255–2258 (2009).
46. E. A. J. Marcatili, "Dielectric rectangular waveguide and directional coupler for integrated optics," Bell Syst. Tech. J. **48**, 2071–2102 (1969).
47. G. B. Hocker and W. K. Burns, "Mode dispersion in diffused channel waveguides by the effective index method," Appl. Opt. **16**, 113–118 (1977).
48. A. G. Rickman, G. T. Reed, and F. Namavar, "Silicon-on-insulator optical rib waveguide loss and mode characteristics," J. Lightwave Technol. **12**, 1771–1776 (1994).
49. J. Schmidtchen, A. Splett, B. Schüppert, K. Petermann, and G. Burbach, "Low loss, singlemode optical waveguides with large cross-section in silicon-on-insulator," Electron. Lett. **27**, 1486–1487 (1991).
50. R. A. Soref, J. Schmidtchen, and K. Petermann, "Large single-mode rib waveguides in GeSi-Si and Si-on-SiO_2," IEEE J. Quantum Electron. **27**, 1971–1974 (1991).
51. L. Vivien, S. Laval, B. Dumont, S. Lardenois, A. Koster, and E. Cassan, "Polarization-independent single-mode rib waveguides on silicon-on-insulator for telecommunication wavelengths," Opt. Commun. **210**, 43–49 (2002).
52. S. P. Pogossian, L. Vescan, and A. Vonsovici, "The single-mode condition for semiconductor rib waveguides with large cross section," J. Lightwave Technol. **16**, 1851–1853 (1998).
53. S. Uehara, "Focusing-type optical modulator," IEEE J. Quantum Electron. **9**, 984–986 (1973).
54. Z. Pantić and R. Mittra, "Quasi-TEM analysis of microwave transmission lines by the finite-element method," IEEE Trans. Microwave Theor. Tech. **34**, 1096–1103 (1986).
55. G. K. Gopalakrishnan, W. K. Burns, R. W. McElhanon, C. H. Bulmer, and A. S. Greenblatt, "Performance and modeling of broadband $LiNbO_3$ traveling wave optical intensity modulators," J. Lightwave Technol. **12**, 1807–1819 (1994).
56. H. Chung, W. S. C. Chang, and G. E. Betts, "Microwave properties of traveling-wave electrode in $LiNbO_3$ electrooptic modulators," J. Lightwave Technol. **11**, 1274–1278 (1993).
57. N. Anwar, S. S. A. Obayya, S. Haxha, C. Themistos, B. M. A. Rahman, and K. T. V. Grattan, "The effect of fabrication parameters on a ridge Mach–Zehnder interferometric (MZI) modulator," J. Lightwave Technol. **20**, 854–861 (2002).
58. Z. Liu and D. Zhu, "A low-loss electro-optic waveguide polymer modulator and its optimization design," Opt. Quantum Electron. **37**, 949–963 (2005).
59. M. Minakata, "Recent progress of 40 GHz high-speed $LiNbO_3$ optical modulator," Proc. SPIE **4532**, 16 (2001).
60. E. J. Denlinger, "Loss of microstrip lines," IEEE Trans. Microwave Theor. Tech. **28**, 513–522 (1980).
61. Z. Liu, S. T. Ho, S. S. Chang, and T. J. Marks, "Waveguide electro-optic modulators based on organic self-assembled superlattices (SAS)," in *Conference on Lasers and Electro-Optics (CLEO)* (IEEE, 2002), pp. 196–197.
62. M. Koshiba, Y. Tsuji, and M. Nishio, "Finite-element modeling of broad-band traveling-wave optical modulators," IEEE Trans. Microwave Theor. Tech. **47**, 1627–1633 (1999).
63. H. A. Wheeler, "Formulas for skin effect," in *Proceedings of the IRE* (IEEE, 1942), pp. 412–424.
64. H. A. Wheeler, "Transmission-line properties of parallel strips separated by a dielectric sheet," IEEE Trans. Microwave Theor. Tech. **13**, 172–185 (1965).
65. G. E. Ponchak, "RF transmission lines on silicon substrates," in *29th European Microwave Conference* (IEEE, 1999), pp. 158–161.
66. T. Sameshima, H. Hayasaka, and T. Haba, "Analysis of microwave absorption caused by free carriers in silicon," Jpn. J. Appl. Phys. **48**, 021204 (2009).
67. S. Haxha, B. M. A. Rahman, and K. T. V. Grattan, "Bandwidth estimation for ultra-high-speed lithium niobate modulators," Appl. Opt. **42**, 2674–2682 (2003).
68. D.-G. Sun, Z. Liu, Y. Huang, S.-T. Ho, D. J. Towner, and B. W. Wessels, "Performance simulation for ferroelectric thin-film based waveguide electro-optic modulators," Opt. Commun. **255**, 319–330 (2005).
69. H. Engstrom, "Infrared reflectivity and transmissivity of boron implanted, laser annealed silicon," J. Appl. Phys. **51**, 5245–5249 (1980).
70. H. Berg, H. Jacobsson, K. Berg, A. Schüppen, and S. Gevorgian, "Measurement and modelling of low resistivity silicon substrate coplanar-strip (CPS) waveguides made in standard silicon technology," in *Topical Meeting on Silicon Monolithic Integrated Circuits in RF Systems* (IEEE, 2000), pp. 91–94.
71. D. Lederer and J.-P. Raskin, "Substrate loss mechanisms for microstrip and CPW transmission lines on lossy silicon wafers," Solid State Electron. **47**, 1927–1936 (2003).

Wiley Online Library
Early View publication on www.wileyonlinelibrary.com
(issue and page numbers not yet assigned;
citable using Digital Object Identifier – **DOI**)

Phys. Status Solidi A, 1–13 (2015) / **DOI** 10.1002/pssa.201532054

physica status solidi a
www.pss-a.com
applications and materials science

Review Article

Review and comparison of experimental techniques used for determination of thin film electro-optic coefficients

Edgars Nitiss*, Arturs Bundulis, Andrejs Tokmakov, Janis Busenbergs, Elza Linina, and Martins Rutkis

Institute of Solid State Physics, University of Latvia, Kengaraga 8, 1068 Riga, Latvia

Received 19 January 2015, revised 16 March 2015, accepted 2 April 2015
Published online 2 May 2015

Keywords electro-optic coefficients, electro-optical effects, nonlinear optics, organic materials, thin films

* Corresponding author: e-mail edgars.nitiss@cfi.lu.lv, Phone: +37167260787, Fax: +37167132778

The results of electro-optic coefficient measurements performed with three commonly applied techniques used to assess electro-optic coefficients: the Mach–Zehnder, the Teng–Man, and the attenuated total reflectance technique are reported. It is shown that the signal obtained by the Mach–Zehnder and Teng–Man techniques is strongly influenced by the multiple internal reflection and piezo- and electrostrictive thickness change effects, which in our opinion have not been addressed sufficiently in the literature. A novel approach based on using Abelès matrix formalism is implemented for the retrieval of electro-optic coefficients from experimental data. The measurement results, errors, and comparison of the obtained electro-optic coefficient values with the ones expected from the second harmonic generation measurements are discussed. It is demonstrated that, by applying incidence angle scan measurements in Teng–Man technique, an analytic approximation that ignores multiple internal reflection and thickness change effects can provide an electro-optic coefficient estimate within the precision of 2%. This value is much less than the error caused by the thickness change effect that may appear in the attenuated total reflectance technique which inherently has low sensitivity to the thickness modulation effects in the sample.

1 Introduction In the last decades nonlinear optical (NLO) materials have been developed, extensively studied, and applied in the industry more and more often. New low-cost materials with enhanced second order properties could be used in various electro-optic (EO) devices such as switches, modulators, tunable filters. In particular an impressive effort has lately been devoted towards the research of organic NLO materials [1]. They are especially interesting due to their low cost, low dielectric constants, high non-linearity, and other advantageous properties [2, 3]. The nonlinearity of the organic material can be characterized by means of EO coefficients. Multiple measurement techniques have been developed and applied for the measurement of EO coefficients [4–7], however, the most widely used are the Fabry–Pérot [8–10], the transmission polarimetric [11–13], the Mach–Zehnder interferometric (MZI) [14–16], the Teng–Man (TM) [17, 18] and the attenuated total reflectance (ATR) technique [19, 20]. All these methods are typically realized by detection of low amplitude EO modulations of the material subjected to a varying electric (AC) field at a frequency of several kHz. The fact that no single technique has been established as the standard for the determination of thin film EO coefficients clearly indicates that not all of the measurements, nor the respective data interpretation are straightforward. Several effects such as the multiple internal reflection (MR) effect [18, 21], the piezo- and electrostrictive thickness change (TC) effects [4, 22–24], and the modulated absorption effect [25] that impede the accurate measurement of EO coefficients have been recognized and reported earlier. The influence of each of the mentioned disturbing effects on the value being measured depends greatly on the technique and the material properties. In some cases the disturbing effects, such as TC of the sample, can cause a severe overestimation of the EO coefficients [26].

In this contribution we review and demonstrate the experimentally retrieved EO coefficients in the low

absorbing region of thin films obtained by the three of the mentioned techniques: MZI, TM, and ATR. These techniques use different phenomena to capture the same effect: refractive index change. The MZI is a two beam interferometric technique, in which the refractive index change causes light phase variations in one of the beams thus resulting in an intensity modulation at the output. In the TM method, the EO effect in the sample causes the light polarization modulations, which are transferred to light intensity modulations by an appropriate alignment of a polarizer and an analyzer. We have recognized that the signal obtained by MZI and TM techniques is strongly influenced by the MR and TC effects in the thin film, which would have been difficult to implement in an analytic description for the calculation of EO coefficients from an experiment. To avoid these difficulties we apply an effective numeric approximation of the data based on Abelès matrix formalism. Such approach enabled us to calculate the EO coefficients r_{13} and r_{33} from the experimental data. In the ATR method, the thin film optical waveguiding properties are exploited [20]. This is a very sensitive technique, in which the refractive index modulations are measured by variations in light coupling conditions. Also in the ATR measured signal the contribution from the TC effect was observed. The obtained EO coefficients have been compared to the NLO coefficients measured by the Maker fringe technique.

In the first sections of the paper, the basic theory of EO effect and the Abelès matrix formalism is provided. Then we discuss the sample design and considerations, as well as the MZI, TM, and ATR techniques separately, including the mathematical apparatus for the description of EO coefficient determination from the measured signals. We continue by demonstrating and discussing the measurement results and errors, as well as provide some conclusions that highlight the advantages and drawbacks of each method.

Edgars Nitiss received a BS and MS degree in physics from University of Latvia. Currently he is pursuing a PhD in solid state physics while working as a researcher at Institute of Solid State Physics University of Latvia. His main research interests are nonlinear optics and waveguide photonics. He is also a SPIE and an OSA student member.

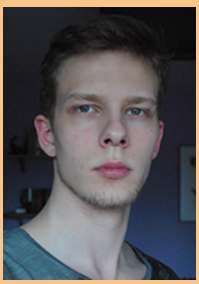

Arturs Bundulis received a BS degree in physics from University of Latvia in 2014. Currently he is a master's student at the Faculty of Physics and Mathematics of the University of Latvia. At same time he is an engineer at Institute of Solid State Physics University of Latvia where he takes part in research of organic nonlinear optical materials. Arturs Bundulis is a SPIE student member.

Dr. Martins Rutkis received his PhD from the Department of Physics University of Latvia in 1990. Presently he is the Deputy Director for Research and Head of the Laboratory of Organic Materials at Institute of Solid State Physics University of Latvia. Research interests of him are focused on structure relation to optical and NLO properties of organic materials where experimental investigations are supported by quantum chemical and molecular mechanical modelling. He is the author of 190 publications in international scientific journals, conference, and workshop contributions. Dr. Martins Rutkis is a member of OSA, ACS, and RSC and associated member of the Latvian Academy of Sciences.

2 Shortly on EO effect The EO coefficient tensor r_{ijk} characterizes the ability of a material to change its refractive index n when an external electric field E_k is applied

$$\left(\frac{1}{\Delta n^2}\right)_{ij} = \sum_k r_{ijk} E_k \tag{1}$$

Due to the Kleinman symmetry, the tensor r_{ijk} with 27 elements can be substituted by r_{hk} which is a 3×6 tensor for characterization of the effective EO response of the material after application of an electric field. An external electric field poled polymer possesses a $C_{\infty V}$ point group symmetry, the effective EO coefficient r_{ef} therefore is only determined by two independent coefficients: r_{13} and r_{33}. A simple isotropic model approximation of the order parameter in the poled polymer materials yields that for weakly poled films the r_{33}/r_{13} ratio should be within the range of 1–3 [27]. However, deviations from this model have been registered experimentally, suggesting that this ratio could be up to the value of six [11, 28].

From Eq. (1) the effective EO coefficient r_{ef} for a poled polymer film can be expressed by two independent tensor elements r_{13} and r_{33}. For the s-polarized light the r_{ef} can be written as [22]

$$r_{ef} = r_{13}, \tag{2}$$

and for the p-polarized light

$$r_{ef} = r_{13}\cos^2\theta_p + r_{33}\sin^2\theta_p, \tag{3}$$

where r_{13} and r_{33} are the EO coefficients, and θ_p is the internal angle of the refracted beam in the EO active layer

and can be determined by Snell's law if the refractive index of the EO layer n_{EO} is known.

3 Abelès matrix formalism for TM and MZI methods The application of TM and MZI methods for evaluation of the EO coefficient of the poled polymer film require a clear understanding of light intensity and phase variations caused by the sample after an AC field is applied. In most cases the samples are formed as a multilayer structure comprising electrode layers, an EO active layer and sometimes also a low conducting buffer layer such as air or an insulating polymer. Unfortunately, it is not a straightforward task to estimate the phase and intensity changes in the reflected or transmitted beams caused by the EO, piezo-, and electrostrictive TC and MR effects. We suggest using a numerical approach based on the Abelès matrix formalism for the description of the intensity and the phase of the transmitted or the reflected beams.

The Abelès matrix formalism is a simple, but a very powerful tool for optical characterization of multilayer films [29, 30] or even waveguide modes [31, 32]. The authors have previously reported the results of EO measurements where we employed the numerical approach based on Abelès matrix formalism for approximation of experimental values obtained by the MZI method [26]. In this approach, the Abelès matrix formalism has been used for estimating the transmittance T, reflectance R of the sample as well as the reflected and transmitted light phase ψ and φ, respectively, taking into account the MR and TC effect. The same approach has been used for characterization of the data obtained by TM method and is described in this paper. Such a numerical approach is quite simple to handle and can be used for describing various effects, such as electro-absorption in the thin film.

4 Multilayer samples The polymer thin film, a host-guest PMMA + DMABI 10 wt% (for the detailed molecular structure see reference [33]), used in this investigation, was spin-coated from a chloroform solution onto a standard 1 inch square indium-tin-oxide (ITO) covered glass slide (SPI Supplies, ITO sheet resistivity 70–100 Ω). Typical thickness of the polymer thin films varied from 1.5 to 2.2 μm, but the refractive index was 1.54 at 632 nm and the absorption maximum was at 490 nm. To obtain a non-centrosymmetric order in the polymer films the samples were poled using a computer controlled corona triode device [26, 34]. The m-line method was used to confirm that the material had not obtained a significant birefringence during the poling suggesting only a weak poling of the films.

The MZI technique requires the top electrode to be both conductive and semi-transparent. An aluminum (Al) layer on the top of the polymer film was sputtered. The schematic structure of the sample is shown in Fig. 1.

If an AC electrical field is applied to the electrodes of the sample, the transmission T, reflection R, the reflected light phase ψ, and the transmitted light phase φ are modulated.

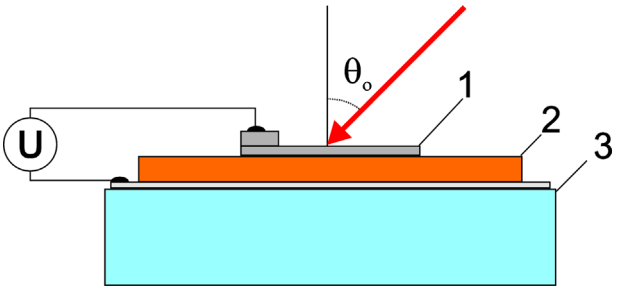

Figure 1 The polymer sample for MZI and TM measurements: 1 Al layer sputtered in two steps, 2 PMMA + DMABI 10 wt% polymer, 3 ITO coated glass, θ_o light incidence angle.

The T, R, ψ, and φ are defined by many sample and acquisition constants and variables, such as the complex refractive index N of the layers, the light polarization, the effective EO coefficient r_{ef}, the thickness of the layers, and the thickness change after the electric field is applied, the modulation voltage V and the light incidence angle θ_o on the sample.

5 MZI measurements The MZI is a two beam interferometric setup. The high sensitivity to optical path length variations in the arms of the interferometer makes it one of the most widely used optical devices in physics today. In the early work by Sigelle [14] and Singer [15] it was demonstrated that the MZI setup can be used for measuring EO coefficients of bulk crystals and thin films. Usually, the thin film under investigation introduces MR effects which have to be taken into account in the interpretation of the measured modulation values. This complicates the seemingly simple technique. Firstly, the data analysis requires cumbersome analytical [21] or numerical approaches [26] that have to be introduced for determination of the EO coefficients from the measured signal. Secondly, the experimental execution becomes time-consuming because angular scans with s- and p-polarized light incident on the sample are required [21, 26, 35]. Additionally, a noticeable error can be caused by the piezo- and electrostrictive TC effects in the sample [14, 22, 24]. In our opinion, the TC effect has not been addressed sufficiently considering the complex analytical solutions required for the complete data analysis. We demonstrate a numerical approach for the analysis of the experimental data obtained in an MZI measurement. The numerical approach is based on the Abelès matrix formalism that allows a simultaneous account for both the MR and the TC effect.

For the measurements, we have implemented an MZI setup shown in Fig. 2. The light intensity modulation I_{AC} (recovered AC signal), as well as the overall MZI output light intensity I_{DC} (recovered DC signal) (see Fig. 3) were measured with a lock-in amplifier and recorded by a computer. For adjusting the interference contrast, which is the difference between the maxima max(I_{DC}) and the minima min(I_{DC}) in the DC signal, a variable attenuator was placed in the reference arm.

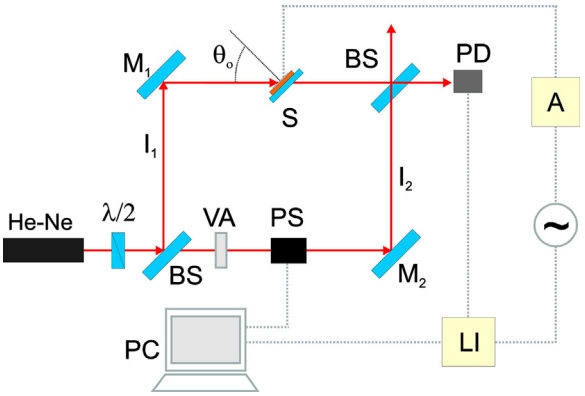

Figure 2 A schematic illustration of the MZI setup that is used for determination of EO coefficients of thin organic films. He–Ne is the helium neon laser 632.8 nm, $\lambda/2$ the half-wave plate, BS the beam splitter, M1, M2 mirrors, VA variable attenuator, PS phase shifter (Thorlabs EO-PM-NR-C1), S sample, PD a large area Si photodiode, LI lock-in amplifier (Stanford Research Systems SR830), A amplifier (Trek PZD350), PC computer, θ_o incidence angle.

For determination of both EO coefficients r_{13} and r_{33}, the AC signal measurements at various phase shift points should be collected. Moreover, such measurements should be done with an s- and a p-polarized light and at various incidence angles θ_o. The modulation frequency was set to 10 kHz in order to avoid mechanical resonances of the sample and reduce the contribution from the piezo-electric effect in the measured signal [24].

In Fig. 3, we have shown the results of measured DC (I_{DC}) and AC (I_{AC}) signals as a function of phase difference φ_o between the reference beam I_1 and the sample beam I_2. It is usually expected the phase difference $\Delta\varphi$ between the AC and the DC signal maxima to be $\pi/2$ or $3\pi/2$. This is due to a

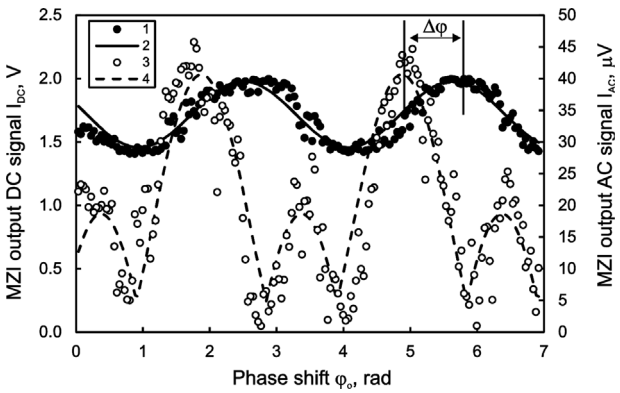

Figure 3 Typical EO measurement performed with MZI technique: (1) I_{DC} signal experimental data, (2) I_{DC} signal sine fit, (3) I_{AC} signal experimental data, (4) I_{AC} signal sine modulus fit, $\Delta\varphi$ AC and DC signal maxima phase difference. The I_{AC} experimental data have an additional offset value in the signal due to cross-talk from the sample drive signal.

simple assumption that the highest modulation efficiency (highest AC signal amplitude) should be proportional to the derivative of the DC signal. Unfortunately, the multiple internal reflection and the thickness change effects can cause variation of $\Delta\varphi$ around the mentioned $\pi/2$ [21, 26]. Nevertheless, for the registered AC and DC, the approximation simple sine fits can be used in the form

$$I_{DC} = A_{DC}\sin(\varphi_o) + B_{DC}, \tag{4}$$

$$I_{AC} = |A_{AC}\sin(\varphi_o + \Delta\varphi) + B_{AC}|, \tag{5}$$

where φ_o is the phase difference between the sample and the reference beams, A_{AC} and A_{DC} are the amplitudes of sine fits, B_{DC} is the offset of the DC signal sine fit, and the B_{AC} is the offset created by electrical cross-talk. The modulus in Eq. (5) is used due to the fact that the signal obtained in the lock-in amplifier is always positive. As it will be shown later, for data approximation and retrieval of real part of EO coefficients using MZI and TM techniques, it is sufficient to use only the ratio of A_{AC} and A_{DC} in the form

$$m = \frac{A_{AC}}{A_{DC}}. \tag{6}$$

To facilitate the further reading, the variable m will be referred to as the "AC and DC amplitude ratio" keeping in mind that it is actually the amplitudes of the sine fits of I_{AC} and I_{DC} signals obtained from the phase shift φ_o scan in the MZI method.

The experimental results displayed in Fig. 3 can also be simulated numerically. For this the MZI interference formula employing the light phase and Fresnel coefficients obtained by the Abelès matrix formalism can be used. The light intensity at the MZI output can be written as

$$I_{MZI} = \frac{1}{2}\left(I_1 + |t|^2 I_2 + 2\sqrt{I_1 I_2 |t|^2}\cos(\varphi_i + \varphi_o)\right), \tag{7}$$

where I_1 and I_2 are the reference and sample beam intensity after the first beam splitter, t the transmission amplitude of the sample, φ_i is the additional phase difference caused by the sample. In this approach a numerical fit of the experimental data is performed via simulating the experiment numerically. The intensity and the phase values in Eq. (7) can be obtained numerically by Abelès matrix formalism [26]. During the experimental data fit the EO coefficients of the thin film were set as adjustable variables. All data were processed using a MatLab code.

Before the approximation of the experimental data, we had performed simulations of the AC and DC signal ratio dependence on the incidence angle. The normalized AC and DC signal ratio m as a function of incidence angle at various EO active thin film thicknesses is shown in Fig. 4.

In case there were no MR and TC effects in the sample a simple analytic approximation could be used [15]. In this

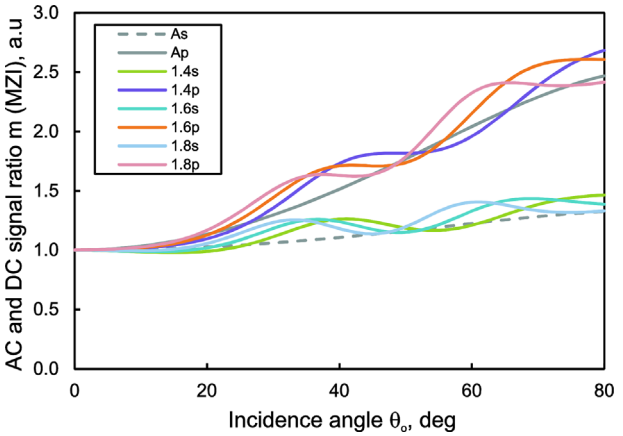

Figure 4 Normalized AC and DC signal ratio as a function of incidence angle at various EO active thin film thicknesses (s and p indicate the incident light polarization) corresponding to the refractive index change of Δn and r_{33}/r_{13} ratio of 3: A – simple analytic solution using (2), (3), and (8); 1.4, 1.6, 1.8 – numeric solution with included MR for 1.4, 1.6, and 1.8 μm thick films with refractive index $n_{EO} = 1.54$.

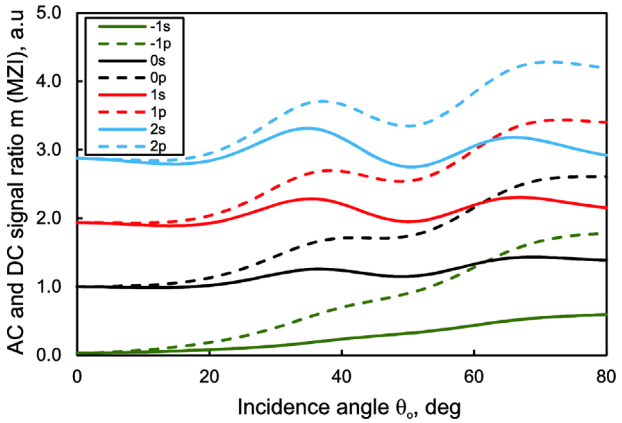

Figure 5 The calculated normalized AC and DC signal ratio m as a function of incidence angle at various EO active thin film thickness modulations. The s and p indicate the incident light polarization. The m value is calculated for a 1.6 μm thick film with refractive index $n_{EO} = 1.54$, refractive index change of Δn and r_{33}/r_{13} ratio of 3. "0" is the numeric solution with no thickness modulations, only with EO modulations Δn. "−1", "1", and "2" are the numeric solution for simultaneous EO modulations and thickness modulations Δl for cases when $(n \cdot \Delta l)/(l \cdot \Delta n) = -1$, $(n \cdot \Delta l)/(l \cdot \Delta n) = 1$, and $(n \cdot \Delta l)/(l \cdot \Delta n) = 2$, respectively.

approximation it is assumed that the amplitude m is proportional to the effective EO coefficient r_{ef} from Eqs. (2) and (3). This analytic approximation is indicated by the lines A_s and A_p for the s- and the p-polarized light, respectively. To account for the MR and the TC effect, the EO caused intensity modulations are solved numerically using the formalism described above. The lines indicate the numerical solution for the AC and DC signal ratio as a function of incidence angle for 1.4, 1.6, and 1.8 μm thick films with refractive index of $n_{EO} = 1.54$. It can be noticed that the multiple internal reflections is one of the effects that affects the line shape of the AC and DC signal ratio function. In terms of the experimental data approximation, it should be possible to obtain a higher precision of the measured EO signal approximation if the MR effects were introduced into the model.

In Fig. 5, the normalized AC and DC signal ratio as a function of incidence angle at various EO active thin film thickness modulations is shown. The m value as a function of an incidence angle for the case of a purely EO effect caused EO modulations are indicated with 0 s and 0 p for the s- and the p-polarized light, respectively. The refractive index change can be written as

$$\Delta n = -\frac{1}{2} n^3 r_{ef} E, \tag{8}$$

thus the optical path length change due to the EO effect in the sample is negative. Another effect that should be considered during the interpretation of the experimental data is the TC effect in the sample. In case the TC effect is included, it should be possible to observe either an increase, or a decrease of the thickness of the sample upon the application of an electric field. If the thickness of the film decreases, the optical path length in the sample also decreases causing the EO and the TC effects to "add up." The measured AC and DC signal ratio m is indicated by curves 1 s, 1 p and 2 s, 2 p in Fig. 5 for the cases where $(n \cdot \Delta l)/(l \cdot \Delta n) = 1$ and $(n \cdot \Delta l)/(l \cdot \Delta n) = 2$, respectively. As can be noticed, the measured m value is increased in comparison to the values obtained if only EO modulations take place. If such data are analyzed and if the thickness modulation effects are not considered, the EO coefficient value can be overestimated. It may also be that the thickness of the film increases after the electric field is applied. Following the same considerations as above, in such case the EO coefficient value could be underestimated if the TC effect is not taken into account. Therefore, additional experiments for estimating the TC should be performed before the interpretation of the EO measured data. It is important to determine not only the amplitude of the TC, but also the sign of the TC effect. For measuring the thickness modulations in our experiments, we used an MZI operating in the reflection configuration [26]. In such setup the mirror M1 (see Fig. 2) is replaced by a sample with a reflecting Al layer facing the beam. The characteristic thickness modulation amplitude was taken into account for the determination of EO coefficients using the TM, MZI, and ATR techniques.

An experimental observation of the AC and DC signal ratio m variations as a function of incidence angle using MZI setup is shown in Fig. 6. The measurement was performed for a 1.6 μm thick PMMA + DMABI 10 wt% polymer film. To estimate the EO coefficient, we first measured the thickness modulation amplitude. Using the MZI in reflection setup, the thickness change was estimated to be around

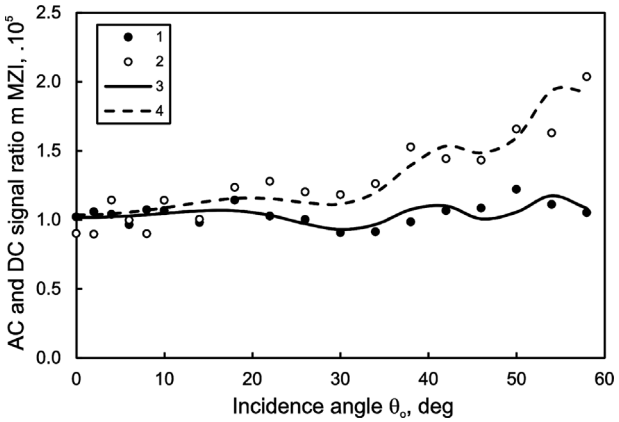

Figure 6 Measurement by MZI setup and data approximation of AC and DC signal ratio m as a function of incidence angle: (1, 2) AC and DC signal ratio measured s- and p-polarized light, respectively; (2, 4) MatLab fit to functions based on Abelès matrix formalism for s- and p-polarized light, respectively. The calculated EO coefficients are $r_{13} = 0.042$ pm/V and $r_{33} = 0.128$ pm/V.

0.25 pm/V. It is important to note that in our case the thickness of the film increased, meaning that the thickness and refractive index variations would operate conversely – one effect would decrease the optical propagation length, while the other would increase it. Then using the MatLab fit to functions based on the Abelès matrix formalism from the data displayed in Fig. 6, we calculated the EO coefficients to be $r_{13} = 0.042$ pm/V and $r_{33} = 0.128$ pm/V, respectively. As it is evident from Fig. 6, more than 20 data points were required to determine the EO coefficient. Each of the points in the graph is obtained from a scan over phase as shown in Fig. 3. Clearly, such experimental and data processing effort for a correct determination of EO coefficients causes the method to be quite time-consuming.

6 TM measurements The TM technique was independently introduced by Teng and Man [17] and by Schildkraut [18] and has been extensively used ever since. In the TM setup, phase variation between the orthogonally polarized components of the beam, caused by the EO effect, is registered. Similarly as in the MZI technique, multiple internal reflection effects should be taken into account for correct interpretation of the measured values [18, 36]. Profound analysis of the influence of MR effects on the TM measurements can be found in the recent work by Park [25]. However, the effect of TC on TM measurement has not been addressed in literature. Most of the authors assume weak or no piezoelectric contributions [7, 25]. As will be shown later, the TC may influence the results significantly in case they are comparable with the EO modulations. We have implemented a numerical approach based on the Abelès matrix formalism, which allows one to account for multiple internal reflection and TC effects simultaneously in the measurement performed by TM technique.

The TM setup was implemented as shown in Fig. 7. In this method, an incident polarized beam travels through a

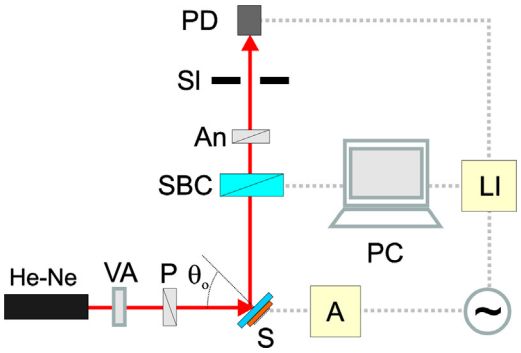

Figure 7 TM setup for determination of EO coefficients of a thin organic film. He–Ne helium neon laser 632.8 nm, VA variable attenuator, P polarizer, S sample, SBC Soleil–Babinet compensator, An analyzer, Sl slit, PD photodiode, LI lock-in amplifier, A amplifier, PC computer, θ_o incidence angle.

glass substrate, an ITO semitransparent electrode, and a polymer film, then the beam is reflected from an Al-coated reflecting layer and passes the above mentioned layers in reverse order. Due to travelling through the multiple layers, including the EO layer, the beam experiences phase retardation, which is different for the s- and for the p-polarized light. The EO effect is measured by estimating the phase shift difference of the reflected s- and p-polarized waves after the modulating electric field is applied across the sample. For such measurement, a Soleil–Babinet Compensator (SBC) is required. It introduces a controllable phase shift of the s- and the p-polarized light waves and allows a phase shift scan.

In contrast to the MZI method, the measured signal with the TM method is less sensitive to the mechanical vibrations of the optical components. This means that each data point could be obtained in less time, because the integration times at each measurement point can be significantly shortened. A typical EO measurement performed with the TM technique is shown in Fig. 8. Similarly as in the data measured by the MZI technique, the TM EO modulation experiments

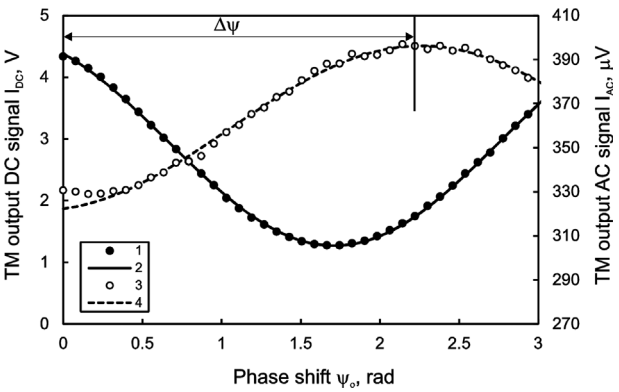

Figure 8 Typical EO measurement performed with TM technique: (1) I_{DC} signal experimental data, (2) I_{DC} signal sine-squared fit, (3) I_{AC} signal experimental data, (4) I_{AC} signal sine-squared fit, $\Delta\psi$ AC and DC signal maxima phase difference.

confirmed that the highest modulation amplitude is not at the steepest slopes of the DC curve. This is again mainly due to MR and TM effects in the sample. The output DC signal in the TM method can be described using the following equation:

$$I_{\mathrm{TM}} = \frac{I_{\mathrm{o}}}{4}\left(|r_{\mathrm{s}}| + |r_{\mathrm{p}}|\right) + I_{\mathrm{o}}|r_{\mathrm{s}}||r_{\mathrm{p}}|\sin^2\left(\frac{\psi_{\mathrm{s}} - \psi_{\mathrm{p}} + \psi_{\mathrm{o}}}{2}\right), \quad (9)$$

where I_{o} is the intensity of the incident beam and ψ_{o} is the phase difference of the s- and the p-polarized beams set by the SBC. As shown by Levy [36], for the determination of the EO coefficient, it is necessary to record incidence angle dependence of the AC signal value at bias points of the I_{TM} function (9). The bias points correspond to the phase difference $\psi_{\mathrm{o}} = 0$, $\pi/2$, π, and $3\pi/2$. This means that recording and approximation of four incidence-angle-dependent AC signal data-points is necessary for the retrieval of the real and the complex EO coefficient values. We will demonstrate that for data approximation in case of the TM techniques and for determination of EO coefficients, similarly as in the MZI method, it is sufficient to use only the ratio m (see Eq. (6). The m value should be measured over a range of incidence angles θ_{o}.

For approximation of the measured data, we use the same approach as in MZI method discussed in the previous section. Firstly, the AC and DC signal ratio m (6) is measured at various incidence angles θ_{o}. Then, using a Matlab code, the experiment is simulated numerically by using the relation for calculating the DC values from Eq. (9). It is done in the following way. By varying the parameters of the EO thin film a numerical derivative of I_{TM} in Eq. (9) as a function of ψ_{o} is obtained. This value which is obtained numerically corresponds to the AC signal. Afterwards the m value which is the ratio of AC and DC signals is calculated. The value m depends on the EO and the TC modulations in the sample. Thus, the experimentally obtained m values can be described numerically by fitting the EO coefficient r_{13} and r_{33} values. An analytic function (10) can also be used for fitting the experimental values m and thus retrieving the EO coefficients [18]

$$m = \frac{4\pi E r_{33} n_{\mathrm{EO}}^3 \tan\theta_{\mathrm{p}} \sin\theta_{\mathrm{p}}}{3\lambda l}. \quad (10)$$

This function does not account for the MR or the TC effects. Moreover, it is assumed that the ratio $r_{33}/r_{13} = 3$, meaning that only one of the EO coefficients can be determined. Nevertheless, we will later show that even such approximation can give results which differ only slightly from the ones obtained by the more complicated approach demonstrated here.

As in the case of MZI method, also when employing the TM method it is worthwhile to understand how the AC and DC signal ratio depends on the incidence angle, considering also the MR and the TC effects. In Fig. 9, the simulation of a normalized AC and DC signal ratio is shown as a function of incidence angle at various EO active thin film thicknesses. The analytic solution (10) indicated by the solid line A does not account for the MR and TC effects in the EO active film. From the simulated data in Fig. 9, two features should be outlined. Firstly, the MR effect has caused a modulation at 0° incidence angle. Clearly, at this angle there is no difference in the phase modulations of the s- and p-polarized light. This effect therefore should be attributed to the modulations of Fresnel reflection coefficients of the multilayer sample. The second effect that arises from the multiple internal reflections is that the AC and DC signal ratio dependence on the incidence angle obtains a wave-type shape. The period of the line oscillations is a function of thicknesses and refractive indices of the layers. Furthermore, at greater incidence angles, the AC and DC signal ratio is determined by r_{33}/r_{13} and r_{13}. Numerical modeling of experiment has shown that the higher the r_{33}/r_{13} ratio, the steeper is the slope of the m dependence on the light incidence angle. Numerical simulations were performed in order to evaluate the effect of thickness modulations in the TM measurements. The normalized AC and DC signal ratio as a function of incidence angle at various EO active thin film thickness modulations for a 1.6 μm thick film are shown in Fig. 10. It can be noticed that the TC effects cause oscillations of the AC and DC signal ratio as a function of the incidence angle. This clearly suggests that for correct determination of EO coefficients in a TM setup it is important to obtain a modulation function as a function of the incidence angle. In case the thickness modulations are present, the measurement at a single incidence angle θ_{o} could be misinterpreted.

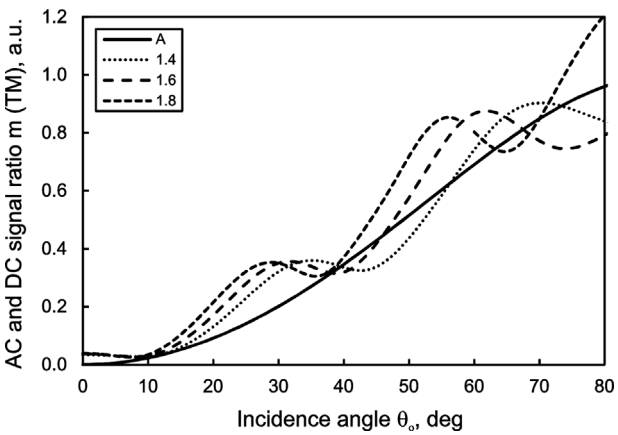

Figure 9 Normalized AC and DC signal ratio m as a function of incidence angle θ_{o} at various EO active thin film corresponding to the refractive index change Δn and the ratio $r_{33}/r_{13} = 3$. The m value is normalized to the maxima of simple analytic solution (10) indicated by line A: A simple analytic solution (10); 1.4, 1.6, 1.8 – numeric solution for 1.4, 1.6, and 1.8 μm thick films with refractive index $n_{\mathrm{EO}} = 1.54$.

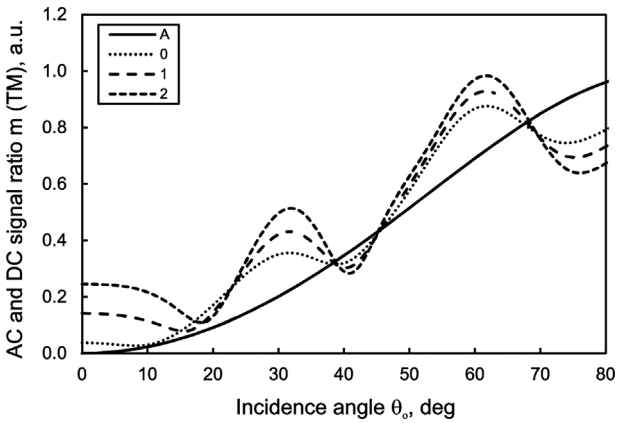

Figure 10 Normalized AC and DC signal ratio m as a function of incidence angle θ_o at various EO active thin film thickness modulations for a 1.6 μm thick film with refractive index $n_{EO} = 1.54$ and refractive index change of Δn the ratio $r_{33}/r_{13} = 3$: (1) simple analytic solution (10) with no thickness modulations included; (0) numeric solution with no thickness modulations, but with multiple internal reflections; (1, 2) numeric solution for refractive index modulations Δn and thickness modulations Δl such that $(n \cdot \Delta l)/(l \cdot \Delta n) = 1$ and $(n \cdot \Delta l)/(l \cdot \Delta n) = 2$, respectively.

For the TM measurements we used the same set of samples that were used to test the MZI technique, thus the thickness modulations of the samples were known. A measurement of the AC and DC signal ratio as a function of the incidence angle using the TM setup is shown in Fig. 11. By applying the fit based on the Abelès matrix formalism from the data displayed in Fig. 11 and taking into account the measured thickness modulations of 0.25 pm/V, the EO coefficients for a 1.64 μm thick PMMA + DMABI 10 wt% polymer film were calculated to be $r_{13} = 0.051$ pm/V and $r_{33} = 0.139$ pm/V. Fitting of the same experimental data with an analytic function (10) gave very similar results: $r_{13} = 0.045$ pm/V and $r_{33} = 0.135$ pm/V. This suggests that in most cases, if an angular measurement of the AC and DC signal ratio m is recorded, a fit with an analytic function can be used instead of a more complicated MatLab fit to functions based on the Abelès matrix formalism.

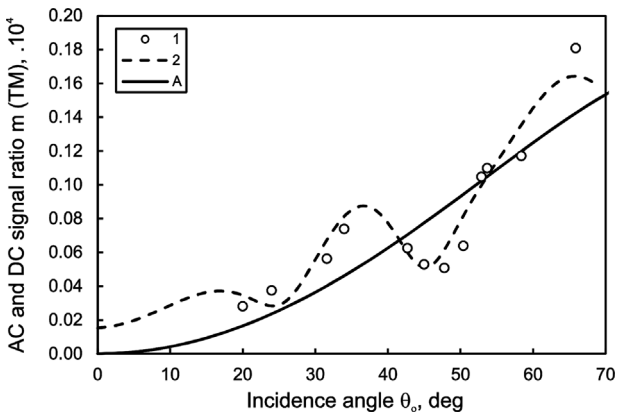

Figure 11 Measurement by the TM setup and data approximation of AC and DC signal ratio as a function of incidence angle: (1) measured AC and DC signal ratio, (2) MatLab fit to functions based on Abelès matrix formalism, (A) fit with analytic function (10). The calculated the EO coefficients from 2: $r_{13} = 0.051$ pm/V and $r_{33} = 0.139$ pm/V; EO coefficients from 3: $r_{13} = 0.045$ pm/V and $r_{33} = 0.135$ pm/V.

7 ATR measurements The ATR technique used for the determination of EO coefficients exploits waveguiding properties [37] of the thin polymer film under investigation [19, 20]. One of the great strengths of the method is that it enables direct determination of both EO coefficients of the thin film. However, the method requires the samples to be low-absorbing, with low-roughness surfaces, and to be prepared as waveguides. Despite these strict sample requirements it is still one of the most frequently used methods [38–40]. Soon after the first demonstration of the application of the ATR for measuring EO coefficients of thin polymer films [20], Dumont and coworkers presented an extensive analysis on the influence of the TC effect on the ATR measurement [4].

The ATR setup was implemented as shown in Fig. 12. In this method a polarized beam is coupled into the sample using a high refractive index prism. The sample and the prism are located on a computer-controlled rotary stage that allows varying the incidence angle Θ on the high refractive index prism. The light reflected from the prism's base facet is collected using a large area photodiode. The coupling point on the prism is coated with Al or gold (Au) which serves as an electrode and is used for applying the electric field on the sample. The drop in the reflected light intensity R and the change in the modulated signal amplitude ΔR are registered at the resonance angles that correspond to the light coupling (mode excitation) condition.

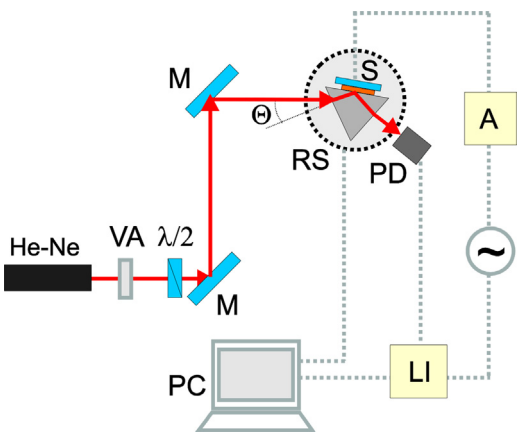

Figure 12 ATR setup for determination of EO coefficients of a thin organic film. He–Ne helium neon laser 632.8 nm, VA variable attenuator, $\lambda/2$ half-wave plate, M mirror, RS rotating stage, Θ the incidence angle on the high refractive index prism, S sample, PD photodiode, LI lock-in amplifier, A amplifier, PC computer.

For experimental data interpretation in this work, we have used the approach by Dumont [4] which for a non-birefingent thin film describes the modulated signal for an s- and a p-polarized light in the following form:

$$\Delta R_s = \frac{\partial R_s}{\partial d}\Delta l - \frac{\partial R_s}{\partial n_{ef}} \cdot \frac{1}{2} n^3 E r_{13}, \quad (11)$$

$$\Delta R_p = \frac{\partial R_p}{\partial d}\Delta l - \frac{\partial R_p}{\partial n_{ef}} \cdot \frac{1}{2} n^3 E (r_{13} + r_{33}), \quad (12)$$

where ΔR_s and ΔR_p are the modulated signal amplitudes (ATR output AC signal) for the s- and the p-polarized light, respectively, R_s and R_p are the reflected light intensities for the s- and the p-polarized light (ATR output DC signal), respectively, l is the thickness of thin film, Δl the thickness change of the thin film. As is evident from Eqs. (11) and (12), for the determination of EO coefficients the thickness changes should be known. A great advantage of the ATR method is that, in case the waveguide allows multiple transfer-electric and transfer-magnetic guiding modes, then during the data analysis of the modulated signal the EO and thickness modulations can be decoupled [4]. Unfortunately, for our samples in most cases only the first transfer-electric and transfer-magnetic modes could be observed. Therefore, for determination of the EO coefficient we used an overestimated value of the thickness change Δl corresponding to 2 pm/V. As will be shown later in the "Comparison of methods," this has a small effect on the precision of the determined EO coefficients using the ATR method.

A typical EO measurement performed with the ATR technique is shown in Fig. 13; a drop in the reflected light intensity or the DC signal is evident. This drop corresponds to the coupling of the incident light into the first mode of the waveguide. The refractive index of the polymer is 1.54, thus any mode should have a corresponding effective refractive index below this value. However, the observed first mode of the waveguide is above the mentioned 1.54. This is due to the 50 nm thick bottom electrode ITO layer, which has the refractive index of around 1.8. Together with the polymer it causes the effective refractive index of the first coupled mode to be higher than that of the polymer alone. The AC signal retrieved by lock-in amplifier is plotted against the secondary axis of Fig. 13. From the AC and the DC signal data, the EO coefficient can be obtained by comparing the AC signal with the DC signal derivative with respect to the n_{ef}. Both of these curves are proportional to each other and their ratio will determine the EO coefficient. The retrieval of EO coefficients is done in the following steps. Firstly, a derivative of R_s (R_p) value or the DC signal with respect to the n_{ef} is obtained. The numerical derivative of the experimentally obtained R_s (R_p) data points is "noisy." To reduce this "noise" the R_s (R_p) should be firstly smoothed or fitted and the derivative should be calculated from the respective smooth or fit function. We fitted the R_s (R_p) with a function that has an analytical derivative within the approximation range. For approximation of R_s (R_p) we have used a sum of multiple Gauss functions, after which an analytic derivation with respect to the n_{ef} is performed. Then the obtained derivative function is used for approximation of the experimentally obtained AC signal or the ΔR_s (ΔR_p) by using Eqs. (11) and (12) [20]. Such approximation requires knowing all of the partial derivatives of $\partial R_s/\partial n_{ef}$ ($\partial R_p/\partial n_{ef}$), which are setup and prism material dependent and are calculated analytically. For this particular measurement we calculated the EO coefficients to be $r_{13} = 0.25$ pm/V and $r_{33} = 0.54$ pm/V.

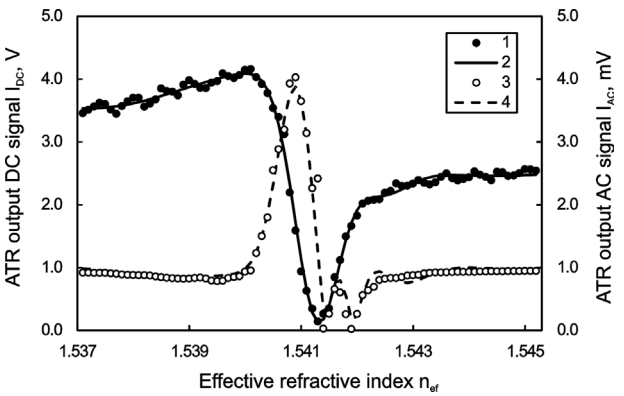

Figure 13 Typical EO measurement for s-polarized light performed with ATR technique: (1) I_{DC} signal experimental data, (2) I_{DC} signal multiple Gauss fit, (3) I_{AC} signal experimental data, (4) I_{AC} signal fit using derivative of I_{DC} signal multiple Gauss fit; the calculated EO coefficients: $r_{13} = 0.25$ pm/V and $r_{33} = 0.54$ pm/V.

8 Determination of NLO coefficients and their relation to EO coefficients In addition to the EO we also determined the NLO coefficients d_{31} and d_{33} of the poled thin films. Even though the EO effect is observed at frequencies much lower than those of the second harmonic generation, the measured NLO coefficients could be extrapolated to a zero frequency according to a two-level model [41]. Even though it is a very simple and straightforward method, it has been shown that in some cases the two-level model may provide a decent estimates of the dispersion of second order susceptibilities [42].

The NLO coefficient measurement can therefore provide valuable information about the expected EO coefficients of the samples under investigation and thus present some arguments about the validity of the used methods. Firstly, it is valid to assume that the ratio of NLO coefficients d_{33}/d_{31} is equal to the ratio of EO coefficients r_{33}/r_{13} since there is no birefringence in the material [41]. Secondly, a rough approximation within the two-level model suggests that the EO coefficients can be estimated from the measurements of NLO coefficients if the resonance frequency and the refractive indices at corresponding wavelengths are known [41]. The ratio of $r_{13}(632\,\text{nm})/d_{31}(1064\,\text{nm})$ (henceforth r_{13}/d_{31}) was

estimated to be 0.51 by using the Eq. (13) and assuming zero birefringence [43],

$$r_{ij}(-\omega,\omega,0) = -\frac{4d_{ji}}{n^4(\omega)}\frac{f^{\omega}f^{\omega}f^{0}}{f^{2\omega''}f^{\omega''}f^{\omega''}}\frac{\left(3\omega_o^2-\omega^2\right)\left(\omega_o^2-\omega''^2\right)\left(\omega_o^2-4\omega''^2\right)}{3\omega_o^2\left(\omega_o^2-\omega^2\right)^2}, \quad (13)$$

where ω is the light frequency at which the EO coefficient is evaluated, ω' is the frequency of fundamental harmonic used for NLO coefficient measurement, ω_o the resonance frequency of material, f^{ω} and f^{0} are the local field factors.

The NLO coefficients at 1064 nm were determined using the Maker fringe technique according to procedure described in [44]. To make the results of EO and NLO coefficients comparable, the experiments were conducted after the NLO efficiency after the poling had become time-invariant.

9 Comparison of measured EO and NLO coefficients The measured EO coefficients by TM, MZI, and ATR methods are summarized in Fig. 14. In this figure, the determined EO coefficient r_{13} of thin films are plotted against the NLO coefficient d_{13} measured using the Maker fringe technique. Clearly, a linear correlation is expected, thus a linear fit is applied to the data.

In Fig. 14, we have plotted a line with a slope 0.51 that corresponds to the theoretical ratio of r_{13}/d_{13} estimated by Eq. (13) for our experimental conditions. The two-level model from NLO measurements predicts higher EO coefficients than those determined experimentally by

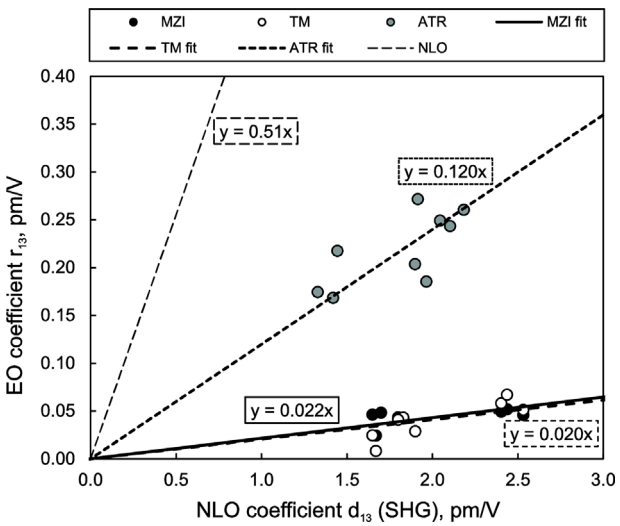

Figure 14 Measured EO coefficients r_{13} as a function of measured NLO coefficients d_{13}: MZI, TM, ATR r_{13} measured by MZI, TM, and ATR techniques, respectively; MZI fit, TM fit, ATR fit, linear fit of the r_{13} measured by MZI, TM, and ATR techniques, respectively; NLO expected r_{13}/d_{13} from two-level model [43].

MZI, TM, and ATR. There could be multiple reasons to this. Firstly, the SHG signal could be resonantly enhanced, thus leading to an inaccurate estimation of r_{13}/d_{13} by the two-level model [7]. A more sophisticated model that includes the damping effects [45, 46] may have resulted in a better approximations of the NLO and EO coefficient ratios. Secondly, the sputtering of electrodes for the EO coefficient measurements may cause a local heating and depolarization of the polymer. Thirdly, we suggest that the inaccuracy of the EO coefficient measurement could also arise from overestimation of the actual modulating electric field on the sample on account of two effects: (i) the poled polymer could have some pinholes which appear after the corona poling process and may cause the effective voltage drop on the thin film to be reduced [7, 47]; (ii) due to the contact resistance and the capacitive nature of the sample it could operate as a filter lowering the amplitude of the modulating electric field. This could also explain why the determined EO coefficients using TM and MZI methods are by an order lower than the ones determined by the ATR method in which the modulating electric field is applied only at the light coupling point. Also, in the ATR method the capacitance of the sample is low due the small area of the top electrode and thus the modulating frequency filtering could be less effective. The results obtained by MZI and TM methods are almost the same. This is not surprising, because in both methods the experimental data are approximated using the same MatLab fit to functions based on the Abelès matrix formalism which have the same input parameters: layer thicknesses and refractive indices and the applied modulating field value. Furthermore, the modulated signal was measured for the same set of samples. The obtained results confirm that both TM and MZI methods give equivalent results for the same EO response. Finally, the errors in the estimated EO coefficients could be caused by the electro-absorption effect [48]. The provided approach based on Abeles matrix formalism for estimating the EO response of the film would have allowed inclusion of electro-absorption effect. However, we estimate that this contribution might have been low due to the fact that the measurements are performed far from the absorption band.

In Fig. 15 experimental data points of r_{33} versus r_{13} which were measured by MZI, TM, and ATR techniques are evident. The slopes of the linear fits of the experimental data correspond to the ratios of r_{33}/r_{13} which are the following: 3.13 ± 0.81 (TM), 2.85 ± 1.44 (MZI), and 2.30 ± 0.23 (ATR). It would also be important to note that the ratio d_{33}/d_{31} was determined to be 1.63 ± 0.28, which differs from the ratios of identified EO coefficients. Clearly, there are contributions from other effects that have led to incorrect measurement of the tensor element ratio r_{33}/r_{13}. As outlined in [19, 22], the piezoelectric contribution, dipole rotation, or incorrect assumption of the material symmetry might be responsible for overestimation of ratio r_{33}/r_{13}. It could be that the piezoelectric contribution, that is included in the model, is not fully accounted for. This is supported by the fact that the ATR method, which is inherently insensitive to

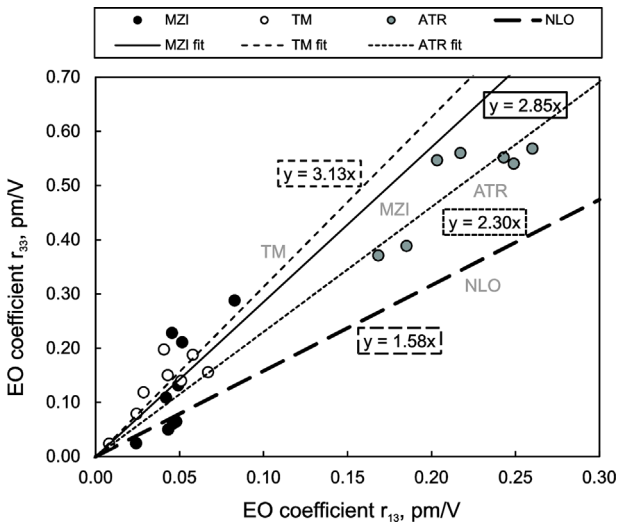

Figure 15 The EO coefficient value correlation: MZI, TM, ATR experimental data points of r_{33} versus r_{13} measured by MZI, TM, and ATR techniques, respectively, MZI, TM, ATR – linear fit of the MZI, TM, and ATR data, respectively; NLO expected r_{33}/r_{13} from the SHG measurements.

the thickness variations of the film [19], gives lower r_{33}/r_{13} ratios then the TM and MZI method.

From the errors of the respective EO coefficient ratios the ATR method should be outlined as the one that gives the most precise results. Moreover, the EO coefficient ratio obtained by the ATR technique is the closest to the ratio measured by the Maker fringe technique. Unfortunately, it is not fully clear why the ratio of r_{33}/r_{13} differ significantly from obtained ratio of NLO coefficients d_{33}/d_{31} from the second harmonic generation (SHG) measurements.

10 Comparison of EO coefficient determination methods As demonstrated in the sections above, the realization of methods for reliable EO coefficient measurements can be troublesome. The ATR measurements can be collected and processed rather fast if the method, which involves cumbersome coupling of light into the waveguide and simultaneous application of the electric field, is established. In contrast, the assembling of optical setups of TM and MZI methods are relatively simple, but the collecting and the processing of the data is very time-consuming. Moreover, to ensure that the MR and TC effects are taken into account, data processing algorithms based on the Abelès matrix formalism should be implemented. In the following section we analyze the errors of implemented methods which arise in case a multiple internal reflection and thickness modulation effects are not considered.

For the MZI method, as it was demonstrated in Fig. 4, the MR effect causes appearance of fringes in the incidence angle scan of the AC and DC signal ratio. Moreover, the MR effect has no influence on the AC and DC signal ratio at zero incidence angle on the sample. This suggests that for MZI data at zero incidence a simple analytic approximation based on Eqs. (2) and (3) can be used instead of the Abelès matrix formalism. In case the thickness changes are present in the thin film, they can be easily accounted for using the numerical approach based on the Abelès matrix formalism. As evident in Fig. 5, the EO coefficient values can be overestimated if the thickness modulation effects are not considered. This error may be significant when the optical path length change $n\Delta l$ due to the TC effect is comparable or greater than the optical path length change $l\Delta n$ due to the EO effect.

In Fig. 16, the estimated error for measured EO coefficients r_{13} and r_{33} using the MZI technique (red lines) are displayed as a function of normalized thickness changes, which are expressed as an optical path length change ratio $n\Delta l/l\Delta n$. It is evident that, if the thickness changes are not considered, the error of the estimated r_{13} value is simply the ratio $n\Delta l/l\Delta n$. Consequently, the error of the measurement is small if the EO effect dominates in the optical path length modulation.

Similar analysis is conducted for the measurement with the TM method. In Fig. 16 (green lines), we have shown our estimates of the r_{13} error if the TC effects are ignored. As it was also shown above in Fig. 11, both effects can be ignored

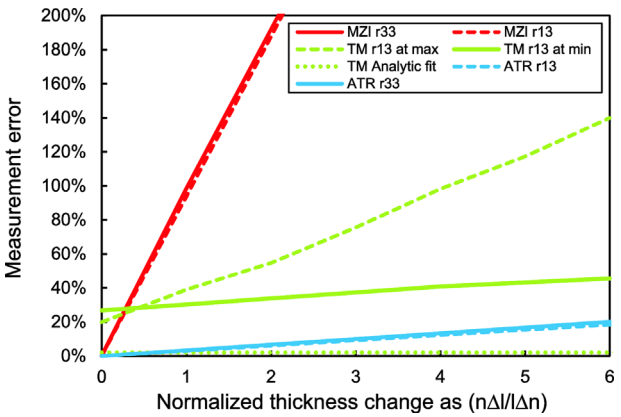

Figure 16 The error of estimated EO coefficients obtained by the MZI, TM, and ATR techniques as a function normalized thickness changes expressed as optical path length change ratio $n\Delta l/l\Delta n$. (i) The red lines indicate the error for r_{13} and r_{33} measurement by MZI technique described previously. If the thickness changes are not considered the error of the estimated r_{13} value is simply the ratio $n\Delta l/l\Delta n$. (ii) The green lines indicate the error of estimated EO coefficients obtained by the TM technique. The "TM r_{13} at max" displays the estimated error of r_{13} if the measurement is performed at incidence angle which corresponds to the local modulation signal maxima (e.g., at 37° in Fig. 11); "TM r_{13} at min" displays the estimated error of r_{13} if the measurement is performed at incidence angle which corresponds to the local modulation signal minima (e.g., at 25° in Fig. 11); "TM Analytic fit" displays the estimated error of r_{13} if the sample modulated signal angular scan is analyzed using the analytic formula (10). (iii) The blue lines indicate the error of estimated EO coefficients obtained by the ATR technique. As can be seen the thickness modulations introduce small errors in the estimated EO coefficients.

if an angular scan of the AC and DC signal ratio is performed. We estimate that the error of the simple analytic fit of the experimental data does not exceed 2% and is independent of the amplitude of the thickness modulations (see Fig. 16). The TC and the MR effects have greater influence on the retrieved EO coefficients if the measurements are done at a single incidence angle. Depending on the film thickness and refractive indices, it may turn out that the single incidence angle measurement is performed either at the minima or maxima of the fringe (see Fig. 11). In such case, even if there is no TC, the error of the retrieved values may be of the order of 20% due to the MR effects.

The retrieved EO coefficient values in the ATR method are much less sensitive to the TC effect. As shown in Fig. 16 with blue lines, even if the optical thickness modulations caused by the TC exceed the modulations caused by the EO effect five times, the error still does not exceed 15%.

11 Conclusions In this paper we have revisited measurements of thin film EO coefficients and implemented three of the most widely employed techniques: MZI, TM, and ATR. We have applied these for the measurements of corona-poled polymer thin films. Each of these techniques has shown to have multiple advantages and drawbacks. The MZI and TM optical setups are very simple. However, a correct interpretation of the experimental data obtained by the mentioned techniques requires full understanding about the effects taking place in the sample. The signal obtained by the MZI and TM techniques is strongly influenced by the multiple internal reflection and piezo- and electrostrictive TC effects, which, in our opinion, have not been sufficiently addressed in the literature. An analytic description containing both of the mentioned effects would be fairly complicated. We have shown that a numerical solution based on the Abelès matrix formalism can be used for the retrieval of the EO coefficient values from the experimental data obtained by MZI and TM methods. The approach requires recording modulated signal measurements at multiple light incidence angles on the sample, which makes the methods quite time-consuming. Moreover, the thickness change of the sample should be known with a high precision. In the MZI technique, the error that may appear if the TC effect is ignored depends on the EO response of the sample. This error may be significant for the cases when the optical path length change due to the TC effect is comparable or greater than the optical path length change due to the EO effect. The TM method is less sensitive to the thickness change effect than the MZI method. However, the errors may arise if the measurement is performed at a single light incidence angle. Surprisingly, if an angular scan of the modulated signal is performed, an analytic approximation that ignores MR and TC effects can provide an EO coefficient estimate within the precision of 2%. The EO coefficients determined by the MZI and the TM techniques are in good agreement, but the determined EO coefficients are obviously underestimated if compared with the values obtained by the ATR method. The reason for this might be that the actual modulating field for the samples used in MZI and TM setups is lower than expected due the sample imperfections, the electrode resistance and the sample impedance. In addition to the EO measurements, the NLO coefficients were determined for the same thin films. The expected ratio of r_{31}/d_{13} calculated from the SHG using the two-level model was always higher than the one observed experimentally. Such phenomenon can occur due to multiple reasons. Previous studies have attributed such disagreement to the resonant enhancement of the SHG signal [7]. We propose that the measured EO coefficients are lower than expected due to the depolarization of the sample during electrode sputtering process, as well as due to an overestimation of the applied modulating AC field during the EO measurements. We also found that the EO coefficient ratio r_{33}/r_{13} is always greater than the ratio of NLO coefficients d_{33}/d_{31}. The obtained ratios of r_{33}/r_{13} are as follows: 3.13 ± 0.81 (TM), 2.85 ± 1.44 (MZI), and 2.30 ± 0.23 (ATR); while the ratio d_{33}/d_{31} was measured to be 1.63 ± 0.28.

The ATR has shown to be the most precise and the simple technique for the determination of EO coefficients. The entire procedure, which involves measurements of modulated signals with TM and MZI setups and data processing, is quite cumbersome. Moreover, MZI and TM does not guarantee high precision EO coefficients despite the independent determination of the entire set of material constants such as refractive indices, thin film thicknesses, and the actual thickness variations due to piezo- and electrostriction effects.

Acknowledgments This work has been supported by the European Social Fund within the project "Support for Doctoral Studies at University of Latvia" and National Research Program "Multifunctional Materials and Composites, Photonics and nanotechnology (IMIS^2)."

References

[1] F. Kajzar and J. Zyss, Nonlin. Opt. Quantum Opt. **43**, 31–95 (2012).
[2] L. R. Dalton, J. Phys. **15**(20), R897–R934 (2003).
[3] R. A. Norwood, C. Derose, Y. Enami, H. Gan, C. Greenlee, R. Himmelhuber, O. Kropachev, C. Loychik, D. Mathine, Y. Merzlyak, M. Fallahi, and N. Peyghambarian, J Nonlin. Opt. Phys. Mater. **16**(2), 217–230 (2007).
[4] M. Dumont, Y. Levy, and D. Morichère, NATO ASI Série E **194**, 461–480 (1991).
[5] M. J. Shin, H. R. Cho, J. H. Kim, S. H. Han, and J. W. Wu, J. Korean Phys. Soc. **31**(1), 99–103 (1997).
[6] M. Aillerie, N. Théofanous, and M. D. Fontana, Appl. Phys. B **70**(3), 317–334 (2000).
[7] D. Morichère, P.-A. Chollet, W. Fleming, M. Jurich, B. A. Smith, and J. D. Swalen, J. Opt. Soc. Am. B **10**(10), 1894–1900 (1993).
[8] N. Benter, R. P. Bertram, E. Soergel, K. Buse, D. Apitz, L. B. Jacobsen, and P. M. Johansen, Appl. Opt. **44**(29), 6235–6239 (2005).
[9] P. Nagtegaele, E. Brasselet, and J. Zyss, J. Opt. Soc. Am. B **20**(9), 1932–1936 (2003).

[10] D. H. Park, J. Luo, A. K. -Y. Jen, and W. N. Herman, Polymers **3**(4), 1310–1324 (2011).
[11] C. Maertens, C. Detrembleur, P. Dubois, R. Jérôme, P.-A. Blanche, and P. C. Lemaire, Chem Mater. Am. Chem. Soc. **10** (4), 1010–1016 (1998).
[12] W.-K. Kuo and Y.-C. Tung, PIERS Online **5**(1), 41–45 (2009). References.
[13] T. Yamada and A. Otomo, Opt. Express **21**(24), 29240–29248 (2013).
[14] M. Sigelle, J. Appl Phys. **52**(6), 4199–4204 (1981).
[15] K. D. Singer, M. G. Kuzyk, W. R. Holland, J. E. Sohn, S. J. Lalama, R. B. Comizzoli, H. E. Katz, and M. L. Schilling, Appl Phys Lett. **53**(19), 1800–1802 (1988).
[16] E. Nitiss, M. Rutkis, and M. Svilans, Lith. J. Phys. **52**(1), 30–38 (2012).
[17] C. C. Teng and H. T. Man, Appl. Phys. Lett. **56**(18), 1734–1736 (1990).
[18] J. S. Schildkraut, Appl. Opt. **29**(19), 2839–2841 (1990).
[19] S. Herminghaus, B. A. Smith, and J. D. Swalen, J. Opt. Soc. Am. B **8**(11), 2311–2317 (1991).
[20] W. H. G. Horsthuis and G. J. M. Krijnen, Appl. Phys. Lett. **55** (7), 616–618 (1989).
[21] F. Qui, X. Cheng, K. Misawa, and T. Kobayashi, Chem. Phys. Lett. **266**(1–2), 153–160 (1997).
[22] R. A. Norwood, M. G. Kuzyk, and R. A. Keosian, J. Appl. Phys. **75**(4), 1869–1874 (1994).
[23] R. Meyrueix and O. Lemonnier, J. Phys. D **27**(2), 379–386 (1994).
[24] C. Greenlee, A. Guilmo, A. Opadeyi, R. Himmelhuber, R. A. Norwood, M. Fallahi, J. Luo, S. Huang, X.-H. Zhou, A. K.-Y. Jen, and N. Peyghambarian, Mach-Zehnder Interferometry Method for Decoupling Electro-Optic and Piezoelectric Tensor Components in Poled Polymer Films, Vol. 7774, edited by M. Eich, J.-M. Nunzi, R. Jakubiak, and T. G. Goodson III (SPIE Publications, Bellingham, WA, 2010), pp. 77740D–77740D-10.
[25] D. H. Park, C. H. Lee, and W. N. Herman, Opt. Express **14** (19), 8866–8884 (2006).
[26] E. Nitiss, M. Rutkis, and M. Svilans, Opt. Commun. **286**(1), 357–362 (2013).
[27] R. H. Page, M. C. Jurich, B. Reck, A. Sen, R. J. Twieg, J. D. Swalen, G. C. Bjorklund, and C. G. Willson, J. Opt. Soc. Am. B **7**(7), 1239–1250 (1990).
[28] O. Ahumada, C. Weder, P. Neuenschwander, U. W. Suter, and S. Herminghaus, Macromolecules **30**(11), 3256–3261 (1997).
[29] F. Abelès, Rev. Générale de l'Electricité **11**(7), 310–314 (1950).
[30] S. Larouche and L. Martinu, Appl. Opt. **47**(13), C219–C230 (2008).
[31] D. Rafizadeh and S.-T. Ho, Opt. Commun. **141**(1–2), 17–20 (1997).
[32] D.-G. Sun, Z. Liu, J. Ma, and S.-T. Ho, Opt. Laser Technol. **39**(2), 285–289 (2007).
[33] M. Rutkis, A. Vembris, V. Zauls, A. Tokmakovs, E. Fonavs, A. Jurgis, and V. Kampars, Novel Second-order Non-linear Optical Polymer Materials Containing Indandione Derivatives as a Chromophore, in: Organic Optoelectronics and Photonics II, edited by P. L. Heremans, M. Muccini, and E. A. Meulenkamp (SPIE Publications, Bellingham, WA, 2006), pp. 61922Q–61922Q-8.
[34] O. Vilitis, E. Titavs, E. Nitiss, and M. Rutkis, Latv. J. Phys. Tech. Sci. **50**(1), 66–75 (2013).
[35] T. Iwamura, S. Suka, X. Y. Liu, and S. Umegaki, Opt. Rev. **16**(1), 4–10 (2009).
[36] Y. Levy, M. Dumont, E. Chastaing, P.-A. Chollet, G. Gadret, and F. Kajzar, Mol. Cryst. Liq. Cryst. Sci. Technol. B **4**, 1–19 (1993).
[37] P. K. v. Tien, Appl. Opt. **10**(11), 2395–2413 (1971).
[38] B. H. Robinson, L. R. Dalton, A. W. Harper, A. Ren, F. Wang, C. Zhang, G. Todorova, M. Lee, R. Aniszfeld, S. Garner, A. Chen, W. H. Steier, S. Houbrecht, A. Persoons, I. Ledoux, J. Zyss, and A. K. Y. Jen, Chem. Phys. **245**(1–3), 35–50 (1999).
[39] J. A. Davies, A. Elangovan, P. A. Sullivan, B. C. Olbricht, D. H. Bale, T. R. Ewy, C. M. Isborn, B. E. Eichinger, B. H. Robinson, P. J. Reid, X. Li, and L. R. Dalton, J. Am. Chem. Soc. **130**(32), 10565–10575 (2008).
[40] Y. Yang, J. Yin, Z. Cao, Q. Shen, X. Chen, L. Qiu, and Y. Shen, Opt. Laser Technol. **39**(5), 1008–1013 (2007).
[41] J. L. Oudar and D. S. Chemla, J. Chem. Phys. **66**(6), 2664–2668 (1977).
[42] T. Goodson, S. S. Gong, and C. H. Wang, Macromolecules **27** (15), 4278–4283 (1994).
[43] K. D. Singer, M. G. Kuzyk, and J. E. Sohn, J. Opt. Soc. Am. B **4**(6), 968–976 (1987).
[44] K. Traskovskis, E. Zarins, L. Laipniece, A. Tokmakovs, V. Kokars, and M. Rutkis, Mater. Chem. Phys. **155**, 232–240 (2015).
[45] M. Kuzyk and C. Dirk, Phys. Rev. A **41**(9), 5098–5109 (1990).
[46] C. Dirk and M. Kuzyk, Phys. Rev. B **41**(3), 1636–1639 (1990).
[47] E. Nitiss, E. Titavs, K. Kundzins, A. Dementjev, V. Gulbinas, and M. Rutkis, J. Phys. Chem. B **117**(9), 2812–2819 (2013).
[48] T. Goodson and C. H. Wang, J. Appl. Phys. **80**(12), 6602–6609 (1996).